

# Advances in Antenna Array Processing for Radar 2016

Guest Editors: Hang Hu, Xue-song Wang, Michelangelo Villano, Ahmed S. Khwaja, Jeich Mar, and Wenchong Xie





---

**Advances in Antenna Array Processing for  
Radar 2016**

International Journal of Antennas and Propagation

---

## **Advances in Antenna Array Processing for Radar 2016**

Guest Editors: Hang Hu, Xue-song Wang,  
Michelangelo Villano, Ahmed S. Khwaja, Jeich Mar,  
and Wenchong Xie



Copyright © 2016 Hindawi Publishing Corporation. All rights reserved.

This is a special issue published in "International Journal of Antennas and Propagation." All articles are open access articles distributed under the Creative Commons Attribution License, which permits unrestricted use, distribution, and reproduction in any medium, provided the original work is properly cited.

## Editorial Board

Ana Alejos, Spain  
Mohammad Ali, USA  
Jaume Anguera, Spain  
Rodolfo Araneo, Italy  
Alexei Ashikhmin, USA  
Herve Aubert, France  
Paolo Baccarelli, Italy  
Xiulong Bao, Ireland  
Toni Björninen, Finland  
Stefania Bonafoni, Italy  
Djuradj S. Budimir, UK  
Paolo Burghignoli, Italy  
Shah Nawaz Burokur, France  
Giuseppe Castaldi, Italy  
Luca Catarinucci, Italy  
Felipe Catedra, Spain  
Marta Cavagnaro, Italy  
Deb Chatterjee, USA  
Shih Yuan Chen, Taiwan  
Yu Jian Cheng, China  
Renato Cicchetti, Italy  
Riccardo Colella, Italy  
Lorenzo Crocco, Italy  
Claudio Curcio, Italy  
Francesco D'Agostino, Italy  
María Elena de Cos Gómez, Spain  
Tayeb A. Denidni, Canada  
Giuseppe Di Massa, Italy  
Michele D'Urso, Italy  
Hala A. Elsadek, Egypt  
Francisco Falcone, Spain  
Miguel Ferrando Bataller, Spain  
Flaminio Ferrara, Italy  
Vincenzo Galdi, Italy  
Claudio Gennarelli, Italy  
Farid Ghanem, Algeria  
Sotirios K. Goudos, Greece  
Rocco Guerriero, Italy  
Kerim Guney, Turkey  
Song Guo, Japan  
Mohamed Himdi, France  
Tamer S. Ibrahim, USA  
Mohammad T. Islam, Malaysia  
M. R. Kamarudin, Malaysia  
Slawomir Koziel, Iceland  
Luis Landesa, Spain  
Ding-Bing Lin, Taiwan  
Angelo Liseno, Italy  
Pierfrancesco Lombardo, Italy  
Giampiero Lovat, Italy  
Lorenzo Luini, Italy  
Atsushi Mase, Japan  
Diego Masotti, Italy  
Giuseppe Mazzeola, Italy  
C. F. Mecklenbräuker, Austria  
Massimo Migliozi, Italy  
A. T. Mobashsher, Australia  
Ananda S. Mohan, Australia  
J.-M. Molina-Garcia-Pardo, Spain  
Giorgio Montisci, Italy  
Marco Mussetta, Italy  
N. Nasimuddin, Singapore  
Miguel Navarro-Cia, UK  
Mourad Nedil, Canada  
Symeon Nikolaou, Cyprus  
Giacomo Oliveri, Italy  
Pablo Otero, Spain  
Athanasios D. Panagopoulos, Greece  
Ikmo Park, Republic of Korea  
Josep Parrón, Spain  
Matteo Pastorino, Italy  
Massimiliano Pieraccini, Italy  
Xianming Qing, Singapore  
Ahmad Safaai-Jazi, USA  
Safieddin Safavi-Naeini, Canada  
Magdalena Salazar-Palma, Spain  
Stefano Selleri, Italy  
Prabhakar Singh, India  
Raffaele Solimene, Italy  
Gino Sorbello, Italy  
Seong-Youp Suh, USA  
Sheng Sun, Hong Kong  
Larbi Talbi, Canada  
Luciano Tarricone, Italy  
Parveen Wahid, USA  
Wen-Qin Wang, China  
Shiwen Yang, China  
Yuan Yao, China  
Jingjing Zhang, Denmark

# Contents

---

**Advances in Antenna Array Processing for Radar 2016**

Hang Hu, Xuesong Wang, Michelangelo Villano, Ahmed Shaharyar Khwaja, Jeich Mar, and Wenchong Xie  
Volume 2016, Article ID 5463057, 1 page

**Measurement of Rank and Other Properties of Direct and Scattered Signals**

Svante Björklund, Per Grahn, Anders Nelander, and Mats I. Pettersson  
Volume 2016, Article ID 5483547, 17 pages

**A Parasitic Array Receiver for ISAR Imaging of Ship Targets Using a Coastal Radar**

Fabrizio Santi and Debora Pastina  
Volume 2016, Article ID 8485305, 11 pages

**Robust Adaptive Beamforming Using a Low-Complexity Steering Vector Estimation and Covariance Matrix Reconstruction Algorithm**

Pei Chen, Yongjun Zhao, and Chengcheng Liu  
Volume 2016, Article ID 2438183, 9 pages

**A FPC-ROOT Algorithm for 2D-DOA Estimation in Sparse Array**

Wenhao Zeng, Hongtao Li, Xiaohua Zhu, and Chaoyu Wang  
Volume 2016, Article ID 5951717, 6 pages

**Efficient Design of the Microstrip Reflectarray Antenna by Optimizing the Reflection Phase Curve**

Xing Chen, Qiang Chen, Pan Feng, and Kama Huang  
Volume 2016, Article ID 8764967, 8 pages

## Editorial

# Advances in Antenna Array Processing for Radar 2016

**Hang Hu,<sup>1</sup> Xuesong Wang,<sup>2</sup> Michelangelo Villano,<sup>3</sup> Ahmed Shaharyar Khwaja,<sup>4</sup> Jeich Mar,<sup>5</sup> and Wenchong Xie<sup>6</sup>**

<sup>1</sup>*School of Electronics and Information Engineering, Harbin Institute of Technology, Harbin 150001, China*

<sup>2</sup>*State Key Laboratory of Complex Electromagnetic Environment Effects on Electronics and Information System, National University of Defense Technology, Changsha 410073, China*

<sup>3</sup>*Microwaves and Radar Institute, German Aerospace Center (DLR), Oberpfaffenhofen, 82234 Wessling, Germany*

<sup>4</sup>*Faculty of Engineering and Natural Sciences, Sabanci University, Tuzla, 34956 Istanbul, Turkey*

<sup>5</sup>*Department of Communications Engineering, Yuan-Ze University, Chung-Li 32003, Taiwan*

<sup>6</sup>*Key Research Laboratory, Wuhan Early Warning Academy, Wuhan 430019, China*

Correspondence should be addressed to Hang Hu; [huhang@hit.edu.cn](mailto:huhang@hit.edu.cn)

Received 25 September 2016; Accepted 26 September 2016

Copyright © 2016 Hang Hu et al. This is an open access article distributed under the Creative Commons Attribution License, which permits unrestricted use, distribution, and reproduction in any medium, provided the original work is properly cited.

RAP (Radar Array Processing) is a very active, open, and concerned topic in the field of radar. It is of great significance to promote the progress of radar theory and technology. Although the RAP has experienced five decades of research, it still represents a fascinating discipline with great development potential.

At present, the rapid development of advanced radar processing techniques is closely related to the RAP. The former includes STAP (Space-Time Adaptive Processing), MIMO (Multiple-Input Multiple-Output) radar, multichannel SAR (Synthetic Aperture Radar), adaptive detection, radar ECCM (Electronic Counter-Countermeasure), and so forth.

PAR (Phased Array Radar), MIMO radar, MIMO-PAR, and digital array radar are suitable for constituting the multichannel system due to their inherent antenna structure. Consequently, we could fully apply a variety of advanced RAP techniques to these radars.

So far, the RAP has obtained fruitful achievements in theory and algorithm respects. However, the research and development on application, system, engineering, implementation of hardware, and so on are still far from enough. And those are just what researchers and radar engineers are particularly concerned about.

The study on RAP should adopt a “systemic” point of view. In other words, it should not be regarded simply as a specific theory, algorithm, or technique issue but should

be considered under a uniform radar system framework. That is, we should incorporate RAP into adaptive detection, parameter estimation (such as adaptive monopulse), and data processing (such as adaptive tracking); consequently, the capabilities of the RAP could be assessed in the whole system.

In this 2016 special issue, we have collected papers covering the following aspects of RAP research and development: parasitic array receiver for ISAR imaging of ship targets using coastal radar, robust adaptive beamforming using low-complexity steering vector estimation and a covariance matrix reconstruction algorithm, FPC-root algorithm for 2D-DOA estimation in sparse array, and design of the microstrip reflect array antenna by optimizing the reflection phase curve.

We would like to thank all the authors for their professional contributions and all the reviewers for their time and effort. A special thank goes to Dr. U. Nickel for his constructive guidance.

*Hang Hu  
Xuesong Wang  
Michelangelo Villano  
Ahmed Shaharyar Khwaja  
Jeich Mar  
Wenchong Xie*

## Research Article

# Measurement of Rank and Other Properties of Direct and Scattered Signals

Svante Björklund,<sup>1</sup> Per Grahn,<sup>1</sup> Anders Nelander,<sup>1</sup> and Mats I. Pettersson<sup>2</sup>

<sup>1</sup>The Swedish Defence Research Agency (FOI), P.O. Box 1165, 581 11 Linköping, Sweden

<sup>2</sup>The Blekinge Institute of Technology, 371 79 Karlskrona, Sweden

Correspondence should be addressed to Svante Björklund; svabj@foi.se

Received 15 April 2016; Revised 12 July 2016; Accepted 25 July 2016

Academic Editor: Wenchong Xie

Copyright © 2016 Svante Björklund et al. This is an open access article distributed under the Creative Commons Attribution License, which permits unrestricted use, distribution, and reproduction in any medium, provided the original work is properly cited.

We have designed an experiment for low-cost indoor measurements of rank and other properties of direct and scattered signals with radar interference suppression in mind. The signal rank is important also in many other applications, for example, DOA (Direction of Arrival) estimation, estimation of the number of and location of transmitters in electronic warfare, and increasing the capacity in wireless communications. In real radar applications, such measurements can be very expensive, for example, involving airborne radars with array antennas. We have performed the measurements in an anechoic chamber with several transmitters, a receiving array antenna, and a moving reflector. Our experiment takes several aspects into account: transmitted signals with different correlation, decorrelation of the signals during the acquisition interval, covariance matrix estimation, noise eigenvalue spread, calibration, near-field compensation, scattering in a rough surface, and good control of the influencing factors. With our measurements we have observed rank, DOA spectrum, and eigenpatterns of direct and scattered signals. The agreement of our measured properties with theoretic and simulated results in the literature shows that our experiment is realistic and sound. The detailed description of our experiment could serve as help for conducting other well-controlled experiments.

## 1. Introduction

In this article we have designed an experiment for low-cost indoor measurements of rank and other properties of direct and scattered signals with radar applications in mind. In real radar applications, such measurements can be very expensive, for example, involving airborne radars with array antennas.

In this introductory section we first in Section 1.1 define the signal rank and mention some other signal properties. Then in Section 1.2 we present radar applications and other applications where the signal rank is important. Section 1.3 tells what we have done in this article and gives an outline of the rest of the article.

**1.1. Signal Rank and Other Signal Properties.** In many applications of array antennas the *covariance matrix*  $\mathbf{R} = E\{\mathbf{x}\mathbf{x}^H\}$  of the received signal vector  $\mathbf{x}$  is utilized. The vector  $\mathbf{x}$  usually contains the signals from the antenna channels and possibly

some temporal dimension. The vector can be called a *space* (or *space-only*) *snapshot* or *space-time snapshot*, respectively.

The rank of the covariance matrix for the case with  $\mathbf{x}$  containing only external signals and without the white receiver noise is important in radar applications and in many other applications (see Section 1.2). It states how many, in some sense, independent signals impinge on the antenna. We talk about the *signal rank*, which is the rank of this covariance matrix.

As  $\mathbf{R}$  usually is unknown, it must be estimated in the algorithms that use it. A common estimate is [1, 2]

$$\hat{\mathbf{R}} = \frac{1}{N_R} \sum_{n=1}^{N_R} \mathbf{x}_n \mathbf{x}_n^H, \quad (1)$$

where  $\mathbf{x}_n$  are training snapshots and  $N_R$  is the number of such snapshots. These training snapshots must be selected wisely, depending on the application, and their acquisition will take

some time, the *acquisition interval*. The acquisition of the training data and the estimation of the covariance matrix influence the rank.

Other signal properties than the rank which we consider in this article are the DOA (Direction of Arrival) spectrum and eigenpatterns. The DOA spectrum shows the distribution of received power from different DOAs. Eigenpatterns are formed by using the eigenvectors of  $\hat{\mathbf{R}}$  as beamforming weights when plotting the antenna array factor. See Section 3.5 for more details.

*1.2. Applications.* In *interference* suppression in radar, the rank of direct and scattered signals is important. Such interference can be *direct path jamming* (signals from a jammer travelling one-way line-of-sight to the radar), *clutter* (signals from the radar transmitter travelling to a surface, where they are undesirably scattered back to the radar, also called *cold clutter*), and *hot clutter* (signals travelling one-way from a jammer to the radar, not directly but scattered on a surface). The received radar signal in a pulse-Doppler radar can be stored in a *radar data cube* with dimensions for antenna channels (*space*), pulses (*slow-time*), and range bins (*fast-time*). Suppression of interference is commonly performed with linear filters, which can be one-dimensional, two-dimensional, or three-dimensional. For suppression of direct path jamming, space-only snapshots are usually employed, for cold clutter usually space-slow-time and for hot clutter usually space-fast-time.

The output of the suppression filter is  $y = \mathbf{w}_a^H \mathbf{x}$ , where  $\mathbf{x}$  is a received snapshot. The filter weights are usually computed as [3–5]

$$\mathbf{w}_a = \mu \mathbf{R}_{\mathbf{q}\mathbf{q}}^{-1} \mathbf{w}_0, \quad (2)$$

where  $\mu$  is a scalar and  $\mathbf{R}_{\mathbf{q}\mathbf{q}}$  is the covariance matrix of the interference plus (receiver) noise signal vector  $\mathbf{x}_{\mathbf{q}}$ . The vector  $\mathbf{w}_0$  contains the weights without adaptation. It is usually the steering vector towards the target, possibly with tapering to reduce the sidelobes [5]. The use of filter (2) is commonly called *adaptive beamforming* for space-only snapshots or STAP (*Space-Time Adaptive Processing*) for space-time snapshots (this is also called *optimal* beamforming and *optimal* STAP if  $\mathbf{R}_{\mathbf{q}\mathbf{q}}$  is known and *adaptive* beamforming and *adaptive* STAP if  $\mathbf{R}_{\mathbf{q}\mathbf{q}}$  is estimated). The interference rank determines the needed DoFs (degrees of freedom = number of filter coefficients minus one) of the filter and the needed number of training snapshots (see, e.g., [4]). The DoF should be at least as many as the rank. There are many proposed methods, called *reduced rank methods*, for the suppression, with the DoFs adapted to the rank; for example, see [4, 6, 7].

Clutter in bistatic radar (the transmitter and receiver geographically separated) is similar to the case of hot clutter in normal (monostatic) radar. It has been suggested that also bistatic clutter should be suppressed by STAP [8]. Many high resolution DOA, Doppler, and range estimation methods in radar also need to know the signal rank.

In applications other than radar, the signal rank is also needed. In Electronic Support Measures (ESM), a kind of electronic warfare, the objective is to learn as much as possible about noncooperative radar and radio transmitters.

Among other things, it is desired to estimate the number and location of the transmitters. This information can be used as information only or as a help for jamming. Some methods for estimating the number of emitters and their location need the signal rank. In wireless communication it is suggested to use adaptive beamforming and DOA estimation methods for interuser interference suppression and signal separation [1]. For estimating multipath channel models in wireless communication, DOA estimation can be used [9]. For adaptive beamforming and DOA estimation the signal rank is often needed. In MIMO (Multiple Input Multiple Output) communications, the signal rank is directly related to the transmission capacity.

*1.3. Description of Work and Outline of Article.* This article describes how we have designed and executed low-cost indoor measurements of direct and scattered signals. Direct signals travel one-way in line-of-sight from transmitter antenna to receiver antenna. Scattered signals do not travel in line-of-sight but are scattered on a surface on the way. We have performed the measurements in an anechoic chamber with an experimental array antenna where the received signals arrived directly from the transmitter(s) (direct signals) or were scattered on a moving rough surface reflector (scattered signals). Our experiment takes several aspects into account: transmitted signals with different correlation, decorrelation of the signals during the acquisition interval, covariance matrix estimation, noise eigenvalue spread, calibration, near-field compensation, and scattering on a rough surface. An advantage of indoor measurements in an anechoic chamber compared to outdoor measurements is the good control of the influencing factors, which is necessary to draw objective conclusions.

The main result of this paper is the design of the experiment for characterization of signal properties of direct and scattered signals. Also our measured signal properties could be seen as results. They agree with theoretic and simulated results in the literature. We have not seen such measured results but they should exist.

In [10], how the space-only rank of direct path signals was dependent on several factors for our experimental array antenna was studied. Also, noise properties were studied. Part of the material in this paper has earlier been published in [11] but the current article contains more details and a significantly deeper analysis.

In Section 2 we will discuss the relation between rank and eigenvalues and also motivate why we can measure space-time rank with space-only snapshots. Then in Section 3 the experimental setup is described and Section 4 gives some measurement results. A discussion is carried out in Section 5 and, finally, conclusions are presented in Section 6.

## 2. Some Preliminaries

What now follows is a discussion of some topics that are needed for and which motivate the article.

*2.1. Rank and Eigenvalues.* The rank of a covariance matrix is equal to the number of eigenvalues larger than zero.

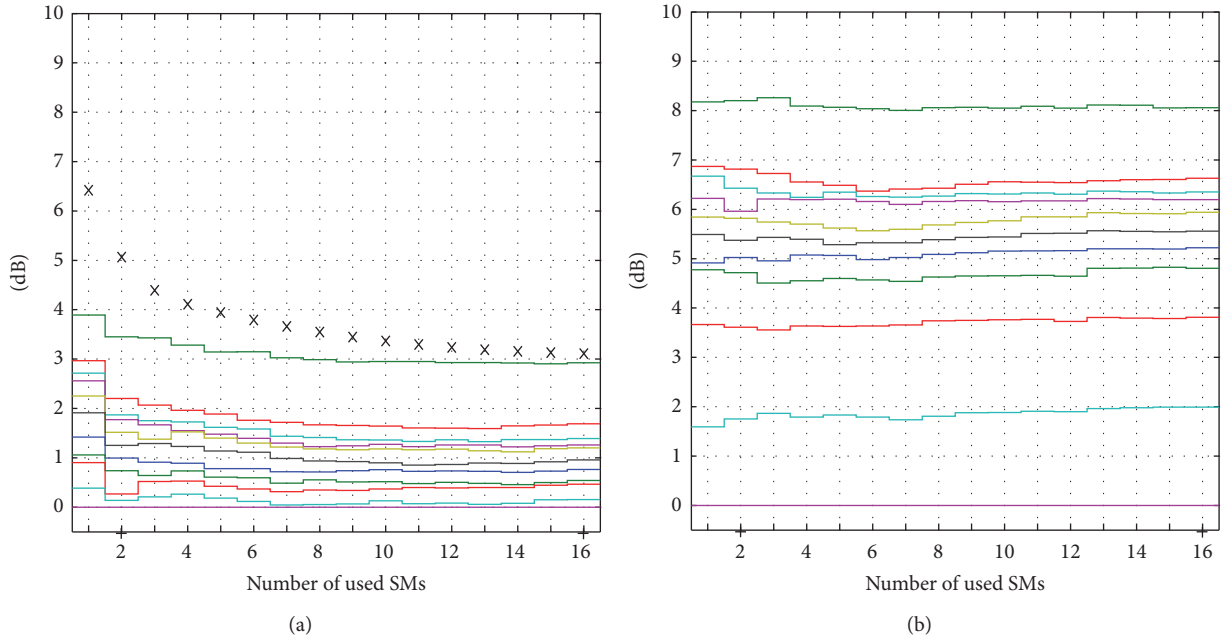


FIGURE 1: Noise eigenspectrum in measurement CIW (one transmitter and reflector; see Table 1). (b) With spatial calibration using a decoupling matrix and (a) without calibration. dB scale. See Section 3.3 for “SM.” See Section 3.5 for an explanation of the figure.

However, what matters for interference suppression [4] and number of sources and DOA estimation [1] is the number of eigenvalues larger than the white noise power. This number is called the *effective rank* [4]. Theoretically, for a known covariance matrix and for white noise as the only signal, all eigenvalues will be equal and also equal to the noise power. This level is called *the noise floor*. Thus, the effective rank is the number of eigenvalues larger than the noise floor. These eigenvalues are caused by external signals, like targets, clutter, jammers, or radio transmitters and are called *signal or interference eigenvalues*. The smaller eigenvalues are caused by the receiver noise and are called *noise eigenvalues*.

In reality the noise eigenvalues will not be equal. There are two reasons. First, the estimated eigenvalues will be different, even if the true covariance matrix has equal eigenvalues, because of estimation errors [4, 10]. If these incorrectly estimated noise eigenvalues are used in the optimal filter (2), the performance will be degraded [4]. Two possible solutions are to set the noise eigenvalues to their correct value (by calibration or appropriate estimation [12]) or to use diagonal loading [4]. When setting the correct noise eigenvalue, the number of signals/interference eigenvalues must be known.

The second reason for different noise eigenvalues is that the true eigenvalues really are different due to system nonidealities, like unequal noise power in the channels or correlation between the channels, or due to the used calibration, for example, with a decoupling matrix (Figure 1 and Section 3.2). These true unequal noise eigenvalues should not be made equal since the optimal filter (2) needs the true covariance matrix, including true unequal noise eigenvalues.

To determine the number of signals/interference eigenvalues (of direct and scattered signals) we compute in this

article a threshold  $\lambda_T$  as the maximum eigenvalue of a measured and estimated noise-only covariance matrix, normalized with the minimum eigenvalue. The threshold then includes the effects due to finite number of snapshots and to nonidealities of the system like unequal and correlated channel noise. The eigenvalues below the threshold are caused by the system (noise and nonidealities) and weak signal/interference eigenvalues. The eigenvalues above the threshold will then, hopefully, only be caused by the external signal/interference sources. Eigenvalues above the threshold will be called *large eigenvalues*.

**2.2. Hot Clutter and Space-Only Data.** Hot clutter suppression is an important use of our results. Therefore we here explain why our space-only measurements of direct and scattered signals are relevant for hot clutter.

The theoretic results in [14] about the estimated space-fast-time hot clutter covariance matrix indicate that the rank of this matrix can be measured by the space-only covariance matrix, if the number of scatterers seen by the receiver is less than the size of the space-only snapshot (which is the case in our measurements since in all experiments the number of large eigenvalues, max 10, is less than the size of the snapshot, 12; see Table 2). Fast-time effects, like jammer and system bandwidth and time-delay to the scatterers, are included in the theoretic model and affect the space-only rank through varying decorrelation of the signals from different scatterers. What determine the rank of space-only or space-fast-time signals are the scatterers and not the number of used samples in space or fast-time. Note that the results in [14] are valid for the estimated covariance matrix (1). This is the covariance matrix that must be used in the signal processing. This is also

the one which is used in the analysis of our measurements. With an estimated covariance matrix the acquisition interval, during which decorrelation can occur, is inevitable.

In [15] the authors measure channel rank in indoor wireless communications by the rank of the time-only covariance matrix of the received signal. They say that in narrowband systems the channel rank is equal to the number of resolvable multipaths for uncorrelated scattering, which with our terminology is the number of uncorrelated sources. This confirms that what determine the rank are the scatterers and not the number of used samples in space or time.

### 3. Experimental Setup

**3.1. The Experimental Array Antenna.** The experimental receiver antenna [10, 16] used in this article was designed and built by FOI (the Swedish Defence Research Agency). The high quality antenna has sidelobe levels below  $-60$  dB [10, 16] and DOA estimation resolution below one-tenth of the conventional beamwidth [10, 17]. The antenna consists of a horizontal receiving linear array of 12 antenna elements with slightly less than half a wavelength separation (45 mm), 12 receiver modules, 12 A/D converters (12 bits), and 12 buffer memories. The antenna has an agile frequency band of 2.8–3.3 GHz and an instantaneous bandwidth of 5 MHz. The antenna elements are vertically polarized and have a horizontal 3 dB beamwidth of about  $115^\circ$  and a vertical beamwidth of about  $15^\circ$  [10]. The horizontal beamwidth of the whole array is about  $10^\circ$ . The receiver modules were manufactured by Ericsson Microwave Systems (today Saab Electronic Defence Systems). From the buffer memories the signals are transferred to a standard computer, where the IQ-conversion, DDC (digital downconversion and downsampling with a factor of 4), calibration correction, and spatial signal processing are performed in nonreal time. See the hardware block diagrams in [16].

The noise properties of our experimental antenna have been investigated by Pettersson in [10]. He stated that the noise sources, without external transmitters, are mainly internal thermal noise from the receiver modules and external thermal noise from the anechoic chamber walls. With external transmitters, there may be additional noise sources, like sampling jitter and phase noise of the signal generators. The true noise power is different in the channels [10] and it may differ by up to 1.5 dB. The noise also has a small correlation between the channels. The absolute value of the nondiagonal elements of the noise covariance matrix can be up to about one-tenth of the diagonal elements [10]. These two noise properties will give spread of the estimated noise eigenvalues; see Section 2.1.

**3.2. Calibration.** Accurate channel equalization (for frequency response) and spatial channel calibration (for mutual coupling) are utilized [10, 16]. The spatial calibration can be performed with three different methods [10]

- (i) with a DOA correction table on the steering vectors,
- (ii) with a decoupling matrix on the steering vectors,
- (iii) with a decoupling matrix on the antenna signals  $\mathbf{x}$ .

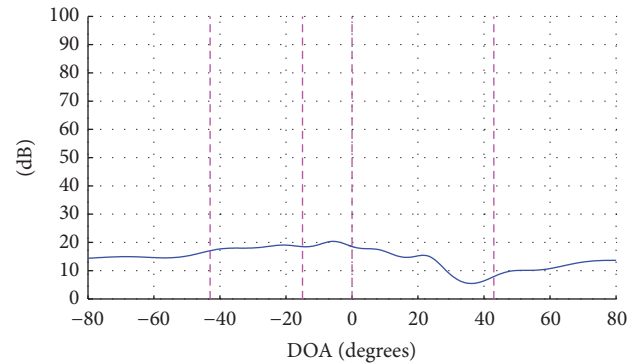


FIGURE 2: Capon DOA spectrum without spatial calibration. Otherwise the same measurement (U2SS, two uncorrelated strong transmitters; see Table 1) and processing as in Figure 10. See Section 3.5 for an explanation of the figure.

The fourth potential method, using a DOA correction table on the antenna signals, is not possible because these signals do not correspond to a single and known DOA. We prefer using a correction table on the steering vectors (method (i)) whenever possible. We have not found any drawbacks with storing such a table instead of only a decoupling matrix, which is contrary to the opinion in [18].

If in STAP the spatial calibration is performed on the antenna signals  $\mathbf{x}$  (by method (iii)), then the same calibration should be done on the antenna signals  $\mathbf{x}_n$  utilized for the estimation of the interference covariance matrix (1). The reason is to keep the STAP filter (2) optimal, for example, keeping the filter as a matched filter. However, if the spatial calibration is applied on the signals, the internal noise will become more correlated, due to the decoupling matrix [10], and the spread of the noise eigenvalues will be increased (Figure 1 and Section 2.1).

Without any spatial calibration the interference suppression performance will be degraded significantly. See Figure 2 for an example with a Capon DOA spectrum (Section 3.5) and compare with Figure 10 where spatial calibration is applied (via a DOA correction table on the steering vectors). See also [18]. The Capon spectrum is a form of the STAP filter (2).

**3.3. Reflector and Data Acquisition.** The measurements were performed in an anechoic chamber at FOI. Both the array antenna and the reflector were horizontally oriented (Figure 3). The reflector, made of a fine-meshed aluminum net of size  $4.0 \text{ m} \times 1.5 \text{ m}$ , was irregularly dented. It was designed to simulate a rough surface with a Gaussian height distribution (with a standard deviation somewhat less than one wavelength) and a Gaussian height correlation function (with a correlation distance of some wavelengths). This surface was chosen to obtain a sufficient number of scattering points from hills and valleys and sufficient roughness to have more than a wavelength bistatic range variation due to the surface roughness. We did not aim to model different terrain types but to achieve multipaths and obtain decorrelation by movement.

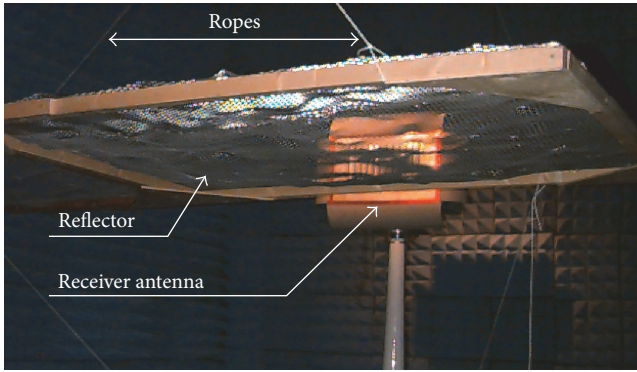


FIGURE 3: The reflector and the receiver antenna in the anechoic chamber. Photo from [13].

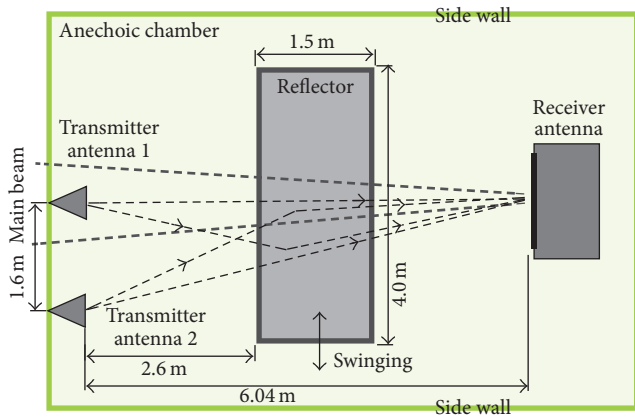


FIGURE 4: Top view of transmitter and receiver antennas and the reflector in the anechoic chamber. The drawing is not to scale.

The reflector was suspended from the ceiling using thin ropes at a height which gave grazing angles of about  $9^\circ$ . This grazing angle was just outside of the 3 dB elevation beamwidth ( $7.5^\circ$ ) of the experimental antenna. This geometry was chosen to have an unobstructed view of the antenna for the direct path signal and to have a sufficient delay corresponding to about one wavelength to obtain a large phase shift for the scattered signals. See Figures 4 and 5 for placement of the equipment in the chamber. The suspension allowed the reflector to swing easily from one side to the other.

When the reflector was swinging back and forth, with a deviation of one to two wavelengths, several submeasurements (SMs) were conducted with a delay of 15 s between the SMs. Each SM contained 256 snapshots (after downconversion and downsampling) and took  $40 \mu\text{s}$  to measure. These snapshots were utilized to estimate a covariance matrix (1). The used covariance matrix in the analysis (Section 3.5) is the average of the covariance matrices from the used SMs. The total time for all SMs was about 3 min for 12 SMs (3072 snapshots), 4 min for 16 SMs (4096 snapshots), and 6 min for 24 SMs (6144 snapshots). Increasing the number of used SMs in this study corresponds to increasing the acquisition interval in [14, 19] (denoted as  $T$  in [19]). An acquisition interval is needed to estimate the covariance matrix (1).

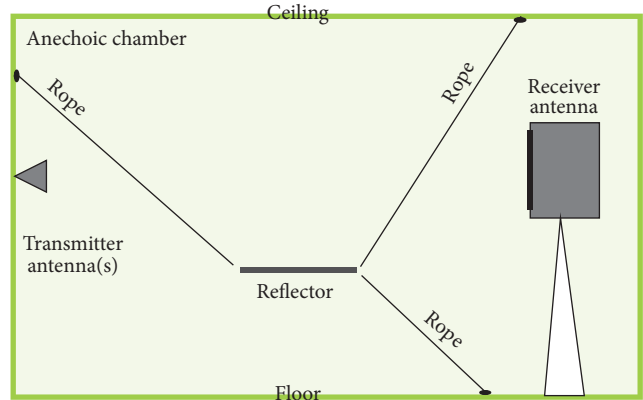


FIGURE 5: Side view of transmitter and receiver antennas and the reflector in the anechoic chamber. The drawing is not to scale.

By utilizing several SMs and a swinging reflector we could simulate decorrelation of the direct and scattered signals. The movement of the reflector gave a random component in the phase of the signal. By this the different multipath signals decorrelated with each other and with the direct signal. The movement of the reflector also enabled us to measure an “average” reflector instead of a particular one by using the same reflector at different positions.

The use of the reflector was not meant to replicate the exact generation of cold or hot clutter or any other signal/interference. In applications the decorrelation can occur due to movement of transmitter and receiver, nonzero bandwidth, and so forth (see above and Section 5).

**3.4. Transmitters.** We used one or two transmitter antennas, which were positioned at about the same height as the receiver antenna. The transmitter antenna 1 was located at the broadside of the receiver antenna and antenna 2 was shifted in DOA (Direction of Arrival) by  $15^\circ$ , which is 1.5 beamwidths of the receiver antenna; see Figure 4. Transmitter antenna 1 was a rectangular standard gain horn with a horizontal 3 dB beamwidth of  $30^\circ$ . The second transmitter antenna was a conical ridge horn. The receiver antenna was directed towards transmitter antenna 1, which had DOA  $0^\circ$  seen from the receiver antenna array center.

The distance between the transmitter antenna 1 and the receiver antennas was 6.0 m, which is on the limit to be considered a far-field distance for one antenna element. Near-field corrections in the receiver antenna were therefore applied [10, 16]. The far-field (Fraunhofer) region for the receiving antenna is beyond 5 m [20], and the radiating near-field (Fresnel) region is between 0.7 and 5 m. This means that the reflector is in the Fresnel region with almost three times the distance from the reactive near-field. We can therefore assume that there is no coupling between the antenna and the reflector and that the reflector will not influence the receiving antenna properties. By this we conclude that the antenna setup will not influence the decorrelation properties investigated in the article.

One or two commercially available signal generators were used for the transmitters. The transmitted waveforms were

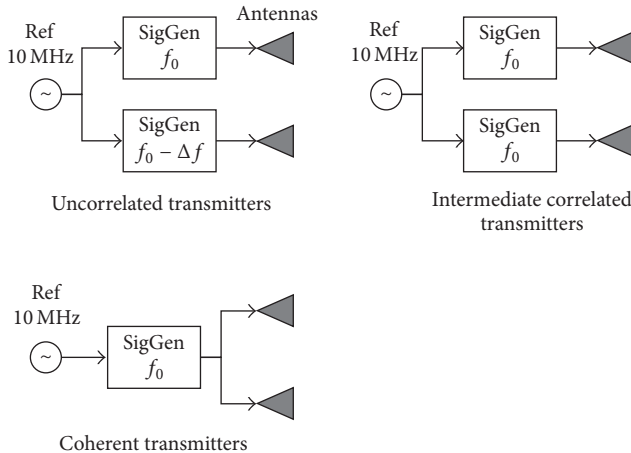


FIGURE 6: Generation of uncorrelated, intermediate correlated, and coherent transmitters. An integral number of periods of the uncorrelated signals fit exactly in the acquisition interval. The frequency  $f_0$  was about 3 GHz and  $\Delta f$  about 0.4 MHz.

pure sinusoids, that is, the carrier signal without modulation. Measurements were conducted with coherent, intermediate correlated, and uncorrelated transmitted signals (Figure 6). The coherent signals originated from the same signal generator which fed both antennas. The uncorrelated signals were generated by two signal generators with different frequencies. The frequencies were selected so that integer numbers of periods of the sinusoid signal of each transmitter (after downconversion and downsampling) were received during the data acquisition interval. The two transmitted signals then seemed uncorrelated over this interval. This matter is treated in [10]. We believe that the accuracy of the frequencies of the transmitters and the internal oscillators of the receivers was sufficiently good to give sufficiently low correlation between the signals which should be “uncorrelated.” Completely uncorrelated signals are not necessary. Even if the signals are somewhat correlated, the same qualitative behavior is achieved regarding the eigenanalysis [21]. A similar condition for space uncorrelation was noted in [19]. The intermediate correlated signals were generated by two signal generators with the same frequency. The two signal generators were in all cases phase-locked with a 10 MHz signal. The intermediate correlated signals should therefore be close to coherent. The used frequencies for the transmitters were 2999.596875 MHz and 2999.193750 MHz. These frequencies fulfill the requirements described above.

Table 1 lists important measurement parameters of our measurements. The two transmitters were selected to be either nearly equal in strength or very different in strength. This later case could imitate a situation with a weak target signal and a strong jammer. The difference in power, 45 dB, was chosen so that the power of the weak transmitter would be similar to the power of the reflections from the stronger transmitter.

**3.5. Methods of Reflection Analysis.** Our first analysis type employed to describe the direct and scattered signals is the

TABLE 1: Parameters of the measurements.

Name	Number of transmitters	Correlation	PG <sup>a</sup> Tx 1 <sup>b</sup> [dB]	PG <sup>a</sup> Tx 2 <sup>b</sup> [dB]	SNR <sup>c</sup> [dB]
CIS	1	—	0.5	—	41
C2SS	2	Coherent	0.5	-4.2	45
U2SS	2	Uncorrelated	0.5	-4.5	40, 32
I2SS	2	Intermediate	High	High	42
CIW	1	—	-39.5	—	14
C2SW	2	Coherent	0.5	-44.2	43
U2SW	2	Uncorrelated	0.5	-44.5	44, -3

<sup>a</sup>PG is the *effective isotropic radiated power* [dBm].

<sup>b</sup>The DOA was 0° for transmitter 1 (Tx 1) and -15° for transmitter 2 (Tx 2).

<sup>c</sup>The SNR is for one antenna channel (mean value between the channels) and one time sample after IQ, DDC, and calibration and is estimated from data (by the frequency spectrum, not the Capon spectrum). For measurements C2SS, I2SS, and C2SW the stated SNR is for the sum of the two transmitters. The reason for this is that the transmitters could not be separated in the SNR estimation.

TABLE 2: Summary of eigenspectra results<sup>a</sup>.

Name	Figure	1 SM	Increase per SM <sup>b</sup>	12 SMs	24 SMs
CIS	Figure 8	1	1	8	8
C2SS	Figure 9	1	≤1	7	8
U2SS	Figure 10	2	2 (up to 6 SM), ≤1 (above 6 SM)	10	10
I2SS	Figure 11	2	≤1	9	10
CIW	Figure 12	1	0	1	1
C2SW	Figure 13	1	≤1	8	8
U2SW	Figure 14	2	1	8	8

<sup>a</sup>The table gives the number of large eigenvalues, that is, eigenvalues larger than the threshold  $\lambda_T$ . Often the last large eigenvalue came later than the rest.

<sup>b</sup>Approximate values.

*Capon DOA spectrum* [22] (also called MVDR, Minimum Variance Distortionless Ratio),

$$P_{\text{capon}}(\theta) = \frac{1}{\mathbf{a}^H(\theta) \hat{\mathbf{R}}^{-1} \mathbf{a}(\theta)}, \quad (3)$$

where  $\mathbf{a}(\theta)$  is the spatial steering vector and  $\hat{\mathbf{R}}$  is the estimated covariance matrix in (1). The steering vector is a model of how the receiver perceives an impinging signal from direction  $\theta$ . For us  $\mathbf{a}(\theta)$  was measured in the anechoic chamber and tabulated for  $-80^\circ \leq \theta \leq 80^\circ$  with a step of  $0.5^\circ$ . For angles  $\theta$  between the ones in the table the vector  $\mathbf{a}(\theta)$  was interpolated linearly. The calibration correction for antenna element coupling, amplitude and phase drift, and near-field were all done on the steering vectors. This is method (i) in Section 3.2 (DOA correction table on the steering vectors). See [10, 16] for more information.

The Capon spectrum shows the distribution of received power from different DOAs unless the signals are coherent. The Capon spectrum also gives an indication of how well optimal beamforming and STAP can suppress scattered signals, since it is computed according to (2), with special

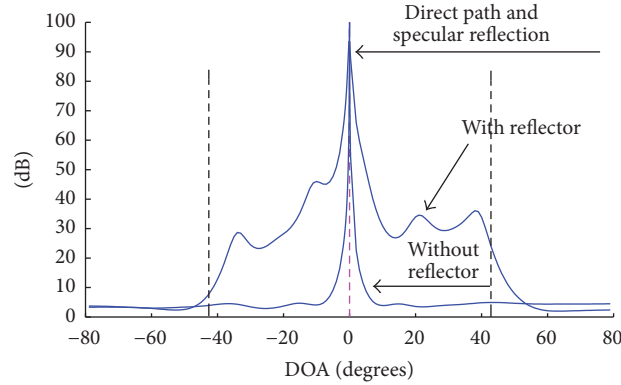


FIGURE 7: Capon DOA spectra with the reflector (measurement C1S in Table 1, same result as Figure 8) and without the reflector plotted on top of each other. The region between the left and right vertical dashed lines is the reflection region, that is, where reflections are possible because of the presence of the reflector. The middle dashed line(s) is the true DOA of the direct signal(s). 24 SMs.

choices of the covariance matrix and the scalar  $\mu$ . For the Capon spectra, 24 SMs were used. As an example of the influence of the reflector, Figure 7 shows the Capon spectra for experiments with and without the reflector.

The second analysis type is the *eigenspectrum*, which is the eigenvalues of the antenna signal covariance matrix, usually sorted in decreasing order. We have plotted the eigenvalues in an uncommon manner. They are not plotted in decreasing order for a single covariance matrix but all eigenvalues for the same covariance matrix are plotted in the same “column.” The different columns are used for covariance matrices with different number of SMs. We have computed the eigenvalues for an increasing number of used SMs, up to a maximum of 24. However, in the graphs in this article only up to 16 SMs are plotted, due to space limitations. See Figure 8(b) for an example. The eigenspectrum illustrates the signal/interference rank. In each presentation we have normalized the eigenvalues to the smallest one. No spatial calibration was performed for the eigenspectra results (except as an illustration in Figure 1). For interference suppression this is not necessary, since when computing the optimal weights in (2), the calibration can and should be performed on the quiescent weight vector  $\mathbf{w}_0$  (method (i) in Section 3.2) instead of the covariance matrix (via a decoupling matrix on the received signals used to estimate the covariance matrix, method (iii)). Done differently, the noise eigenvalue spread would increase (Figure 1) and the noise eigenvectors would influence the optimal filter (2) more and perhaps require more DoFs. In this paper we determine the interference rank by the threshold described in Section 2.1. In the graphs the threshold is marked by the symbol “ $\times$ ”; see Figure 8.

We also present *eigenpatterns* (eigenvector antenna array factors) [23]. Eigenpatterns are formed by using the eigenvectors of the antenna signal covariance matrix as beamforming weights when plotting the antenna array factor. Since the element pattern is not included in the steering vector, our eigenpatterns will not be antenna patterns. For the eigenpatterns the spatial calibration was performed using a decoupling matrix on the training signals (method (iii) in Section 3.2). See [10, 16] for more information. Since the

reflector is not placed in the extreme near-field and the eigenpatterns are transformed to the far-field (by near-field compensation on the training signals and by the used far-field steering vector), there should be no significant differences in the eigenpatterns compared to the case where the reflector is in the far-field.

## 4. Measurement Results

**4.1. Capon DOA Spectra and Eigenspectra.** The Capon DOA spectrum and the eigenspectrum for measurement C1S (a single, strong transmitter; see Table 1) are shown in Figure 8. A clear peak at DOA  $0^\circ$  is seen in Figure 8(a). This is the direction of the transmitter. The peak contains both the direct signal and the specular reflection. In the figure the extension of the reflector is given by dashed vertical lines. As seen in the figure, most reflections from the reflector are about 60 dB lower than the peak. We see that the whole reflector is covered by the power from the transmitting antennas. In Figure 8(b), the number of large eigenvalues, that is, above the threshold (Section 2.1), starts with one and increases by one for each new SM, except for the last large eigenvalue, up to a maximum of eight. This means that we can consider the signal/interference rank to be about one to eight, depending on the level of decorrelation, of which the direct signal is one. Table 2 summarizes all eigenspectra.

Figure 9 presents results from measurement C2SS (two strong coherent transmitters). Here, the Capon spectrum peak for DOA  $0^\circ$  is considerably lower, 30 dB, than in Figure 8. The second direct signal peak is also weak and has some bias in DOA. Most parts of the reflection region are weaker than in Figure 8. The probable reason for the low levels is the mutual cancellation of the signals from the two transmitters due to the coherence between them [21, 24]. The eigenspectrum is similar to Figure 8. This similarity means that two coherent transmitters are seen as a single transmitter. The largest eigenvalue in Figure 9 has nearly the same size as in Figure 8, despite the largest peak being lower in Figure 9 than in Figure 8. This is possible since the eigenvalues do not correspond directly to the power of the signal sources but the

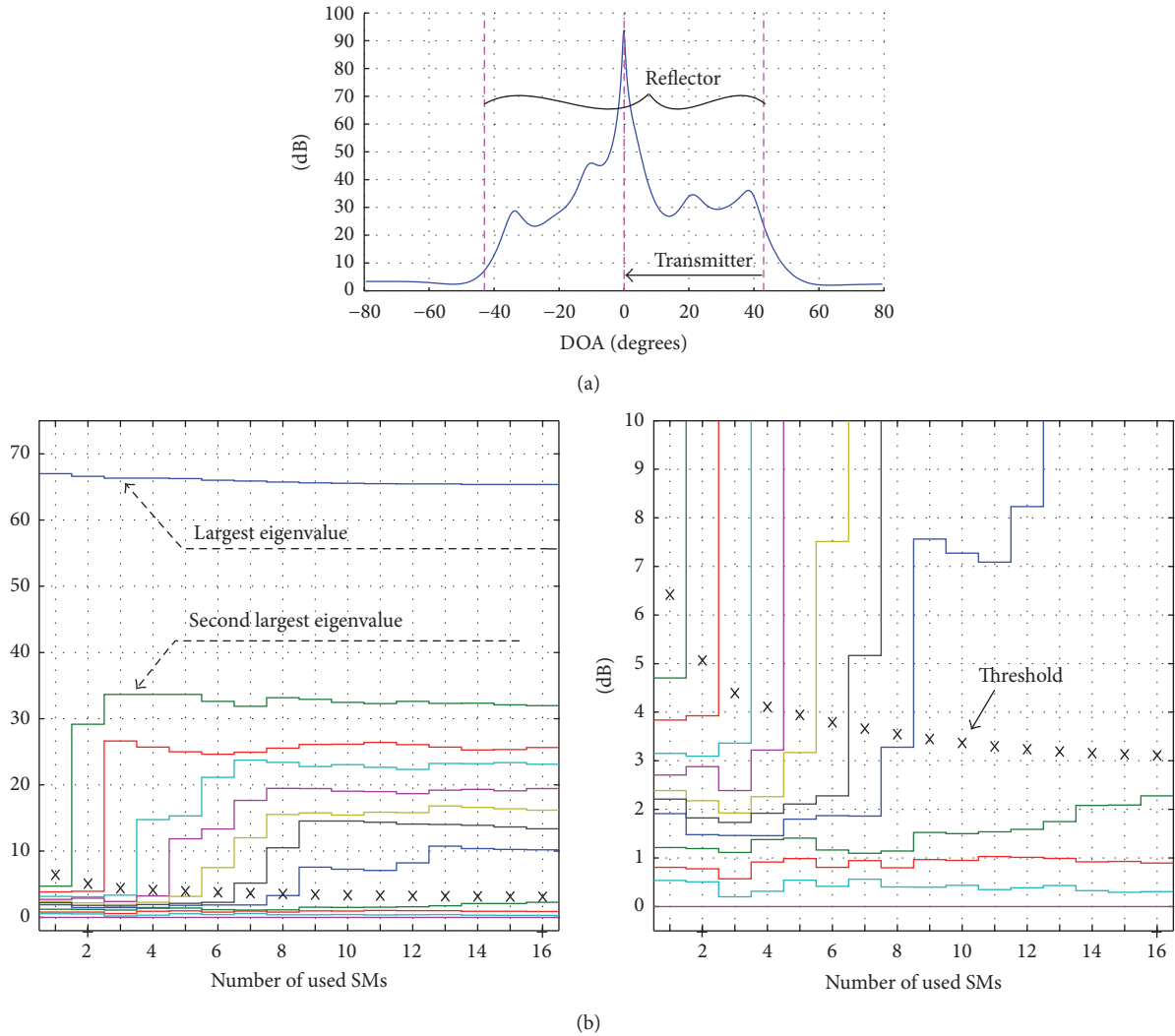


FIGURE 8: Measurement CIS. A single strong transmitter. (a) Capon DOA spectrum. Figure description in Figure 7. (b) Eigenspectrum. Zoom-in to the right. dB scale. See Section 3.3 for “SM.”

sum of the signal eigenvalues  $\lambda_l$  is equal to the sum of the signal powers  $P_l$  [21]:

$$\sum_{l=1}^L P_l = \sum_{l=1}^L \lambda_l, \quad (4)$$

where  $L$  is the number of signal sources.

The case with two strong uncorrelated transmitters (measurement U2SS) is depicted in Figure 10. Both direct signals (including specular reflections) are clearly seen. Also the reflection region is clearly visible. When studying the eigenspectrum, we note a difference to the previous measurements. Here it starts with two large eigenvalues for the first SMs and initially increases by two for each new SM (up to six). Then it increases slower, probably because some eigenvalues are below the noise floor, up to ten large eigenvalues on the remaining SMs.

Figure 11 shows Capon spectrum and eigenspectrum for the case with two strong and intermediate correlated transmitters (measurement I2SS). The Capon spectrum seems to be nearly identical with the case of uncorrelated transmitters (compare Figures 10 and 11). The eigenspectrum starts with two large eigenvalues and then increases by only one for each extra SM, except for no change between 3 and 4 SMs. The maximum number of large eigenvalues is ten as for uncorrelated transmitters (U2SS) but the final large eigenvalues require more SMs and therefore more decorrelation than for uncorrelated transmitters. The more uncorrelated the transmitters are, the more equal in size the eigenvalues are in the simulations in [19, 21]. In measurement I2SS the transmitters were more correlated than in U2SS. The eigenvalues were probably therefore more unequal and some were too small to cross the threshold and become “large” ones. Thus, the signal/interference rank increases as the correlation between the transmitters decreases.

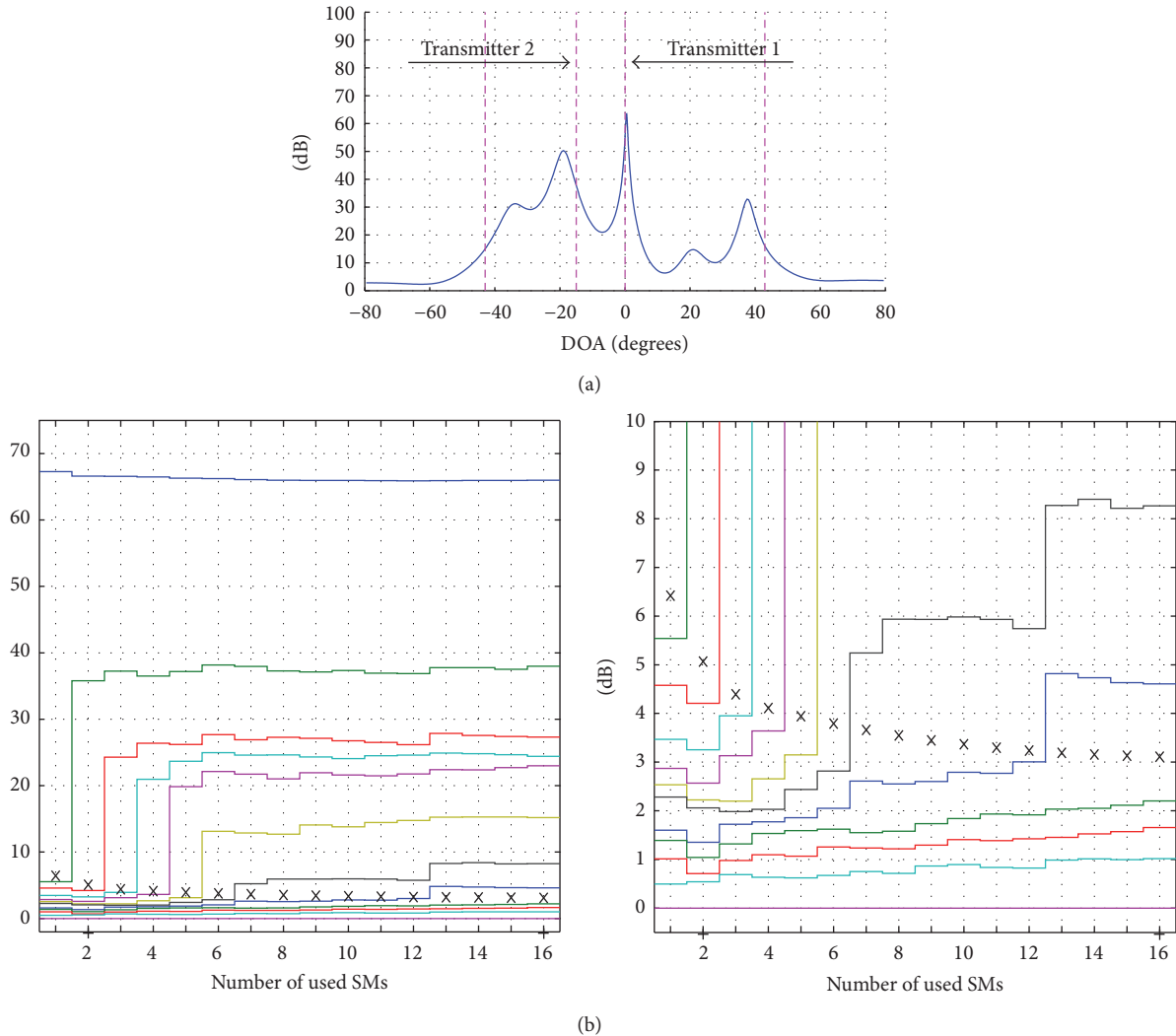


FIGURE 9: Measurement C2SS. Two coherent strong transmitters. (a) Capon DOA spectrum. (b) Eigenspectrum. Zoom-in to the right. dB scale. See Section 3.3 for “SM.”

In Figure 11, we observed that there are two large eigenvalues for a single SM. By changing the analysis to use only 1 SM in 16 repetitions, we obtained two large eigenvalues in 13 repetitions, we obtained one large eigenvalue in 1 repetition, and we obtained three large eigenvalues in 2 repetitions. This shows that with a high probability there will be two large eigenvalues for 1 SM.

We now turn to the case with a single weak transmitter (measurement CIW). The Capon spectrum (Figure 12) tells us that the peak is 40 dB lower than in Figure 8, which is as expected since the transmitted power was this much lower. The reflection region is not seen at all. The explanation is that the scattered signals are weaker than the noise. The eigenspectrum in Figure 12 contains the same information. It has only one large eigenvalue for all SMs, because of the weak transmitter. All but one eigenvalue are below the noise. See also the discussion about the iceberg effect in Section 5.

The Capon DOA spectrum in Figure 13 for two coherent and different strong transmitters (measurement C2SW)

resembles the one for a single strong transmitter (Figure 8) very much. Also the eigenspectra (Figure 13(b)) are fairly similar for few SMs (compare Figures 8(b) and 13(b)). For up to 6 SMs, the number of large eigenvalues increases by one for each SM as in Figure 8 but the 7th large eigenvalue does not show up until SM 11 for C2SW. The probable reason for the similarity is that the weak transmitter is too weak to disturb the strong transmitter.

In measurement U2SW (two uncorrelated transmitters with different strength) the Capon DOA spectrum (Figure 14) is also rather similar to the one with a single strong transmitter (Figure 8). The direct signal is about 3 dB lower and the valleys of the reflection region are deeper. Interestingly, the eigenspectrum (Figure 14) starts with two large eigenvalues, which indicates two noncoherent transmitters despite the low power of the weak transmitter, below the noise ( $\text{SNR} \approx -3$  dB). This is also possible because of (4). Then the number of large eigenvalues increases by one for each additional SM, which could indicate a single transmitter. It ends with eight

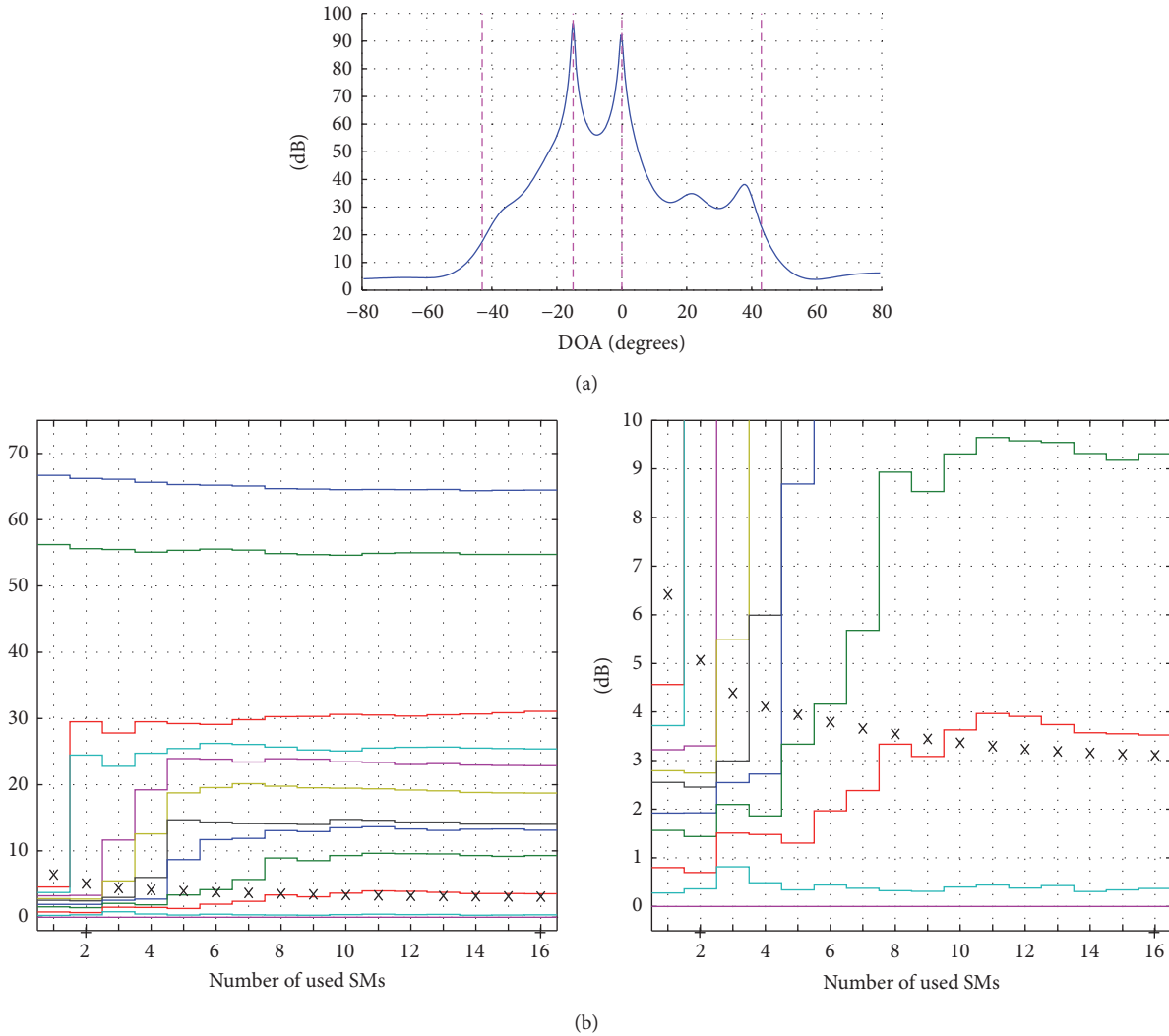


FIGURE 10: Measurement U2SS. Two uncorrelated strong transmitters. (a) Capon DOA spectrum. (b) Eigenspectrum. Zoom-in to the right. dB scale. See Section 3.3 for “SM.”

large eigenvalues as for a single strong transmitter. There are probably several signal/interference eigenvalues below the noise.

4.2. *Eigenpatterns.* Figures 15 and 16 give some examples of eigenpatterns. More eigenpatterns can be found in [13] according to Table 3. We notice that each eigenpattern has one or more large lobes. When the peak of the highest lobe is within the reflection region (where the reflector can give scattered signals, denoted with the outermost dashed vertical lines), we say that the eigenpattern *covers* the reflection region. When the peak is outside this region we say that the eigenpattern covers the region outside.

In our measurements the eigenpatterns corresponding to the largest eigenvalues usually cover the reflection region. The remaining eigenpatterns cover the region outside. The one or two largest eigenvalues have eigenpatterns which are directed towards the strong direct signals and the other eigenpatterns usually have nulls in these directions (Figures 15 and 16).

Actually, the eigenpatterns, associated with the eigenvectors, must be as “different” as possible since they are orthogonal.

There is approximately the same number of covering eigenpatterns for 1 SM (“without order”) as for 12 SMs; see Table 3.

Strangely enough, there is about the same number of eigenpatterns covering the reflection region for 1 SM as there are large eigenvalues using all (24) SMs, especially “without order” (compare Tables 2 and 3). Exceptions are the measurement CIW which has 7 covering eigenpatterns (Figure 16) despite only 1 large eigenvalue and U2SS and I2SS, which have somewhat fewer covering eigenpatterns than eigenvalues. CIW seems to observe all distinct sources with its eigenpattern but not with its eigenvalues. Remember some signal eigenvalues are below the noise floor in the eigenspectra.

For the weak direct signal in the presence of a strong direct signal, its eigenpattern has a bias in DOA. Also for the case with two equal strong coherent transmitters there

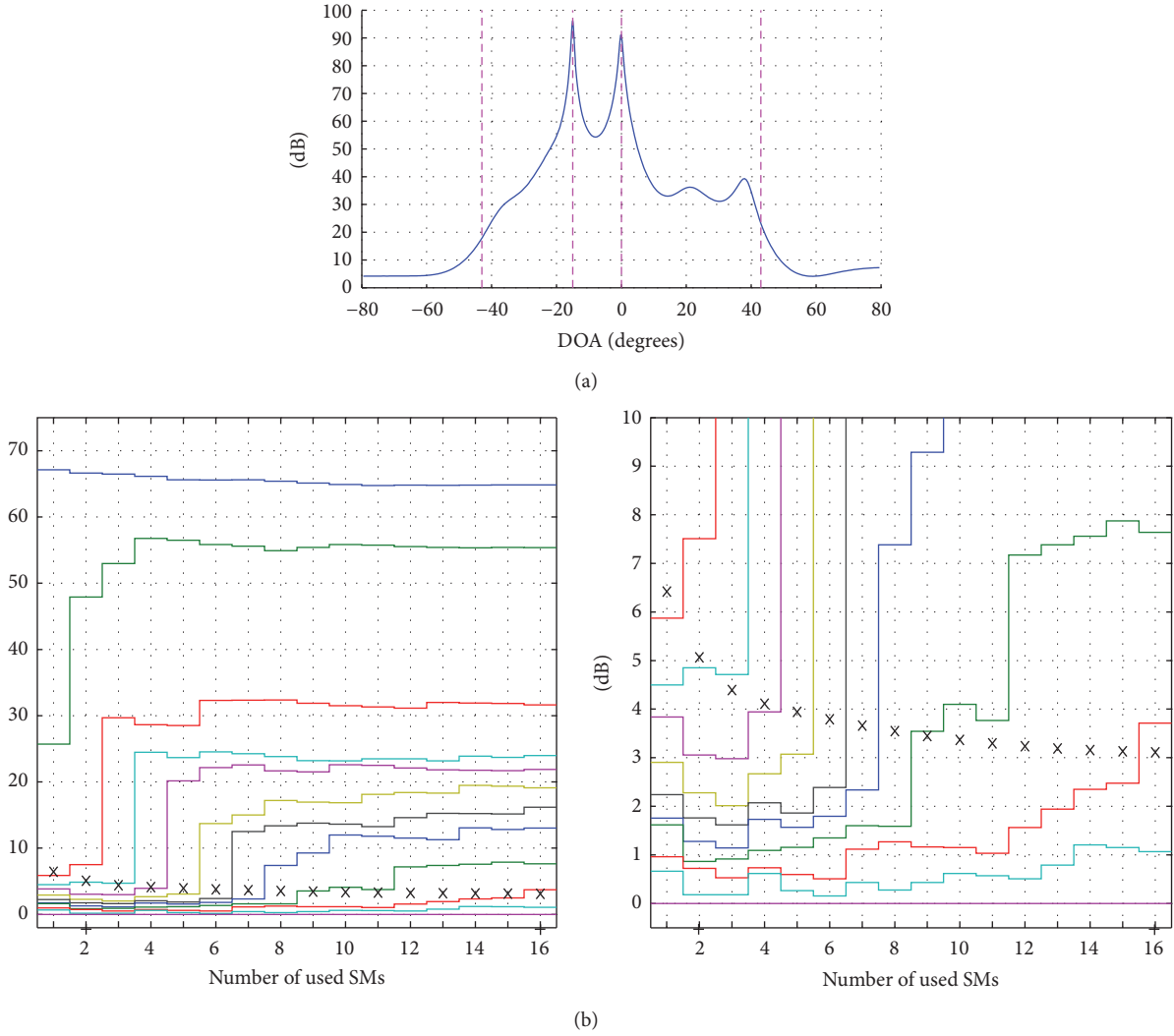


FIGURE 11: Measurement I2SS. Two intermediate correlated strong transmitters. (a) Capon DOA spectrum. (b) Eigenspectrum. Zoom-in to the right. dB scale. See Section 3.3 for “SM.”

TABLE 3: Summary of eigenpattern results<sup>a</sup>.

Name	1 SM w ord <sup>b</sup>	1 SM w/o ord <sup>c</sup>	Figure	12 SMs	Figure
C1S	8	8	6.8 in [13]	8	6.9 in [13]
C2SS	8	8	Figure 15	7-8	6.33 in [13]
U2SS	5	7	6.24 in [13]	8	6.25 in [13]
I2SS	2	6	6.36 in [13]	8	6.37 in [13]
C1W	7	7	Figure 16	7-8	6.21 in [13]
C2SW	5	7	6.16 in [13]	8	6.17 in [13]
U2SW	8	8	6.28 in [13]	8	6.29 in [13]

<sup>a</sup>The table gives the number of eigenpatterns covering the reflection region.  
<sup>b</sup>“w ord” stands for “with order” and means the number of covering eigenpatterns in an uninterrupted sequence from the first one.  
<sup>c</sup>“w/o ord” means “without order” and means the total number of covering eigenpatterns.

is a bias, although less than for two signals with unequal strength.

4.3. *Summary of the Measurement Results.* We have from the measurements obtained results on the rank and other properties of direct and scattered signals. We see that the signal/interference rank depends on the number of transmitters, the SNR (Signal to Noise Ratio), the correlation between the transmitters, and the degree of decorrelation of the transmitter signals that occurs during the data acquisition.

Without decorrelation, the direct and scattered signals of a transmitter will all be coherent. If the scattered signals decorrelate with each other and with the direct signal, the rank is increased. Two coherent transmitters appear as a single transmitter regarding the signal/interference rank. Two strong uncorrelated transmitters give rise to the double number of sources compared to a single transmitter.

With higher SNR, more eigenvalues of the eigenspectrum tail will appear above the noise level, and the rank will be higher.

The eigenpatterns show the reflection region and the DOAs to the direct signals. The eigenpattern can tell us the number of signal sources when the signals still are coherent.

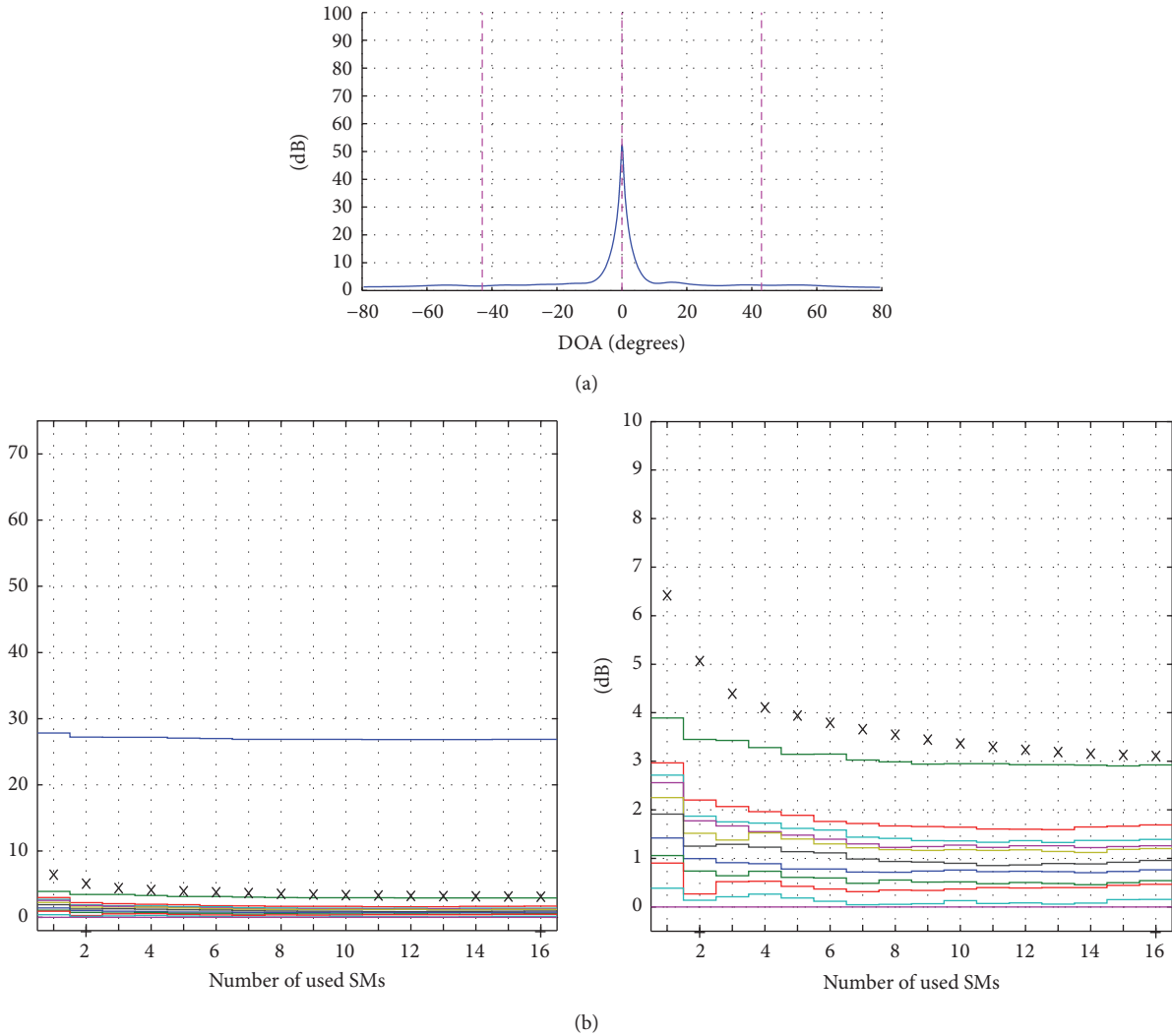


FIGURE 12: Measurement CIW. A single weak transmitter. (a) Capon DOA spectrum. (b) Eigenspectrum. Zoom-in to the right. dB scale. See Section 3.3 for “SM.”

Alternatively, they can tell us the extent of the reflection region if the number of signal sources is known.

## 5. Discussion

*5.1. Discussion about the Experimental System.* To show the eigenvalues for an increasing number of used SMs when the reflector is moving gives the possibility to study the signal/interference rank for different degrees of decorrelation. In a real case, decorrelation can occur as a result of platform motion (comparing with [19]), internal clutter motion, nonzero bandwidth [25], long acquisition interval for estimating the covariance matrix, carrier frequency changes, and so forth.

Note that we are studying the estimated covariance matrix (1), not the true covariance matrix. It is the estimated matrix which must be used in algorithms. The measured signal snapshots were space-only snapshots. However, the time

dimension enters via the acquisition interval, during which decorrelation of the signals can occur (see also Sections 2.2 and 3.3). This will increase the rank. The decorrelation increases if the acquisition interval is prolonged (more SMs) as in [14].

The Capon spectrum gives a good picture of the impinging power from the direct and scattered signals if the transmitters are noncoherent.

The measurement result will be influenced by different transmitter signals. With a different frequency of the pure sinusoid, there will be different differences in amplitude and phase between the scatterers on the reflector. If the frequency is changed much, the number of scatterers will change and thereby the signal rank will change too, with a higher number and higher rank with a higher frequency. Now the signal bandwidth is low and the scatterers on the reflector cannot be resolved in range (= fast-time). A bandwidth in the order of 100 MHz would be needed to resolve in range. If the

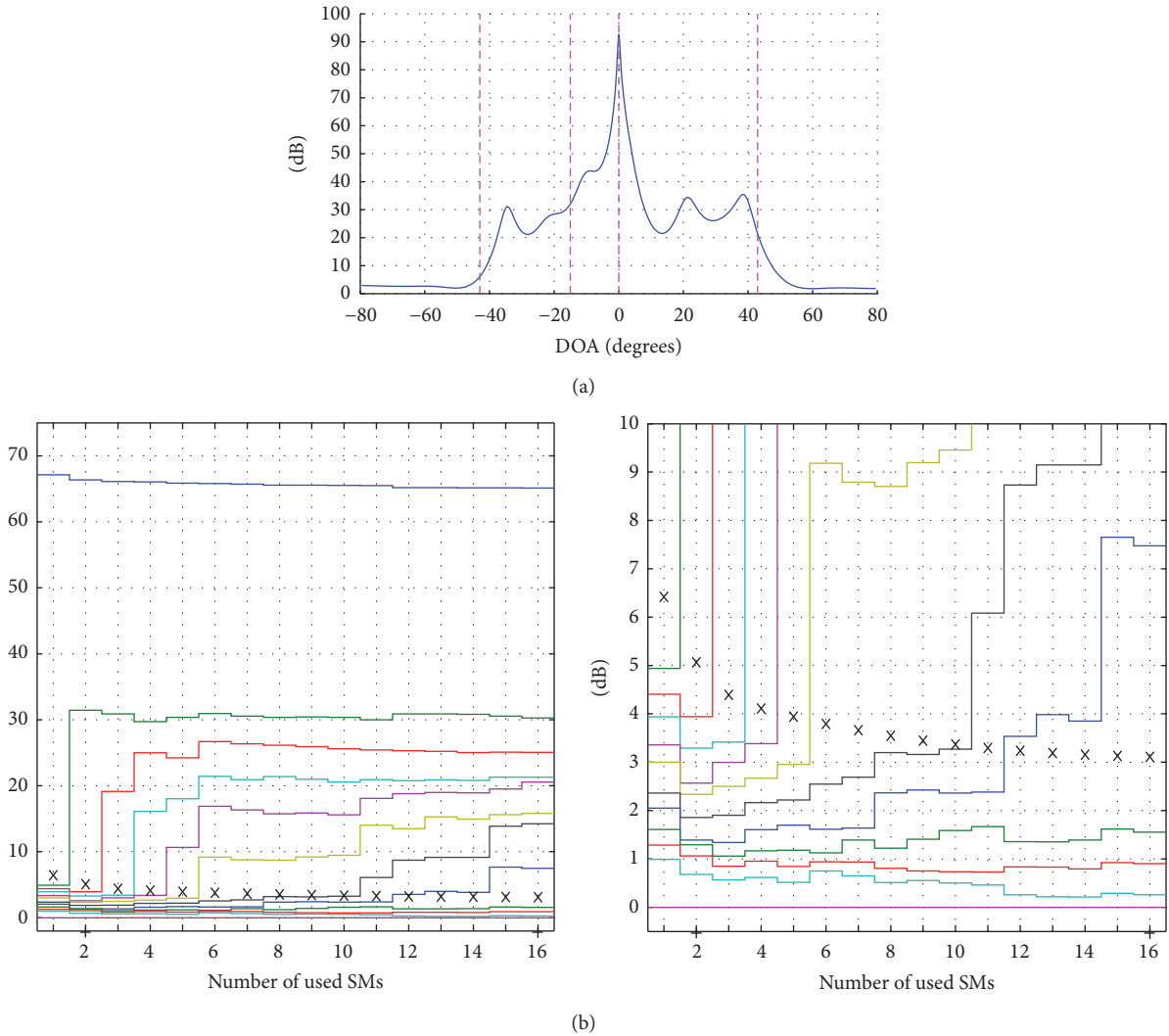


FIGURE 13: Measurement C2SW. Two coherent transmitters, one strong and one weak. (a) Capon DOA spectrum. (b) Eigenspectrum. Zoom-in to the right. dB scale. See Section 3.3 for “SM.”

transmitter signals are different from pure sinusoids, the emulation of uncorrelated transmitted signals probably had to be performed in a different way.

The measurement quality was considered before, during, and after conducting the experiments, for example, with a written experimental design [26] and estimation of uncertainty in the position measurements of the antennas and the reflector. See [13] for further information on this.

*5.2. More Comparison of the Measurements with the Literature.* The literature [19, 21, 27] says that each noncoherent monochromatic source with a different DOA gives rise to a large eigenvalue, which is in accordance with our measurements C1S, C2SS, and U2SS.

The more uncorrelated the sources are the more equal in size the eigenvalues are in the experiments in [19, 21]. In particular, uncorrelated sources with well separated DOAs give each an eigenvalue of similar size according to [21]. These statements are in accordance with our measurements I2SS

and U2SS. In [25] a theoretic expression for the size of the two eigenvalues of two uncorrelated zero bandwidth signals is derived. In our measurements U2SS and U2SW the difference between the two largest eigenvalues for 1 SM was about 6 dB larger than the prediction of the theory. The discrepancy could be due to a nonideal measurement system and to a nonzero bandwidth because of time limited measurements.

The result that the eigenspectrum starts with a single eigenvalue for (one or two) coherent transmitters for a single SM (a very short acquisition interval) in our measurements agrees with the result in [14] showing that the rank will be one for the case without motion and with zero jammer bandwidth and for the case with motion of radar and/or jammer, zero bandwidth, and a “vanishing short” acquisition interval. One of our results is that the number of large eigenvalues will increase up to a limit when the number of SMs is increased. This result is in agreement with the result in [14] showing that each scatterer will appear as an independent source when the acquisition interval goes to infinity.

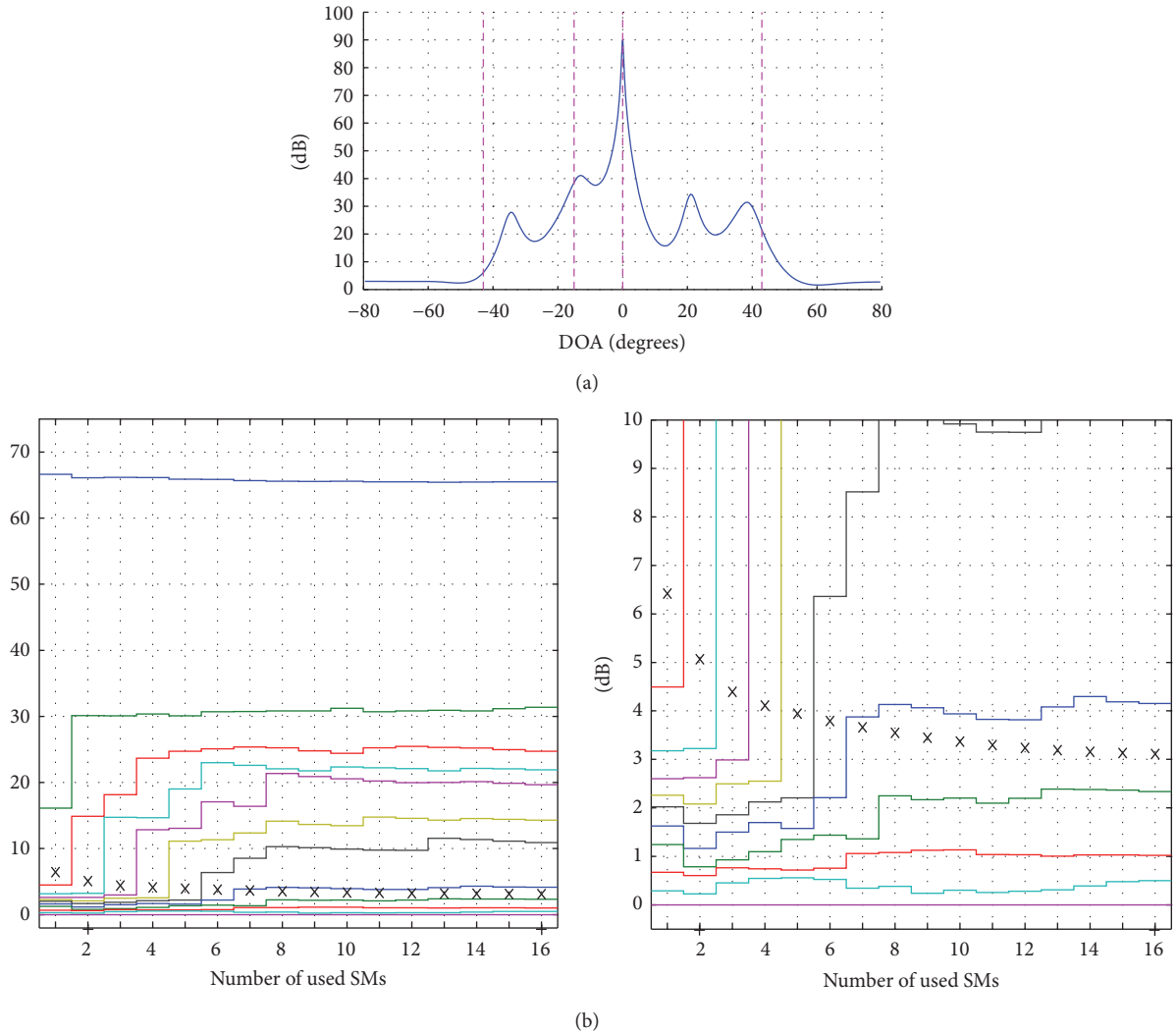


FIGURE 14: Measurement U2SW. Two uncorrelated transmitters, one strong and one weak. (a) Capon DOA spectrum. (b) Eigenspectrum. Zoom-in to the right. dB scale. See Section 3.3 for “SM.”

We noticed by our measurements that the number of large eigenvalues depends on the signal power in comparison to the noise floor (compare measurement CIS in Figure 8 with CIW in Figure 12 and measurement U2SS with U2SW). The higher the signal power is, the more the eigenvalues of the spectrum tail will appear above the noise level. It is like an iceberg lifting above the ocean surface. This phenomenon is therefore called the *iceberg effect*. It is described in [4, 27] and there illustrated by simulations.

We found that the number of eigenpatterns which cover the reflection region (by the number of eigenpatterns which have their highest peak within the reflection region) is nearly independent of the number of used SMs. To estimate the number of signals using the eigenvalues we need many SMs but with the eigenpatterns it is enough with a few. Thus, it seems like the fact that the eigenpatterns are better for the estimation of the number of signals than the eigenvalues. Nevertheless, it is well-known that the number of large eigenvalues determines the required DoFs for interference suppression [4]. In [27] it is noticed, probably from simulations,

that the eigenpatterns corresponding to the signal sources were “essentially unaffected” by a “modest amount” of interference subspace leakage, which is in agreement with our results.

We conclude that our measurement results agree in most cases with theoretic and simulated results presented in the literature.

## 6. Conclusions

We have designed an experiment for low-cost indoor measurements of direct and scattered signals with radar applications in mind. We have good control of the influencing factors, which is necessary to draw objective conclusions. The detailed description of our experiment could serve as a help for conducting other well-controlled experiments. Our experimental design has some characteristics:

- (i) Emulation of coherent, intermediate correlated, and uncorrelated signal sources (Section 3.4).

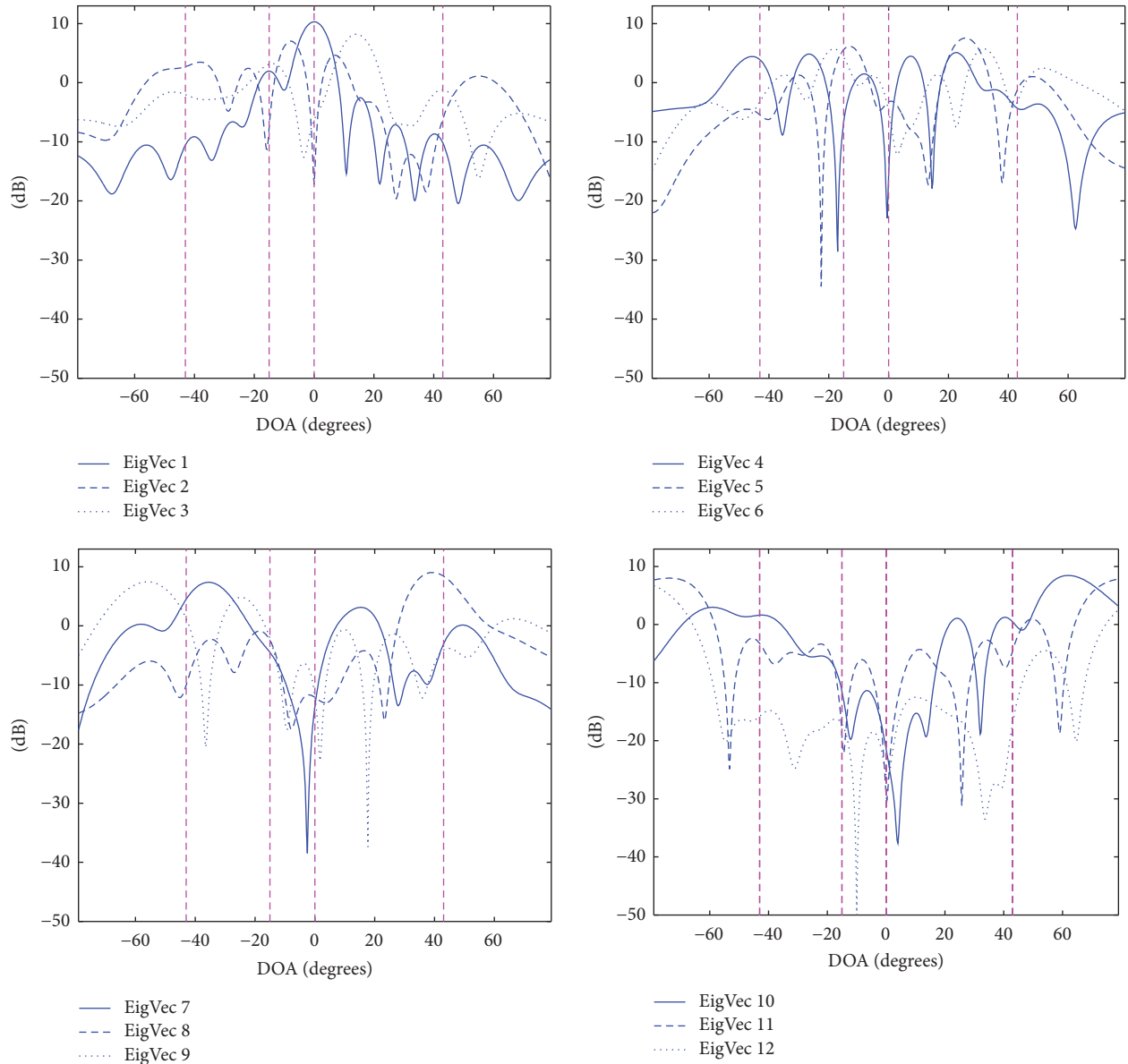


FIGURE 15: Eigenpatterns for measurement C2SS (two coherent strong transmitters). 1 SM. Dashed vertical lines are the true DOAs of the transmitter(s) and the nearest left and right corner of the reflector. Figure 6.32 in [13].

- (ii) Calibration: when to calibrate and when not and also how to calibrate in different cases (Sections 3.2 and 3.5).
- (iii) Near-field compensation: relation to receiving antenna properties, decorrelation, and eigenpatterns (Sections 3.4 and 3.5).
- (iv) Noise eigenvalue spread: relation to calibration, hardware quality, and signal rank (Sections 2.1, 3.2, and 3.5).
- (v) Emulation of a rough surface by a reflector (Section 3.3).
- (vi) Decorrelation of the signals by movement of the reflector (Section 3.3).
- (vii) Acquisition interval for the estimation of the covariance matrix and its effects on the rank (Section 3.3).
- (viii) Analysis methods: Capon DOA spectrum, eigenspectrum, and eigenpatterns (Section 3.5).

Section 4.3 summarizes our measured properties of direct and scattered signals. The agreement of our measured properties with theoretic and simulated results presented in the literature shows that our experimental design is realistic and sound.

### Competing Interests

The authors declare that they have no competing interests.

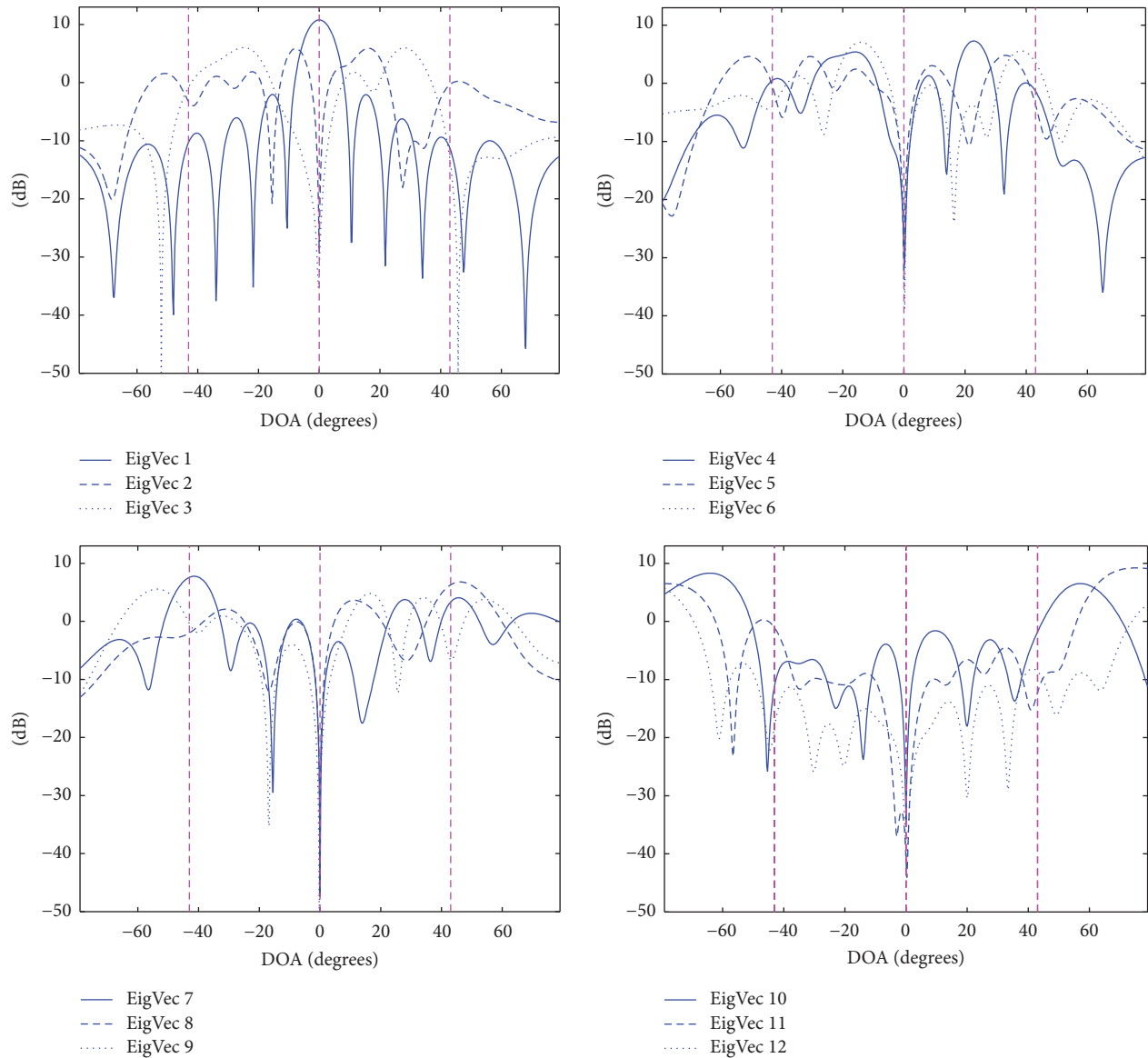


FIGURE 16: Eigenpatterns for measurement CIW (a single weak transmitter). 1 SM. Dashed vertical lines are the true DOAs of the transmitter(s) and the nearest left and right corner of the reflector. Figure 6.20 in [13].

## Acknowledgments

This work has been financially supported by the Swedish Armed Forces, the Swedish Defence Materiel Administration, and the Swedish Knowledge Foundation.

## References

- [1] H. Krim and M. Viberg, "Two decades of array signal processing research: the parametric approach," *IEEE Signal Processing Magazine*, vol. 13, no. 4, pp. 67–94, 1996.
- [2] I. S. Reed, J. D. Mallett, and L. E. Brennan, "Rapid convergence rate in adaptive arrays," *IEEE Transactions on Aerospace and Electronic Systems*, vol. 10, no. 6, pp. 853–863, 1974.
- [3] L. E. Brennan and I. S. Reed, "Theory of adaptive radar," *IEEE Transactions on Aerospace and Electronic Systems*, vol. 9, no. 2, pp. 237–252, 1973.
- [4] J. R. Guerci, *Space-Time Adaptive Processing for Radar*, Artech House, 2003.
- [5] J. Ward, "Space-time adaptive processing for airborne radar," Tech. Rep. 1015, MIT Lincoln Laboratory, 1994.
- [6] M. C. Wicks, M. Rangaswamy, and R. Adve, "Space-time adaptive processing: a knowledge-based perspective for airborne radar," *IEEE Signal Processing Magazine*, vol. 23, no. 1, pp. 51–65, 2006.
- [7] J. R. Guerci, J. S. Goldstein, and I. S. Reed, "Optimal and adaptive reduced-rank STAP," *IEEE Transactions on Aerospace and Electronic Systems*, vol. 36, no. 2, pp. 647–663, 2000.
- [8] W. L. Melvin and M. E. Davis, "Adaptive cancellation method for geometry-induced nonstationary bistatic clutter environments," *IEEE Transactions on Aerospace and Electronic Systems*, vol. 43, no. 2, pp. 651–672, 2007.

- [9] M. Viberg, "Direction-of-arrival estimation," in *Smart Antennas: State of the Art*, chapter 16, Hindawi Publishing Corporation, New York, NY, USA, 2005.
- [10] L. Pettersson, "An S-band digital beamforming antenna: design, procedures and performance," FOA Report FOA-R—99-01162-408—SE, 1999.
- [11] S. Björklund, P. Grahm, and A. Nelander, "Analysis of array antenna measurements with a rough surface reflector," in *Proceedings of the 34th Asilomar Conference on Signals, Systems, and Computers*, pp. 1135–1139, Pacific Grove, Calif, USA, November 2000.
- [12] X. Mestre, "Improved estimation of eigenvalues and eigenvectors of covariance matrices using their sample estimates," *IEEE Transactions on Information Theory*, vol. 54, no. 11, pp. 5113–5129, 2008.
- [13] S. Björklund, P. Grahm, A. Nelander, and A. Alm, "Hot clutter reduction in radar. Measurement report for anechoic chamber measurements in spring 2000," Tech. Rep. FOA-R—00-01806-408—SE, 2000.
- [14] P. M. Techau, J. R. Guerci, T. H. Slocumb, and L. J. Griffiths, "Performance bounds for hot and cold clutter mitigation," *IEEE Transactions on Aerospace and Electronic Systems*, vol. 35, no. 4, pp. 1253–1265, 1999.
- [15] R. Cepeda, C. Vithanage, and W. Thompson, "From wideband to ultrawideband: channel diversity in low-mobility indoor environments," *IEEE Transactions on Antennas and Propagation*, vol. 59, no. 10, pp. 3882–3889, 2011.
- [16] L. Pettersson, M. Danestig, and U. Sjoström, "An experimental S-band digital beamforming antenna," *IEEE Aerospace and Electronic Systems Magazine*, vol. 12, no. 11, pp. 19–26, 1997.
- [17] S. Björklund and A. Heydarkhan, "High resolution direction of arrival estimation methods applied to measurements from a digital array antenna," in *Proceedings of the IEEE Sensor Array and Multichannel Signal Processing Workshop (SAM '00)*, pp. 464–468, Cambridge, Mass, USA, March 2000.
- [18] E. M. Friel and K. M. Pasala, "Effects of mutual coupling on the performance of STAP antenna arrays," *IEEE Transactions on Aerospace and Electronic Systems*, vol. 36, no. 2, pp. 518–527, 2000.
- [19] F. Haber and M. Zoltowski, "Spatial spectrum estimation in a coherent signal environment using an array in motion," *IEEE Transactions on Antennas and Propagation*, vol. AP-34, no. 3, pp. 301–310, 1986.
- [20] C. A. Balanis, *Antenna Theory. Analysis and Design*, John Wiley & Sons, New York, NY, USA, 2nd edition, 1997.
- [21] A. Farina, *Antenna-Based Signal Processing Techniques for Radar Systems*, Artech House, Norwood, Mass, USA, 1992.
- [22] J. Capon, "High-resolution frequency-wavenumber spectrum analysis," *Proceedings of the IEEE*, vol. 57, no. 8, pp. 1408–1418, 1969.
- [23] W. F. Gabriel, "Using spectral estimation techniques in adaptive processing antenna systems," *IEEE Transactions on Antennas and Propagation*, vol. AP-34, no. 3, pp. 291–300, 1986.
- [24] V. U. Reddy, A. Paulraj, and T. Kailath, "Performance analysis of the optimum beamformer in the presence of correlated sources and its behavior under spatial smoothing," *IEEE Transactions on Acoustics, Speech, and Signal Processing*, vol. 35, no. 7, pp. 927–936, 1987.
- [25] M. Zatman, "How narrow is narrowband?" *IEE Proceedings—Radar, Sonar and Navigation*, vol. 145, no. 2, pp. 85–91, 1998.
- [26] S. Björklund, "Hot clutter reduction in radar. Experimental design for anechoic chamber measurements," Technical Report FOA Memo 00-3316/L, 2000.
- [27] J. R. Guerci and J. S. Bergin, "Principal components, covariance matrix tapers, and the subspace leakage problem," *IEEE Transactions on Aerospace and Electronic Systems*, vol. 38, no. 1, pp. 152–162, 2002.

## Research Article

# A Parasitic Array Receiver for ISAR Imaging of Ship Targets Using a Coastal Radar

**Fabrizio Santi and Debora Pastina**

*Department of Information Engineering, Electronics and Telecommunications, University of Rome "La Sapienza",  
Via Eudossiana 18, 00184 Rome, Italy*

Correspondence should be addressed to Fabrizio Santi; [santi@diet.uniroma1.it](mailto:santi@diet.uniroma1.it)

Received 15 April 2016; Accepted 12 June 2016

Academic Editor: Michelangelo Villano

Copyright © 2016 F. Santi and D. Pastina. This is an open access article distributed under the Creative Commons Attribution License, which permits unrestricted use, distribution, and reproduction in any medium, provided the original work is properly cited.

The detection and identification of ship targets navigating in coastal areas are essential in order to prevent maritime accidents and to take countermeasures against illegal activities. Usually, coastal radar systems are employed for the detection of vessels, whereas noncooperative ship targets as well as ships not equipped with AIS transponders can be identified by means of dedicated active radar imaging system by means of ISAR processing. In this work, we define a parasitic array receiver for ISAR imaging purposes based on the signal transmitted by an opportunistic coastal radar over its successive scans. In order to obtain the proper cross-range resolution, the physical aperture provided by the array is combined with the synthetic aperture provided by the target motion. By properly designing the array of passive devices, the system is able to correctly observe the signal reflected from the ships over successive scans of the coastal radar. Specifically, the upper bounded interelement spacing provides a correct angular sampling accordingly to the Nyquist theorem and the lower bounded number of elements of the array ensures the continuity of the observation during multiple scans. An *ad hoc* focusing technique has been then proposed to provide the ISAR images of the ships. Simulated analysis proved the effectiveness of the proposed system to provide top-view images of ship targets suitable for ATR procedures.

## 1. Introduction

The monitoring and protection of the coastal area are a primary task to improve the situation awareness in the maritime domain and considerably efforts have been made over the last years to improve the levels of safety and security by using available monitoring and control systems [1]. Ground-based, airborne, and spaceborne radar sensors play a fundamental role in the framework of maritime surveillance, due to their capability to detect, track, and possibly image ship targets autonomously and continuously, night and day and even in hard meteorological conditions. As well as the employment of active radar systems, over the last years a number of studies concerning passive radar systems for marine applications have been conducted, essentially motivated by the well-known benefits of passive radars. Indeed, since only the receiver has to be designed and developed, such kind of systems is extremely of low cost if compared to conventional

active systems. Typically, they have small dimensions and hence can be deployed in place where heavy conventional radars cannot be. In addition, since they do not emit any waves, they provide increased antijamming capabilities as well as reduced environmental pollution. In the field of maritime surveillance, different opportunity illuminators have been proved able to increase safeguarding coastlines, such as geostationary telecommunication satellites [2, 3], digital terrestrial television transmitters [4, 5], and WiMAX [6] and cell phone [7] base stations. On the other hand, since the transmitted waveforms are designed for different purposes, they are not optimal for radar applications. A different solution is to exploit the signals emitted by opportunistic radar.

Traditionally, the control of the traffic along the coast is accomplished by the use of a ground-based radar system having its antenna rotating with a speed of 10–30 rpm, azimuth beamwidth of 0.4–2°, and a range resolution of few meters. Moreover, they are often equipped with a second antenna

able to receive the Automatic Identification System (AIS) signal transmitted by cooperative vessels, which provides to the marine traffic coordinator their unique identifiers, as well as their courses and speeds. However, information as much as possible has to be gathered about noncooperative targets, which may be involved in illegal activities such as piracy, human smuggling, or terrorist actions. Furthermore, small-sized vessels often do not carry an AIS transponder, and they could potentially increase the insurgence of accidents. Automatic Target Recognition (ATR) procedures greatly help maritime safety and security organizations, and often they rely on radar images. Nevertheless, the antenna angle resolution of a coastal radar is not sufficient to provide an image suitable for the recognition of the detected ship. However, by exploiting the well-known principle of the Inverse Synthetic Aperture Radar (ISAR) [8, 9], radar images with sufficient resolution for recognition can be obtained and employed in ATR procedures [10]. In this work, we consider a parasitic radar system that exploits the friendly emissions of a coastal radar in order to provide ISAR images of ship targets.

As is well known, ISAR technique exploits the ship movements with respect to the stationary radar to produce an image of the ship itself. Usually, the rotational motion of the ship around its center of gravity induced by the sea waves is exploited to produce the Doppler gradient needed to achieve the desired cross-range resolution. However, in the case of low sea-state this ship rotation can be negligible or not sufficient for the formation of the ISAR image. In such a case, it is of interest to develop an ISAR mode relying on the translational motion only. As typical ship velocities are limited to about twenty knots (about 10 m/s), ship reflected signals have to be integrated over a long integration time to achieve an ISAR image with reasonable resolution. While the radar antenna rotates, it illuminates the target for a time interval given by the time-on-target. Typical values of the scan rates and azimuth beam widths for a coastal radar entail times-on-target of tens of milliseconds, certainly too short for imaging purposes. Nevertheless, the target is again illuminated after a time interval equal to the time needed to the antenna to complete a scan, and by exploiting the signal reflected by the ship over successive scans, a processing time long enough for the ISAR process can be obtained. On the other hand, the usual values of the scan rates of the coastal radar give rise to sampling frequencies considerably lower than the Doppler bandwidth and therefore the coastal radar by itself cannot carry out a proper sampling of the azimuth signal.

The solution proposed here to achieve a proper sampling of the signal in the azimuth domain is to use an array of passive sensors located near the coast receiving the signal transmitted by the coastal radar over its successive scans (and otherwise not involved in the imaging activity) and reflected by the ship. The proper configuration of the array parameters, that is, number of elements and their reciprocal distance, is therefore linked to the parameters of the coastal radar as well as the target motion (a preliminary assessment of the system has been presented in [11]). Then, by jointly exploiting the physical aperture provided by the parasitic array and the synthetic aperture based on the target motion, a proper

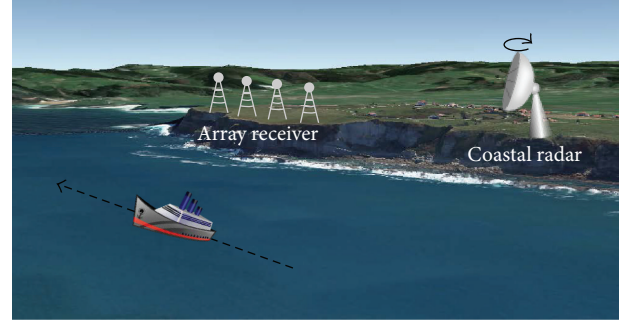


FIGURE 1: Operative scenario.

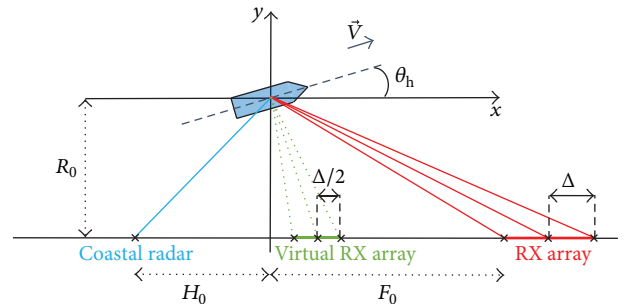


FIGURE 2: Top view of the system geometry.

processing of the data provides a well-focused image to be efficiently employed in ATR procedures.

The remainder of the paper is organized as follows: Section 2 describes the geometry of the system and the signal model; the receiver array configuration is derived in Section 3 and the data processing in Section 4; simulated results are provided in Section 5 and Section 6 concludes the paper.

## 2. System Geometry and Echo Model

The operative scenario is depicted in Figure 1. A coastal radar working in X-band (wavelength  $\lambda = 3$  cm) monitors the littoral traffic. An array of passive devices is located near the coast, collecting the signal transmitted from the coastal radar and reflected from a moving ship. The ship is modeled as a rigid body in the far field characterized by  $K$  dominant scattering centers with complex reflectivity constant along the length of synthetic aperture. The ship is assumed moving with translation motion and negligible rotations (i.e., low sea-state conditions).

The geometry of the system is depicted in Figure 2. For the sake of simplicity in the subsequent derivation, we consider the elements of the array receiver and the coastal radar aligned along the  $x$  direction. Within this reference system, coastal radar coordinates are given by

$$\begin{aligned} x_{\text{TX}} &= -H_0, \\ y_{\text{TX}} &= -R_0, \\ z_{\text{TX}} &= Z_T. \end{aligned} \quad (1)$$

Let  $N$  be the number of elements of the array and  $\Delta$  the interelement distance, and the  $n$ th receiving element position ( $n = 1, \dots, N$ ) is

$$\begin{aligned} x_{\text{RX}^n} &= F_0 + (n-1)\Delta, \\ y_{\text{RX}^n} &= -R_0, \\ z_{\text{RX}^n} &= Z_R. \end{aligned} \quad (2)$$

The coastal radar illuminates the target each  $T_{\text{scan}}$  seconds, whose value depends on the rotation speed of its antenna. Let  $M$  be the number of processed scans and let  $\vec{V}$  be the target velocity vector, and the  $k$ th scatterer position at the  $m$ th scan ( $m = -M/2, \dots, M/2 - 1$ ) is given by

$$\begin{aligned} x_k(m) &= x_k^0 + |\vec{V}| \cos(\theta_h) m T_{\text{scan}}, \\ y_k(m) &= y_k^0 + |\vec{V}| \sin(\theta_h) m T_{\text{scan}}, \end{aligned} \quad (3)$$

where  $\theta_h$  is the target heading angle and  $(x_k^0, y_k^0)$  are the scatterer coordinates at the central scan instant.

Without loss of generality, we assume the target reference point located in  $(x_0^0, y_0^0) = (0, 0)$ . For such a scatterer, the signal received from the  $n$ th array element during the  $m$ th scan is given by

$$s_0(m, n) = A_0 \cdot \exp \left\{ -j \frac{2\pi}{\lambda} [R_{\text{TX}}(m) + R_{\text{RX}^n}(m)] \right\}, \quad (4)$$

where  $R_{\text{TX}}(m)$  and  $R_{\text{RX}^n}(m)$  are the target to transmitter and target to  $n$ th receiver distances, respectively, and  $A_0$  is its complex amplitude. By expanding the bistatic ranges in (4) in Taylor series and stopping at second order, we obtain

$$\begin{aligned} s_0(m, n) &\cong A_0 \cdot \exp \left\{ -j \frac{2\pi}{\lambda} \left[ (\sigma_{\text{TX}} + \sigma_{\text{RX}^n}) \right. \right. \\ &\quad \left. \left. + (\alpha_{\text{TX}} + \alpha_{\text{RX}^n}) \cdot m T_{\text{scan}} + \frac{1}{2} (\beta_{\text{TX}} + \beta_{\text{RX}^n}) \right. \right. \\ &\quad \left. \left. \cdot (m T_{\text{scan}})^2 \right] \right\}. \end{aligned} \quad (5)$$

Let  $V_x = |\vec{V}| \cos(\theta_h)$  and  $V_y = |\vec{V}| \sin(\theta_h)$  be the target velocity components along the  $x$  and  $y$  directions, respectively, and the polynomial phase coefficients in (5) are as follows:

$$\begin{aligned} \sigma_{\text{TX}} &= \sqrt{H_0^2 + R_0^2 + Z_T^2}, \\ \sigma_{\text{RX}^n} &= \sqrt{(F_0 + (n-1)\Delta)^2 + R_0^2 + Z_R^2}, \\ \alpha_{\text{TX}} &= \frac{H_0 V_x + R_0 V_y}{\sigma_{\text{TX}}}, \\ \alpha_{\text{RX}^n} &= \frac{-(F_0 + (n-1)\Delta) V_x + R_0 V_y}{\sigma_{\text{TX}}}, \end{aligned}$$

$$\begin{aligned} \beta_{\text{TX}} &= \frac{(H_0 V_y + R_0 V_x)^2}{\sigma_{\text{TX}}^3}, \\ \beta_{\text{RX}^n} &= \frac{((F_0 + (n-1)\Delta) V_y + R_0 V_x)^2}{\sigma_{\text{RX}^n}^3}. \end{aligned} \quad (6)$$

It is worth to explicitly notice that in practice the altitudes of both transmitter and receiving array,  $Z_T$  and  $Z_R$ , respectively, are considerably lower than the target distance. Consequently, the only effect of the difference among the transmitter, receiver, and target heights is a slight difference between the ground plane and the image (i.e., slant) plane. Therefore, in the following for the sake of clearness we refer to the coplanar geometry.

Finally from (5)-(6), it is easy to obtain the expression of the received signal from the  $k$ th scatterer  $s_k(m, n)$  by replacing  $H_0$  with  $H_k = H_0 + x_k^0$ ,  $F_0$  with  $F_k = F_0 - x_k^0$ , and  $R_0$  with  $R_k = R_0 + y_k^0$ .

### 3. Design of the Array

In order to design the array, we have to set the number of its elements and their distances. The configuration has to allow obtaining an ISAR image of the ship with proper cross-range resolution. The achievable cross-range resolution  $\rho_{\text{cr}}$  depends on the overall view angle  $\Delta\theta$  observed during the aperture time  $T_a$  [9]:

$$\rho_{\text{cr}} = \frac{\lambda}{2\Delta\theta}. \quad (7)$$

For a target at distance  $R_0$  moving with velocity component  $V_x$  along the  $x$  direction,  $\Delta\theta$  is given by

$$\Delta\theta = \frac{T_a |V_x|}{R_0}. \quad (8)$$

In the framework of coastal surveillance, typical speeds of the targets of interest are in the order of 1–20 kt and the range is in the order of tens of kilometers. It is easy to verify that we need aperture times in the order of ten seconds to reach resolution values suitable to provide images to be employed in ATR procedures. Since the radar antenna rotates with speed of about 10–30 rpm,  $T_{\text{scan}}$  is 2–6 s, and hence we need to observe the target for  $M$  successive scans. Therefore, in order to obtain a desired value  $\rho_{\text{cr}}$  of cross-range resolution, we need to form a synthetic aperture over a number of scans given by

$$M = \frac{\lambda R_0}{2\rho_{\text{cr}} T_{\text{scan}} |V_x|}. \quad (9)$$

The Doppler bandwidth provided by the target can be written as

$$B_d = \frac{4|V_x|}{\lambda} \sin\left(\frac{\Delta\theta}{2}\right) \approx \frac{2|V_x|\Delta\theta}{\lambda} = \frac{|V_x|}{\rho_{\text{cr}}}. \quad (10)$$

Its inverse is the sampling period requested by the Nyquist theorem. Through its rotations, the coastal radar operates a sampling of the signal with a period equal to  $T_{\text{scan}}$ , which is greater than  $\rho_{\text{cr}}/|V_x|$  for practical situations. For example, if we aim at obtaining a resolution of 2 m for a target moving with tangential velocity 2.5 m/s ( $\approx 5$  kt),  $T_{\text{scan}}$  should be 0.8 s that would require the antenna rotating with a speed of 75 rpm, much greater than the rotation speeds commonly employed by coastal radars.

Nevertheless, due to their physical distance, the  $(n + 1)$ th element of the array will receive the samples with a delay with respect to the  $n$ th element, and this delay is given by

$$\tau = \frac{1}{2} \frac{\Delta}{|V_x|}. \quad (11)$$

In the above equation, the coefficient 1/2 is due to the bistatic geometry of the system. Indeed, since a bistatic acquisition is equivalent to a monostatic acquisition located on the bisector between the transmitter and receiver line-of-sights [12–14], a virtual array of  $N$  elements having interelement spacing equal to half of the physical distance is achieved; see Figure 2.

Since the Nyquist theorem requires  $\tau \leq B_d^{-1}$ , we have to impose a maximum distance between the elements of the array; by carrying out the calculus, from (9), (10), and (11) we found that  $\Delta$  has to be at least twice the desired cross-range resolution:

$$\Delta \leq \frac{\lambda R_0}{MT_{\text{scan}} |V_x|} = 2\rho_{\text{cr}}. \quad (12)$$

Therefore, we can set  $\Delta = 2\rho_{\text{cr}}/\mu$ , where  $\mu \geq 1$ .

As previously discussed, in order to increase the azimuth resolution, the target is observed for  $M$  successive scans. This imposes the time interval  $\Delta T$  covered by the array during the single-scan to be at least equal to  $T_{\text{scan}}$ , thus avoiding gaps between successive scans.  $\Delta T$  is  $N$  times  $\tau$ , and therefore, from (9) and (11)

$$N\tau \geq T_{\text{scan}} \implies N \geq \left\lceil 2\mu M \frac{T_{\text{scan}}^2 |V_x|^2}{\lambda R_0} \right\rceil, \quad (13)$$

where  $\lceil \cdot \rceil$  is the ceil operator needed to have an integer number of elements. From (12) and (13) we get the physical extension of the array; that is,

$$L_A = N\Delta = 2T_{\text{scan}} |V_x|. \quad (14)$$

Finally, to complete the design of the array the value of  $\mu$  has to be set. The condition  $\mu = 1$  represents the less demanding configuration for the array, since it corresponds to having the minimum number of elements separated as much as possible. Nevertheless, the interelement distance affects the nonambiguous azimuth swath  $W$ . Indeed, the angular sampling  $\delta\theta$  is given by  $\Delta/2R_0$ , and from (9) and (12) we obtain

$$W = \frac{\lambda}{2\delta\theta} = \mu MT_{\text{scan}} |V_x| = \mu L_s, \quad (15)$$

$L_s = MT_{\text{scan}} |V_x|$  being the length of the synthetic aperture. In the event that, for a given  $\Delta$  value,  $N$  is the minimum number

of elements,  $L_s = (\Delta/2)MN$ , where the ceil operator in (13) has been neglected. Let  $D$  be the maximum size of the ship along the cross-range dimension; it must be

$$\mu \geq \frac{D}{L_s}. \quad (16)$$

As an example, let us consider a ship moving with  $|\vec{V}| = 5$  m/s along the positive  $x$  direction at a distance  $R_0 = 10$  km. A coastal radar with a scan rate of 20 rpm (corresponding to  $T_{\text{scan}} = 3$  s) detects and tracks the ship. We aim at obtaining an ISAR image of such target with  $\rho_{\text{cr}} = 2.5$  m. To the purpose, we need  $M = 4$  scans, (9), and the receiving array has to be composed by elements at a distance of  $5/\mu$  meters. By setting  $\mu = 1$  and choosing for  $N$  the minimum allowed value, we obtain an array of 6 elements at a distance of 5 m. In such conditions, the array is able to correctly sample the signal over the whole aperture time, and by the proper processing of the data (addressed in the following section), the ISAR image can be obtained. However, the choice  $\mu = 1$  entails an azimuth swath equal to 60 m and target with size larger than such a value will suffer from aliasing effects. If  $D = 100$  m, we have to set  $\mu \geq 1.67$  to have a sufficient large swath. For example, by setting  $\mu = 2$ , we obtain an array of 12 elements with interelement distance 2.5 m able to image unambiguously target of maximum length 120 m at 10 km range.

As it has been shown by the above equations, for given transmitter parameters of the coastal radar, the array design depends on the parameters of the target, specifically on its distance from the radar system  $R_0$  and on its tangential velocity  $|V_x|$ . Obviously, the array has to be designed in order to fulfill the imaging requirements for the most demanding cases, represented by the shorter distance and the faster target. Let  $|\vec{V}| = 10$  m/s ( $\approx 20$  kt) be the maximum speed considered for the ship targets of interest, and suppose the system surveying a large corridor going from  $R_{\text{min}} = 4$  km till  $R_{\text{max}} = 20$  km range. Furthermore, we assume a maximum extent of the ship  $D = 100$  m. Figure 3 shows the main parameters of the array for the different distance and tangential velocity couples for the case of a coastal radar with  $T_{\text{scan}} = 3$  s. As we expected, the maximum number of elements at the lowest interelement distance is obtained for the target moving at the maximum speed and at the minimum distance at the same time. In such a situation, we have to configure an array with 50 elements with spacing 1.2 m.

Let us now consider a target moving at a distance greater than  $R_{\text{min}}$ . Since  $W = \lambda R_0/\Delta$ , a larger azimuth swath will be obtained, therefore allowing to correctly image targets with  $D > 100$  m. On the other hand, for a given target velocity and number of integrated scans, a worse resolution is obtained, (7) and (8). However, by increasing the number of integrated scans, desired resolution values can be reached.

Then, we analyze the case of a target moving with a velocity lower than the maximum considered value for which the array has been configured. As it has been previously discussed, the delay experienced by two adjacent elements of the array is related to the tangential velocity of the target, (11), and during a scan, the array covers a time interval equal to  $N\tau$ . In the event that  $\Delta T = N\tau > T_{\text{scan}}$ , during the  $(m + 1)$ th

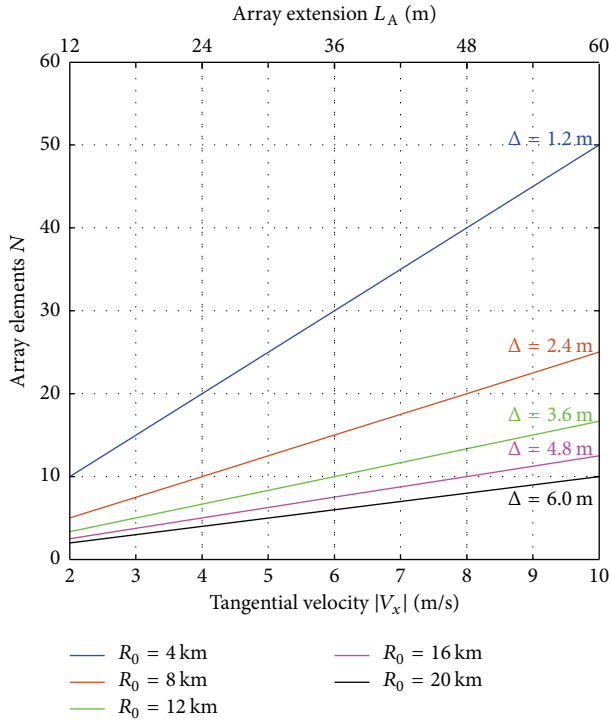


FIGURE 3: Array parameters as a function of the target parameters ( $T_{\text{scan}} = 3$  s).

scan the last elements of the array are still receiving the target contributions due to the transmissions carried out at the  $m$ th scan. Therefore, as it has been sketched in Figure 4, in the time domain an overlapping between signals received by the array during successive scans will occur. Specifically, let  $N_{\text{eq}}$  be the number of elements such that  $N_{\text{eq}}\tau = T_{\text{scan}}$ , the signals received by the last  $(N - N_{\text{eq}})$  elements of the array during the  $m$ th scan overlap in time with the signals received by the first  $N_{\text{eq}}$  elements of the array during the  $(m + 1)$ th scan. Consequently, in order to achieve a contiguous sampling of the azimuth signal over  $M > 1$  scans, only the first  $N_{\text{eq}}$  elements of the array should be considered. It should be pointed out that, in general,  $N_{\text{eq}}$  is not an integer number, and a fractioned number of elements of the array should be selected. Such a problem can be faced by carrying out a proper interpolation of the data, as it will be detailed in describing the array data processing.

#### 4. Array Data Processing

In this section, we present the processing of the data received from the array to achieve the ISAR image of the target. Section 4.1 deals with the case of a monodimensional azimuth signal. The objective of the subsection is to illustrate the proof of concept and highlight the main operations involved in the azimuth compression. Based on the concepts illustrated in Section 4.1, the focusing technique for a distributed target is detailed in Section 4.2.

**4.1. Monodimensional Azimuth Signal Proof of Concept.** Let us assume a single scatterer located in  $(x_k^0, y_k^0)$  at the reference time, and suppose we aim at focusing it as observed in a single scan. To the purpose, we need to compensate the phase shift of the target as it moves through the aperture. Due to the geometry of the system, we have two contributions. The former is due to the transmitter-target distance, and it is the same for all the elements of the receiving array. The latter is due to the target-receiver distance, and it varies with the element index. The azimuth compression is therefore obtained by multiplying the data received by each element of the array for the complex conjugate of a common reference signal given by

$$s_{\text{TX}}^{\text{ref}} = \exp \left\{ -j \frac{2\pi}{\lambda} \left[ a_0 + a_1 m T_{\text{scan}} + \frac{a_2}{2} (m T_{\text{scan}})^2 \right] \right\} \quad (17)$$

and then, for the  $n$ th element, by multiplying the data for the complex conjugate of the reference signal given by

$$s_{\text{RX}^n}^{\text{ref}} = \exp \left\{ -j \frac{2\pi}{\lambda} \left[ b_0^{(n)} + b_1^{(n)} m T_{\text{scan}} + \frac{b_2^{(n)}}{2} (m T_{\text{scan}})^2 \right] \right\}. \quad (18)$$

The coefficients  $(a_0, \dots, a_2, b_0^{(n)}, \dots, b_2^{(n)})$  are the coefficients of the Taylor expansion of the bistatic distances for the scatterer located in  $(x_k^0 = 0, y_k^0)$ , which can be obtained from (6) by replacing  $R_0$  with  $R_k = R_0 + y_k^0$ . Thereby, the compensation of the linear phase terms will result in a residual Doppler centroid related to the  $k$ th scatterer position in the azimuth domain. It should be also pointed out that, as usual in ISAR processing, we neglect the variation of the Doppler rate with the cross-range position of the scatterer while, as stated above, we take into account its variation along the range direction. Then, by applying a FFT the scatterer ISAR profile can be obtained.

Now, we aim at focusing the target observed over a number of successive scans. As discussed in Section 3, in general the data received by the array during successive scans overlap in time, and the selection of the first  $N_{\text{eq}}$  elements of the array must be performed. Since such a number being an integer number cannot be ensured, a proper interpolation of the data must be performed in order to artificially increase the time sampling. This task can be easily accomplished by zero padding. After the data corresponding to the  $m$ th scan have been compressed by multiplying the array data for the reference signals (17) and (18), a zero padding is performed in the frequency domain. Let  $q$  be the oversampling factor and the sampling time is  $\tau/q$ ; for  $q$  values high enough, we can assume  $qN_{\text{eq}} \cong \lceil qN_{\text{eq}} \rceil$ , and therefore a more precise selection of the data can be performed, thus ensuring a contiguous time observation among successive scans. After the time oversampling and selection of the data have been performed, vector signals  $\mathbf{s}_m^{\text{int}}$  with dimension  $[1 \times qN_{\text{eq}}]$  can be obtained by interleaving the data corresponding to each scan. Two different strategies could be adopted to merge the data received over the successive scans to provide the increased cross-range resolution. The former operates in the time domain and it

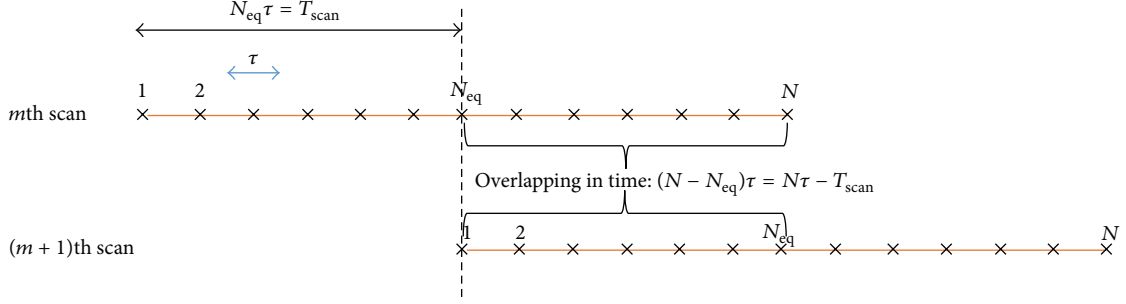


FIGURE 4: Time intervals covered by the array over successive scans.

consists in placing side by side the single-scan data to obtain the final vector  $\mathbf{s}_{\text{TOT}}^{\text{int}} = [\mathbf{s}_1^{\text{int}}, \dots, \mathbf{s}_M^{\text{int}}]$ ; a FFT can be subsequently applied thus obtaining the multiscan ISAR profile.

The latter strategy operates in the frequency domain. The single-scan ISAR profile can be obtained by applying a FFT to each  $\mathbf{s}_m^{\text{int}}$  after they have been temporarily aligned. To this purpose, for each scan a FFT can be applied to the vector  $\tilde{\mathbf{s}}_m^{\text{int}} = [\mathbf{z}_m^{\text{left}}, \mathbf{s}_m^{\text{int}}, \mathbf{z}_m^{\text{right}}]$ , where  $\mathbf{z}_m^{\text{left}}$  and  $\mathbf{z}_m^{\text{right}}$  are zero vectors with dimensions  $[1 \times qN_{\text{eq}}(m-1)]$  and  $[1 \times qN_{\text{eq}}(M-m)]$ , respectively. Then, by coherent summation of the single-scan profiles, the multiscan ISAR profile is obtained.

So far, we considered completely negligible target rotations. This is reasonable in our hypothesis of low sea-state conditions, and the imaging of rotating ships could be addressed by conventional ISAR techniques or by using formations of active and passive radar sensors to reach high resolution products [13, 14]. Nevertheless, even though they are limited, rotations may affect the imaging technique here proposed. Therefore, the case in which the target motion is characterized also by rotations is here discussed. In the case of a jointly translating and rotating target,  $k$ th scatterer coordinates (3) can be rewritten in matrix notation as

$$\begin{bmatrix} x_k(m) \\ y_k(m) \end{bmatrix} = \begin{bmatrix} x_k^0 \\ y_k^0 \end{bmatrix} \begin{bmatrix} \cos(\omega m T_{\text{scan}}) & \sin(\omega m T_{\text{scan}}) \\ -\sin(\omega m T_{\text{scan}}) & \cos(\omega m T_{\text{scan}}) \end{bmatrix} + \begin{bmatrix} V_x m T_{\text{scan}} \\ V_y m T_{\text{scan}} \end{bmatrix}, \quad (19)$$

where  $\omega$  is the rotation speed. By carrying out the calculus, we can write scatterer coordinates as

$$\begin{aligned} x_k(m) &= \{x_k^0 [\cos(\omega m T_{\text{scan}}) - 1] + y_k^0 \sin(\omega m T_{\text{scan}})\} \\ &\quad + \{x_k^0 + V_x m T_{\text{scan}}\} = x_k^V(m) + x_k^\omega(m), \\ y_k(m) &= \{y_k^0 [\cos(\omega m T_{\text{scan}}) - 1] - x_k^0 \sin(\omega m T_{\text{scan}})\} \\ &\quad + \{y_k^0 + V_y m T_{\text{scan}}\} = y_k^V(m) + y_k^\omega(m) \end{aligned} \quad (20)$$

$x_k^V$  and  $y_k^V$  being the target coordinates for the only-translating target and  $x_k^\omega$  and  $y_k^\omega$  the shifts due to the rotation.

As pointed out, the dwell time during a single scan is due to the ratio between the antenna beamwidth and the scan rate. For example, an antenna with rotation rate of 20 rpm and beamwidth  $0.6^\circ$  provides a time-on-target of 5 ms. In such a limited interval, target rotation can be neglected and therefore the rotations do not affect the imaging processing within a single scan. Nevertheless, the rotation causes a Doppler shift experienced by the data received among the successive scans, deriving from the different orientations of the target. Such a Doppler shift can be written as

$$\Delta f_k(m) = \frac{2}{\lambda} \frac{V_x}{R_0} \delta_k^{\text{cr}}(m), \quad (21)$$

where  $\delta_k^{\text{cr}}(m)$  represents the cross-range shift due to the difference in cross-range position with respect to the nominal position accounting only for the translation; that is,  $\delta_k^{\text{cr}}(m) = x_k^\omega(m)$ . The compensation of this Doppler shift corresponds to performing a coregistration among the single-scan responses, which can be obtained by multiplying  $\tilde{\mathbf{s}}_m^{\text{int}}$  for a phase ramp  $\exp\{j2\pi\Delta f_k(m)\tilde{\mathbf{n}}\}$ ,  $\tilde{\mathbf{n}}$  being the vector of time instants going from  $-(M/2)T_{\text{scan}}$  to  $(M/2)T_{\text{scan}}$  with step  $(1/q)(\Delta/2|V_x|)$ .

Furthermore, the rotation causes a different range of the scatterer with respect to the one foreseen by the translational motion only. Such a difference in range entails phase jumps among the different scans to be compensated. Therefore, the single-scan data  $\tilde{\mathbf{s}}_m^{\text{int}}$  have to be further multiplied by a term given by

$$\Delta \xi_k(m) = \exp\left\{\frac{j2\pi}{\lambda} \delta_k^{\text{r}}(m)\right\} \quad (22)$$

with  $\delta_k^{\text{r}}(m) = y_k^\omega(m)$ .

**4.2. Focusing Technique for Distributed Target.** In previous section, we considered the case of a monodimensional signal in order to illustrate the main concept to obtain the multiscan ISAR profile. It has been shown that the crucial steps are azimuth dechirping, time selection, time alignment, and possible rotation compensations. Based on these considerations, the focusing technique for a distributed target is developed as depicted in Figure 5. It comprises two parts: first, data received by the array during each scan are processed; then,

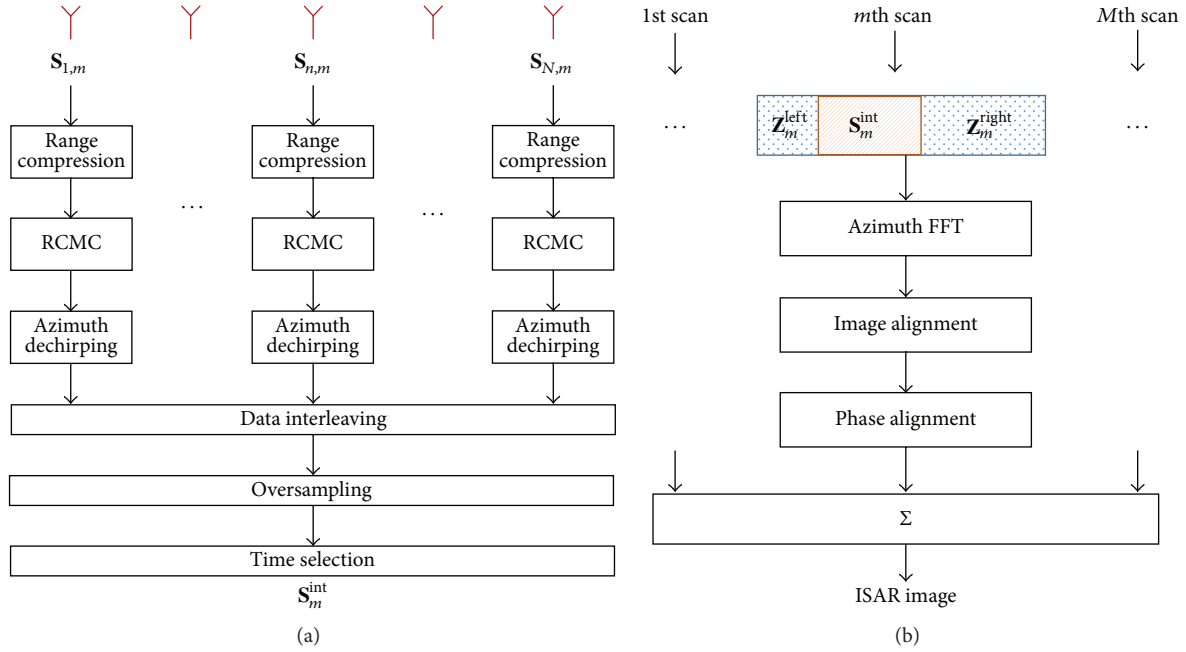


FIGURE 5: Processing scheme: (a) single-scan processing and (b) multiscan data fusion.

data received during multiple scans are merged to form the final image.

Accounting also for the fast time dimension, the data received from the  $n$ th sensor during the  $m$ th scan are organized in a matrix  $\mathbf{S}_{n,m}$ , with number of rows equal to the number of fast time samples and number of columns depending on the number of samples within the time-on-target. Taking into account the short duration of the time-on-target, we can neglect the variation among adjacent pulses collected by a single array element during a scan and therefore, for sake of simplicity, we assume that the  $n$ th receiver collects a single sample during the  $m$ th time-on-target for each range bin. Therefore,  $\mathbf{S}_{n,m}$  is a column vector of dimension  $[L \times 1]$ ,  $L$  being the number of range bins. The processing of the data received by the array during the  $m$ th scan consists of the following steps (see Figure 5(a)):

- (1) Range compression: allowing transiting in the slant range domain.
- (2) Range Cell Migration Correction (RCMC): due to the long integration time, the correction of the range migration is a needed step. It can be obtained in the fast frequency domain by multiplying the Fourier transformed data by a reference signal equal to  $\exp\{j2\pi f_r(\delta R_n^0(m)/c)\}$ .  $f_r$  is the fast frequency,  $c$  is the speed of light, and  $\delta R_n^0(m)/c$  is the time delay due to the variation of the distance between the target reference point and the central element of the array at the reference scan  $m = 0$  and the distance between the target reference point and the  $n$ th array element at the  $m$ th scan.
- (3) Azimuth dechirping: for the  $l$ th range bin, two reference signals as in (17) and (18) are generated, where

the coefficients  $(a_0, \dots, a_2, b_0^{(n)}, \dots, b_2^{(n)})$  account for the specific range bin position; namely, as explained in Section 4.1, in the Taylor coefficients (6) we have to replace  $R_0$  with  $R_0 + \bar{y}_l$ ,  $\bar{y}_l$  being the  $l$ th value of the range axis.

- (4) Data interleaving among the array elements: to obtain a data matrix  $\mathbf{S}_m^{\text{int}}$  of dimension  $[L \times N]$ .
- (5) Oversampling: as explained in the previous subsection, by means of Fourier transform and zero padding, an increased time sampling is obtained, and after the oversampling  $\mathbf{S}_m^{\text{int}}$  has dimension  $[L \times qN]$ .
- (6) Time selection: to ensure time continuity among the data collected by the successive scans, the first  $qN_{\text{eq}}$  columns of  $\mathbf{S}_m^{\text{int}}$  are selected. After this operation,  $\mathbf{S}_m^{\text{int}}$  has dimension  $[L \times qN_{\text{eq}}]$ . It should be pointed out that if the interest is in focusing the image resulting from a single scan, time selection can be bypassed, and through an azimuth FFT the single-scan image can be obtained.

At this point,  $M$  matrices  $\mathbf{S}_m^{\text{int}}$  are available covering a time interval equal to  $MT_{\text{scan}}$ . The following operations are performed to obtain the multiscan ISAR image (see Figure 5(b)):

- (1) Time shift: as explained in Section 4.1, for temporarily aligning the data received by each scan, the array data processed for the  $m$ th scan can be organized in the matrix  $[\mathbf{Z}_m^{\text{left}}, \mathbf{S}_m^{\text{int}}, \mathbf{Z}_m^{\text{right}}]$ ,  $\mathbf{Z}_m^{\text{left}}$  and  $\mathbf{Z}_m^{\text{right}}$  being zero matrices with dimension  $[L \times qN_{\text{eq}}(m-1)]$  and  $[L \times qN_{\text{eq}}(M-m)]$ , respectively.
- (2) Single-scan images formation: by applying a FFT along the azimuth dimension, the ISAR image corresponding to the  $m$ th scan is achieved. Thanks to

the time-shift operation, the images correspond to the same time interval, and, in the event that rotation motion can be neglected, a coherent summation provides the ISAR image with  $M$  times finer (with respect to the single-scan images) cross-range resolution. However, since, in general, ship targets undergo rotations, their effects have to be compensated as explained in steps (3) and (4).

- (3) Image coregistration: the short duration of the time-on-target allows considering each single-scan image as a “snapshot” of the target, and the possible rotation motion does not affect the imaging processing [15]. However, such a rotation motion causes the target to change its orientation when imaged at different scans, and hence the series of single-scan images can be regarded as snapshots of the same target that has changed its orientation. Therefore, a rotation of the  $m$ th scan image accordingly to an angle equal to  $\omega m T_{\text{scan}}$  has to be performed. It should be pointed out that such an image alignment also compensates the Doppler shift (21) experienced by each scatterer.
- (4) Phase alignment: as it is shown by (22), the  $k$ th scatterer of the scene undergoes a phase jump when imaged in different scans, and, since  $\delta_k^v(m) = y_k^\omega(m)$  is a function of both cross-range and range positions, (20), a space variant phase compensation has to be performed. Let  $\bar{y}_l$  be the  $l$ th range bin value and let  $\bar{x}_h$  be the  $h$ th cross-range bin value; for the  $m$ th scan a phase matrix with elements  $\Delta \xi_{l,h}^f(m) = \exp\{(j2\pi/\lambda)\delta_{l,h}^f(m)\}$ , with  $\delta_{l,h}^f(m) = \bar{y}_l[\cos(\omega m T_{\text{scan}}) - 1] - \bar{x}_h \sin(\omega m T_{\text{scan}})$ , can be generated. By multiplying cell by cell the  $m$ th scan image for such a matrix, the space variant phase compensation can be accomplished.
- (5) Coherent summation: finally, the temporarily aligned, coregistered, and phase aligned single-scan images can be coherently added to form the final multiscan ISAR image.

Finally, it is worth to mention that the described focusing technique accounts for an *a priori* known target motion. Generally, with particular regard to the imaging of noncooperative targets, the motion parameters have to be retrieved directly by the received data, and generally speaking many contributions can be found in the literature dealing with the estimation of the translational and rotational motion of ship targets. Even though the target motion estimation is beyond the goal of this paper, which mainly focuses on the definition of the array parameters and of a suitable processing of the received data, we want here to outline possible strategies to address the issue.

Typically, ISAR requires the compensation of the translational motion between the radar and the target (i.e., motion compensation): largely employed techniques are based on the maximization/minimization of proper cost functions with respect to the unknown translational motion [8], such as the maximization of the contrast [16] or the minimization of the entropy [17]. In our case, the same concept can be adequately applied, where the ship translation can be estimated

maximizing the intensity contrast of the set of single-scan ISAR images. In this regard, it is also worth to notice that typical ship translations implicate low terms of the received phase; therefore acceleration and higher order terms could be reasonably neglected for the single-scan autofocus and do not need to be estimated, thus alleviating the computation burden for this issue.

Regarding the rotational motion, as it has been pointed out in describing the image coregistration procedure, in the proposed system the ship rotations only entail an additional change in the orientation of the ship when imaged in successive scans. The estimation of this additional scan-to-scan rotation can be addressed maximizing proper cost functions on the final image [18] or looking for that angle providing the best alignment among the single-scan images (taking also into account the misalignment due to translation as estimated from the previous step). A promising alternative could be the estimation of the slope of the ship centerline [10], which is a function of the rotation rate as detailed in [19]. Lastly, it is also worth to underline that the proposed imaging technique mainly addresses those scenarios where the low sea-state conditions entail very limited rotations of the ship, thus making the formation of ISAR images with proper resolution hard with conventional techniques. In this work, we accounted for a possible not negligible yaw motion of the ship, since it could also account for an initial target maneuver. In contrast, complicated ship dynamics involving nonnegligible three-dimensional rotations would not require multiple scans and therefore can be treated by resorting to conventional ISAR techniques.

## 5. Simulated Results

In the simulated analysis, we consider an X-band fully solid state coastal radar for vessel traffic services, operating with a scan rate of 20 rpm and transmitting a chirp signal with a bandwidth of 22 MHz [20]. An array of 50 elements with spacing 1.2 m is configured, allowing imaging targets of maximum length 100 m, at a maximum speed of 10 m/s and at ranges longer than 4 km.

In a first case study, we consider a target moving with velocity  $|\vec{V}| = 10$  m/s and heading angle  $\theta_h = 60^\circ$  at a distance  $R_0 = 8$  km, and we consider the target observed over 4 scans. Since  $|V_x| = 5$  m/s, during a scan the array covers a time interval twice that of the scan interval, and therefore, to combine the signals received over the successive scans, proper time selection has to be performed. In particular, since  $\Delta T = 2T_{\text{scan}}$ , in this case  $N_{\text{eq}} = (1/2)N$ . By considering a single pointlike scatterer located in (30, 0) m at the reference time and applying the processing described in Section 4.1, the cross-range profiles shown in Figure 6 are obtained, when one or more scans have been integrated. As we can observe, cross-range resolution progressively increases by integrating the signals received by the array over an increased number of scans. Specifically, we found  $\rho_{\text{cr}} = 8$  m, 6 m, 4 m, 2 m when  $M = 1, 2, 3, 4$ , respectively, in agreement with the theoretical expectations. It should be pointed out that if a single scan is considered, time selection step could be avoided, and the whole time interval  $\Delta T$  covered by the array could be

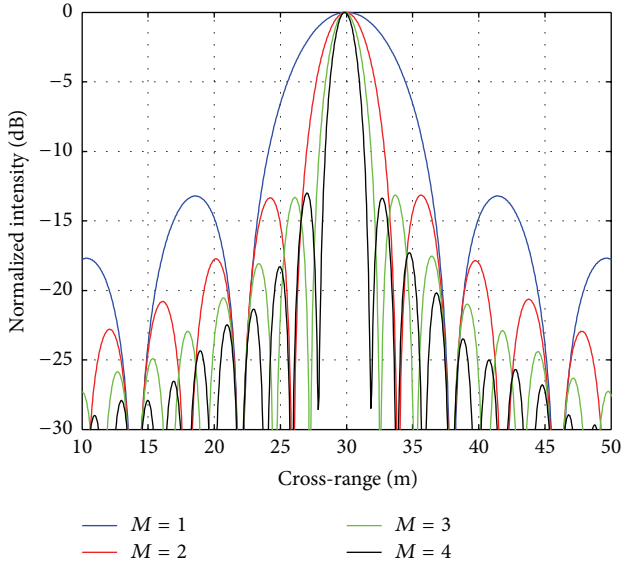


FIGURE 6: ISAR profiles for successive integrated scans.

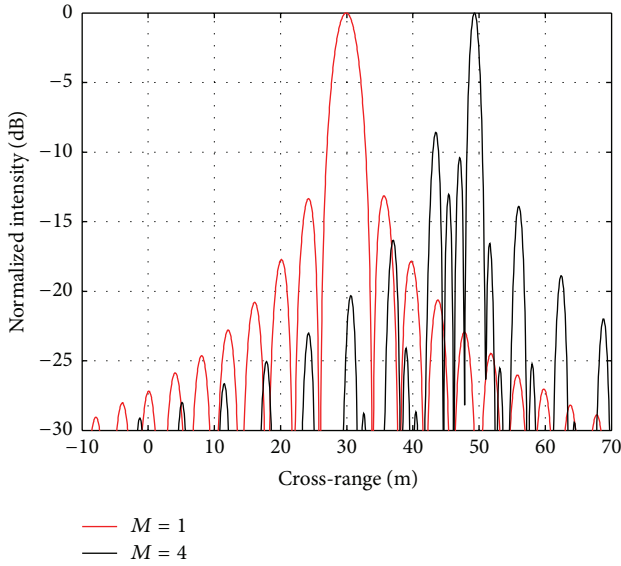


FIGURE 7: ISAR profiles obtained without applying the time selection.

processed. Since, in this particular scenario,  $\Delta T$  is twice  $T_{\text{scan}}$ , the case  $M = 1$  without time selection provides the same imaging results as the case  $M = 2$  with time selection. Nevertheless, to further increase the resolution by combining  $M > 2$  scans, time selection is essential. As example, Figure 7 shows the results obtained without the time selection step for the cases  $M = 1$  and  $M = 4$ . In the former case, we can observe the same profile achieved in Figure 6 for  $M = 2$ , whereas in the latter, as a consequence of the time overlapping, we observe the scatterer not correctly focused.

The hypothesis of absence of rotation motion is then removed considering the target undergoing a rotation motion with an angular velocity  $\omega = 0.5^\circ/\text{s}$ . We assume the target observed for  $M = 3$  scans and we consider an isolated point

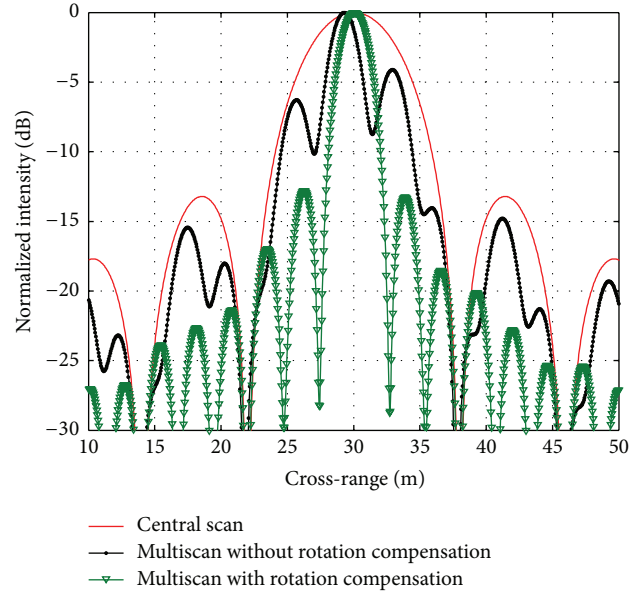


FIGURE 8: ISAR profiles for nonnegligible rotation motion.

scatterer with coordinates (30, 10) m at the reference time. The ISAR profiles obtained if the effects of the rotational motion have been or have not been taken into account in processing the data are shown in Figure 8. Specifically, red and black plots are the results obtained by focusing the data received when no compensation for the rotation motion has been applied. As we can observe, the rotation has not affected the single-scan imaging result, red plot, whereas a degradation of the quality of the profile (such as wrong position of the peak, higher sidelobes level, and loss in resolution) is experienced for the multiscan case, black plot. By performing a correct image alignment and phase junction steps, successive scan images can be properly combined, and a correct imaging result is obtained, green plot.

Finally, we consider a ship target composed by many pointlike scatterers with different levels of superstructure located at a distance  $R_0 = 10$  km and moving with velocity  $|\vec{V}| = 7$  m/s and heading angle  $\theta_h = -45^\circ$ . By following the focusing technique described in Figure 5,  $M$  single-scan ISAR images of the ships are obtained and then combined to obtain a final multiscan image providing enhanced cross-range resolution. Figure 9 shows the images resulting from the integration of  $M = 1, 3, 5$  scans. As we can observe, while the range resolution is limited to be about 6.8 m by the bandwidth of the chirp signal transmitted by the coastal radar, the cross-range resolution of the image increases considering more scans. The single-scan image is shown in Figure 9(a) and we can observe that the poor azimuth resolution (about 10 m) does not allow a proper identification of the main features of the target, such as its size. By considering  $M = 3$ , Figure 9(b), and  $M = 5$  scans, Figure 9(c), we move from 10 m to 3.3 m and to 2 m, respectively. As the azimuth resolution increases, scattering centers not resolvable with the data received during a single scan can be resolved, thus providing enhanced capability to recognize the size of the ship and its main features. For

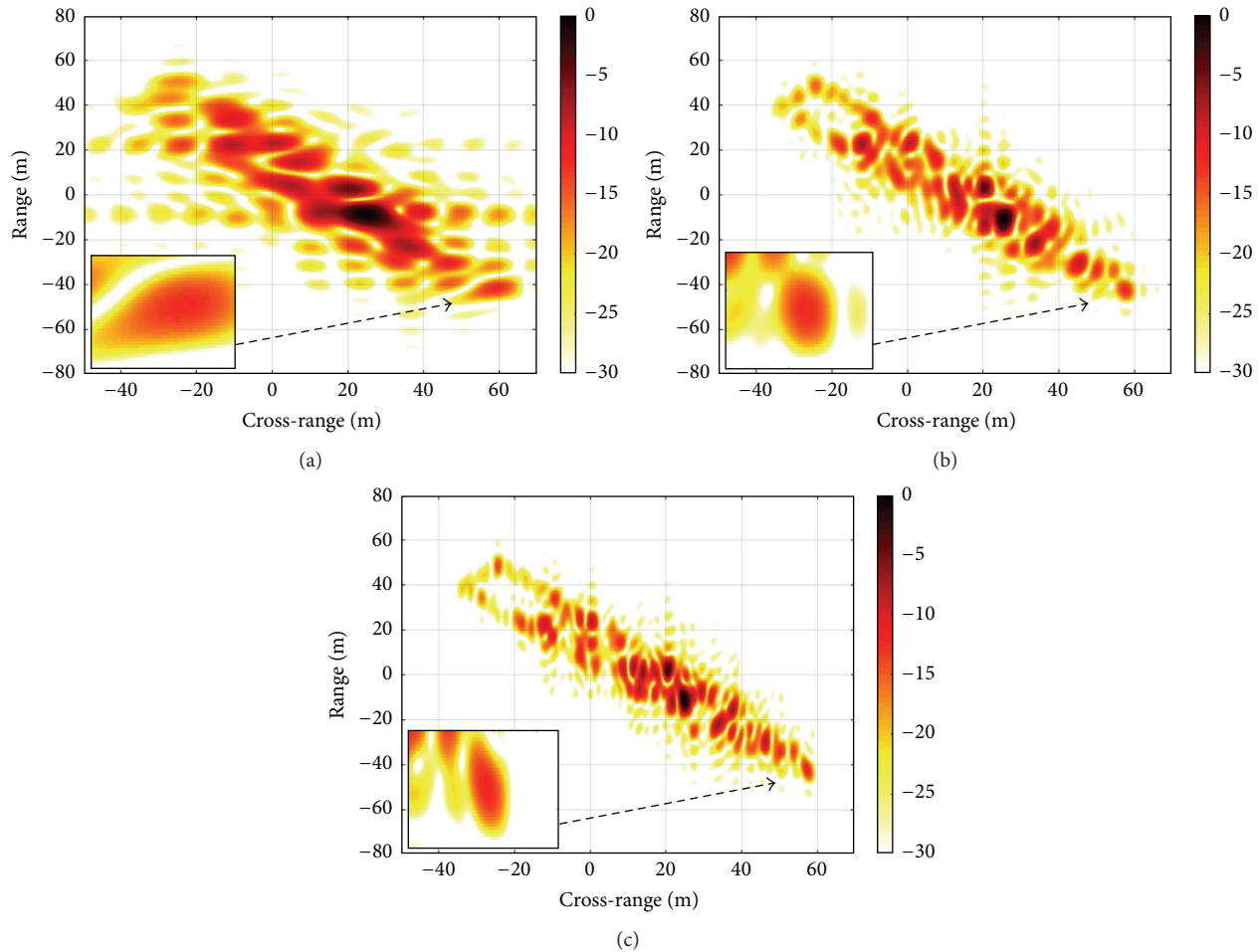


FIGURE 9: Single/multiscan ISAR images of the ship target.

example, black bottom boxes of Figure 9 highlight the patches of the images corresponding to the bow scatterer, whose position becomes progressively easier to be identified.

## 6. Conclusions

The paper puts forward a novel ISAR imaging system for coastal surveillance based on a parasitic array receiver and an opportunistic coastal radar. The signal transmitted by a ground-based radar with its antenna rotating for vessel traffic services purposes is exploited as signal of opportunity by an array of passive (receiving only) devices properly located near the coast. The physical aperture provided by such an array, jointly to the synthetic aperture provided by the target motion during successive scans of the radar, allows reaching a Doppler gradient suitable for the image resolution process. Relationships between the parameters of the array and the transmitter parameters have been derived to deal with ship targets of interest. Then, a focusing technique has been proposed able to focus the data collected over one or more scans, even in the case of not negligible rotation motion.

The simulated performance analysis proved the effectiveness of the technique to provide ISAR images of ship

targets with suitable resolutions. By exploiting multiple scans, azimuth resolution can be increased, thus achieving cross-range resolutions comparable or even better than the range resolutions, limited by the bandwidth of the transmitted signal. Furthermore, it should be pointed out that because of the exploitation of the translation motion, achievable ISAR images are top views of the ship. Such images can be properly exploited in ATR procedure, thus helping in increasing the efficiency of the vessel traffic monitoring and the coastal surveillance.

## Competing Interests

The authors declare that they do not have any conflict of interests.

## References

- [1] M. Glandrup, "Improving situation awareness in the maritime domain," in *Situation Awareness with System of Systems*, P. van de Laar, J. Tretmans, and M. Borth, Eds., pp. 21–38, Springer, New York, NY, USA, 2013.
- [2] D. Pastina, M. Sedhei, and D. Cristallini, "Geostationary satellite based passive bistatic ISAR for coastal surveillance," in

- Proceedings of the IEEE Radar Conference*, Washington, DC, USA, May 2010.
- [3] F. Turin and D. Pastina, "Multistatic passive ISAR based on geostationary satellites for coastal surveillance," in *Proceedings of the IEEE Radar Conference (RadarCon '13)*, Ottawa, Canada, May 2013.
- [4] D. W. O'Hagan, A. Capria, D. Petri et al., "Passive Bistatic Radar (PBR) for harbour protection applications," in *Proceedings of the IEEE Radar Conference*, pp. 0446–0450, IEEE, Atlanta, Ga, USA, May 2012.
- [5] D. Langellotti, F. Colone, P. Lombardo, M. Sedehi, and E. Tilli, "DVB-T based passive bistatic radar for maritime surveillance," in *Proceedings of the IEEE Radar Conference (RadarCon '14)*, pp. 1197–1202, IEEE, Cincinnati, Ohio, USA, May 2014.
- [6] K. Chetty, K. Woodbridge, H. Guo, and G. E. Smith, "Passive bistatic WiMAX radar for marine surveillance," in *Proceedings of the IEEE International Radar Conference*, pp. 188–193, Washington, DC, USA, May 2010.
- [7] H. Sun, D. K. P. Tan, Y. Lu, and M. Lesturgie, "Applications of passive surveillance radar system using cell phone base station illuminators," *IEEE Aerospace and Electronic Systems Magazine*, vol. 25, no. 3, pp. 10–18, 2010.
- [8] B. D. Steinberg and H. M. Subbaram, *Microwave Imaging Techniques*, Wiley, New York, NY, USA, 1991.
- [9] D. R. Wehner, *High-Resolution Radar*, Artech House, Boston, Mass, USA, 2nd edition, 1992.
- [10] S. Musman, D. Kerr, and C. Bachmann, "Automatic recognition of ISAR ship images," *IEEE Transactions on Aerospace and Electronic Systems*, vol. 32, no. 4, pp. 1392–1404, 1996.
- [11] F. Santi, D. Pastina, and P. Lombardo, "ISAR while-scan mode for coastal surveillance," in *Proceedings of the IEEE Radar Conference (RadarCon '14)*, pp. 1301–1306, Cincinnati, Ohio, USA, May 2014.
- [12] B. Correll, "Efficient spotlight SAR MIMO linear collection configurations," *IEEE Journal of Selected Topics in Signal Processing*, vol. 4, no. 1, pp. 33–39, 2010.
- [13] D. Pastina, M. Bucciarelli, and P. Lombardo, "Multistatic and MIMO distributed ISAR for enhanced cross-range resolution of rotating targets," *IEEE Transactions on Geoscience and Remote Sensing*, vol. 48, no. 8, pp. 3300–3317, 2010.
- [14] D. Pastina, F. Santi, and M. Bucciarelli, "MIMO distributed imaging of rotating targets for improved 2-D resolution," *IEEE Geoscience and Remote Sensing Letters*, vol. 12, no. 1, pp. 190–194, 2015.
- [15] G. Hajduch, R. Garello, J.-M. Le Caillec, M. Chabah, and J.-M. Quellec, "High-resolution snapshot SAR/ISAR imaging of ship targets at sea," in *SAR Image Analysis, Modeling, and Techniques V*, 39, vol. 4883 of *Proceedings of SPIE*, March 2003.
- [16] F. Berizzi and G. Corsini, "Autofocusing of inverse synthetic aperture radar images using contrast optimization," *IEEE Transactions on Aerospace and Electronic Systems*, vol. 32, no. 3, pp. 1185–1191, 1996.
- [17] L. Xi, L. Guosui, and J. Ni, "Autofocusing of ISAR images based on entropy minimization," *IEEE Transactions on Aerospace and Electronic Systems*, vol. 35, no. 4, pp. 1240–1252, 1999.
- [18] D. Pastina, "Rotation motion estimation for high resolution ISAR and hybrid SAR/ISAR target imaging," in *Proceedings of the IEEE Radar Conference (RADAR '08)*, pp. 1–6, IEEE, Rome, Italy, May 2008.
- [19] D. Pastina and C. Spina, "Slope-based frame selection and scaling technique for ship ISAR imaging," *IET Signal Processing*, vol. 2, no. 3, pp. 265–276, 2008.
- [20] F. Amato, M. Fiorini, S. Gallone, and G. Golino, "Fully solid state radar for vessel traffic services," in *Proceedings of the 11th International Radar Symposium (IRS '10)*, pp. 438–441, June 2010.

## Research Article

# Robust Adaptive Beamforming Using a Low-Complexity Steering Vector Estimation and Covariance Matrix Reconstruction Algorithm

Pei Chen, Yongjun Zhao, and Chengcheng Liu

Zhengzhou Institute of Information Science and Technology, Zhengzhou, Henan 450000, China

Correspondence should be addressed to Pei Chen; [clevercpei@126.com](mailto:clevercpei@126.com)

Received 16 April 2016; Accepted 12 June 2016

Academic Editor: Michelangelo Villano

Copyright © 2016 Pei Chen et al. This is an open access article distributed under the Creative Commons Attribution License, which permits unrestricted use, distribution, and reproduction in any medium, provided the original work is properly cited.

A novel low-complexity robust adaptive beamforming (RAB) technique is proposed in order to overcome the major drawbacks from which the recent reported RAB algorithms suffer, mainly the high computational cost and the requirement for optimization programs. The proposed algorithm estimates the array steering vector (ASV) using a closed-form formula obtained by a subspace-based method and reconstructs the interference-plus-noise (IPN) covariance matrix by utilizing a sampling progress and employing the covariance matrix taper (CMT) technique. Moreover, the proposed beamformer only requires knowledge of the antenna array geometry and prior information of the probable angular sector in which the actual ASV lies. Simulation results demonstrate the effectiveness and robustness of the proposed algorithm and prove that this algorithm can achieve superior performance over the existing RAB methods.

## 1. Introduction

Aiming at receiving a signal from a certain direction and suppressing interferences and noise, adaptive beamforming has found widespread application in many fields ranging from radar, sonar, wireless communication, and radio astronomy to medical imaging, speech processing, and so forth [1–4]. Beamformers can be regarded as spatial filters, which have proper performance under ideal circumstances. The standard Capon beamformer (SCB) is an optimal spatial filter that maximizes the array output signal-to-interference-plus-noise ratio (SINR) [5]. However, it is sensitive to array steering vector (ASV) uncertainty and direction of arrival (DOA) estimation error for the desired signal (DS). The performance also degrades due to the presence of the DS component in the training data and small sample size. In order to improve the robustness of SCB, various robust adaptive beamforming (RAB) techniques have been proposed in the past decades [6].

The existing RAB techniques mainly consist of diagonal loading (DL) technique [7], eigenspace-based (ESB) technique [8], uncertainty set-based technique [9, 10], and the reconstruction-based technique [11]. They have effective

performance in the presence of different mismatches in typical situations. However, there exist some drawbacks that limit their application range, which include the difficulty to choose the optimal DL factor, the high probability of subspace swap for ESB beamformers at low signal-to-noise ratio (SNR), the cost of reducing output SINR due to the expansion of the uncertainty set when the SV mismatch is large, the ad hoc nature, and the high computational cost.

Recently, a new approach to the design of RAB based on the interference-plus-noise (IPN) covariance matrix reconstruction has been introduced in [11]. This method utilizes the Capon spectrum to integrate over an angular sector separated from the direction of DS. The reconstruction-based beamformer is effective at removing the DS from the sample covariance matrix but suffers from its high computational complexity. The main computational cost is due to the large number of samples involved in both spectrum estimation and summation. On the other hand, the recent beamformers in [12, 13] enhance the robustness against ASV errors. However, the utilization of complicated optimization software restricts their applications in practical situations. To improve the reconstruction-based RAB

technique, a Low-Complexity Shrinkage-Based Mismatch Estimation (LOSCME) algorithm is presented in [14]. But it can perform effectively only when the interfering sources are weak.

To reduce the computational complexity of the RAB method in [11] and eliminate its dependence on the optimization software, in this paper, a novel reconstruction-based RAB algorithm is proposed. This algorithm is characterized by lower complexity and a closed-form formula estimation of the actual ASV. Moreover, it requires very little prior information and has a superior performance to previously reported RAB algorithms. The only prior information required is the knowledge of the antenna array geometry and the coarse angular sector in which the actual ASV lies. Three steps are needed to achieve this algorithm. Firstly, a subspace-based method is introduced to obtain a closed-form formula for ASV estimation, avoiding using the optimization software. Then, the IPN covariance matrix is reconstructed based on a spatial power spectrum sampling (SPSS) method [15], which is realized by a proposed sample equation. Finally, the covariance matrix taper (CMT) technique [16] is utilized to adopt the relatively small size of array systems in practice. Simulation results will be provided to prove the effectiveness and robustness of the proposed beamformer.

The rest of this paper is organized as follows. The data model of array output and some necessary backgrounds about adaptive beamformer are described in Section 2. In Section 3, a novel RAB algorithm is proposed by employing ASV estimation and IPN covariance matrix reconstruction. Simulation results are presented in Section 4. Finally, conclusion is drawn in Section 5.

## 2. Signal Model

Consider a uniform linear array (ULA) of  $M$  omnidirectional antenna elements impinged by  $P$  narrowband uncorrelated far-field signals. The  $M \times 1$  vector representing the received signal at the  $k$ th snapshot can be modeled as

$$\mathbf{x}(k) = \mathbf{s}(k) + \mathbf{i}(k) + \mathbf{n}(k), \quad (1)$$

where  $\mathbf{s}(k)$ ,  $\mathbf{i}(k)$ , and  $\mathbf{n}(k)$  denote the statistically independent  $M \times 1$  vectors of the DS, interference, and noise, respectively. The beamformer output is given by  $\mathbf{y}(k) = \mathbf{w}^H \mathbf{x}(k)$ , where  $\mathbf{w} = [w_1, w_2, \dots, w_M]^T$  is the complex beamformer weighting vector, and  $(\cdot)^H$  and  $(\cdot)^T$  denote the Hermitian transpose and transpose, respectively. The beamformer output SINR is defined as

$$\text{SINR} = \frac{\sigma_s^2 |\mathbf{w}^H \mathbf{a}(\theta_s)|^2}{\mathbf{w}^H \mathbf{R}_{\mathbf{i}+\mathbf{n}} \mathbf{w}}, \quad (2)$$

where  $\theta_s$  is the assumed DOA of the DS and  $\mathbf{a}(\theta_s)$  is the ASV, which has the general form  $\mathbf{a}(\theta_s) = [1 e^{j\pi \sin \theta_s} \dots e^{j\pi(M-1) \sin \theta_s}]^T$ . Meanwhile,  $\sigma_s^2$  is the power of the DS, and  $\mathbf{R}_{\mathbf{i}+\mathbf{n}} = E\{(\mathbf{i}(k) + \mathbf{n}(k))(\mathbf{i}(k) + \mathbf{n}(k))^H\}$  is the IPN covariance matrix.

By maximizing the output SINR of the beamformer, the optimal weight vector can be obtained by

$$\begin{aligned} \min_{\mathbf{w}} \quad & \mathbf{w}^H \mathbf{R}_{\mathbf{i}+\mathbf{n}} \mathbf{w} \\ \text{subject to} \quad & \mathbf{w}^H \mathbf{a}(\theta_s) = 1. \end{aligned} \quad (3)$$

The solution is known as the Capon beamformer [13]:

$$\mathbf{w} = \frac{\mathbf{R}_{\mathbf{i}+\mathbf{n}}^{-1} \mathbf{a}(\theta_s)}{\mathbf{a}^H(\theta_s) \mathbf{R}_{\mathbf{i}+\mathbf{n}}^{-1} \mathbf{a}(\theta_s)}. \quad (4)$$

In practice, theoretical covariance matrix  $\mathbf{R}_{\mathbf{i}+\mathbf{n}}$  is usually unavailable and sample covariance matrix (5) is used as an approximation:

$$\hat{\mathbf{R}}_x = \frac{1}{K} \sum_{k=1}^K \mathbf{x}(k) \mathbf{x}^H(k), \quad (5)$$

where  $K$  is the number of data snapshots.

## 3. Proposed Approach

The performance of standard beamformers degrades dramatically when the ASV errors exist and the DS with a high SNR is present in the training snapshots. To remove the DS from the sample covariance matrix, recently, an IPN covariance matrix reconstruction method was proposed [11].

In [11], the IPN covariance matrix can be reconstructed by using the spatial spectrum of the array as

$$\mathbf{R}_{\mathbf{i}+\mathbf{n}} = \int_{\theta \in \bar{\Theta}} \sigma^2(\theta) \mathbf{a}(\theta) \mathbf{a}^H(\theta) d\theta, \quad (6)$$

where  $\sigma^2(\theta)$  is the Capon spectrum  $\sigma^2(\theta) = 1/\mathbf{a}^H(\theta) \hat{\mathbf{R}}_x^{-1} \mathbf{a}(\theta)$ ,  $\bar{\Theta}$  is the complement sector of  $\Theta$  and  $\Theta$  stands for the assumed direction range of the DS; that is,  $\bar{\Theta} \cap \Theta = \emptyset$ , and  $\bar{\Theta} \cup \Theta$  covers whole spatial domain.

This method has mainly two aspects of drawbacks. Firstly, concerning the mismatch between the actual ASV and the nominal ASV, the IPN matrix may not be reconstructed accurately. Secondly, its high computational complexity restricts its practical performance [12]. In the following part, more precise estimation of the actual ASV can be achieved and the computational cost of IPN matrix reconstruction can be reduced.

*3.1. Desired Signal Array Steering Vector Estimation.* Similar to the reconstruction of IPN covariance matrix as (6), a new matrix  $\mathbf{C}_{\text{asv}}$  can be constructed by

$$\mathbf{C}_{\text{asv}} = \int_{\Theta} c(\theta) \mathbf{a}(\theta) \mathbf{a}^H(\theta) d\theta, \quad (7)$$

where  $c(\theta)$  denotes a probability density function, but the choice of  $c(\theta)$  is more flexible, which means that  $c(\theta)$  can be chosen to be independent of  $\theta$ , for example,  $c(\theta) = 1, \forall \theta \in$

$\Theta$ , or adjust values depending on the prior information. Then,  $\mathbf{C}_{\text{asv}}$  can be eigendecomposed as

$$\mathbf{C}_{\text{asv}} = \sum_{i=1}^M \sigma_i \mathbf{v}_i \mathbf{v}_i^H = \mathbf{V} \mathbf{\Sigma} \mathbf{V}^H, \quad (8)$$

where  $\{\sigma_i, i = 1, \dots, M\}$  are the eigenvalues of  $\mathbf{C}_{\text{asv}}$  in descending order,  $\mathbf{\Sigma} = \text{diag}\{\sigma_1, \dots, \sigma_M\}$  are diagonal matrices,  $\{\mathbf{v}_i, i = 1, \dots, M\}$  are the eigenvectors associated with  $\sigma_i$ , and  $\mathbf{V} = [\mathbf{v}_1, \dots, \mathbf{v}_M]$ . Following the approach in [17], let  $S$  be the smallest integer such that  $\sum_{i=1}^S |\sigma_i|^2 / \sum_{i=1}^M |\sigma_i|^2 > \xi$ , where  $0 < \xi < 1$  is a predetermined threshold. Then, the eigenvectors associated with  $S$  largest eigenvalues of  $\mathbf{C}_{\text{asv}}$  can be chosen to form the column orthogonal matrix  $\mathbf{V}_S = [\mathbf{v}_1, \dots, \mathbf{v}_S]$ . As derivation in [18], the actual ASV  $\mathbf{a}(\theta_s)$  lies in the subspace spanned by the columns of  $\mathbf{V}_S$ .

Similar to (8), in order to obtain the eigenvector, the sample covariance matrix  $\hat{\mathbf{R}}_x$  can be decomposed as

$$\hat{\mathbf{R}}_x = \sum_{j=1}^M \lambda_j \mathbf{e}_j \mathbf{e}_j^H = \mathbf{E}_s \mathbf{\Lambda}_s \mathbf{E}_s^H + \mathbf{E}_n \mathbf{\Lambda}_n \mathbf{E}_n^H, \quad (9)$$

where  $\{\lambda_j, j = 1, \dots, M\}$  are the eigenvalues of  $\hat{\mathbf{R}}_x$  in descending order,  $\mathbf{\Lambda}_s = \text{diag}\{\lambda_1, \dots, \lambda_p\}$  and  $\mathbf{\Lambda}_n = \text{diag}\{\lambda_{p+1}, \dots, \lambda_M\}$  are diagonal matrices,  $\{\mathbf{e}_j, j = 1, \dots, M\}$  are the eigenvectors associated with  $\lambda_j$ , and  $\mathbf{E}_s = [\mathbf{e}_1, \mathbf{e}_2, \dots, \mathbf{e}_p]$  and  $\mathbf{E}_n = [\mathbf{e}_{p+1}, \dots, \mathbf{e}_M]$  denote the signal-plus-interference (SPI) subspace and noise subspace, respectively. It is well known that the actual ASV of DS  $\mathbf{a}(\theta_s)$  belongs to the subspace spanned by the columns of  $\mathbf{E}_s$  [19].

As mentioned above, two constraints can be imposed on  $\mathbf{a}$ :

$$\begin{aligned} C_1 &= \{\mathbf{a} : \mathbf{a} = \mathbf{V}_S \alpha_V\}, \\ C_2 &= \{\mathbf{a} : \mathbf{a} = \mathbf{E}_s \alpha_E\}, \end{aligned} \quad (10)$$

where  $\alpha_V$  and  $\alpha_E$  are the coefficient vectors. Then, the actual ASV should be a vector lying within the intersection of  $C_0 = C_1 \cap C_2$ . This intersection can be obtained by employing the theorem of sequential vector space projections [19], and the ASV of DS is proved to be estimated by

$$\mathbf{a}_{\text{es}} = \sqrt{MP} \{\mathbf{P}_{C_1} \mathbf{P}_{C_2}\}, \quad (11)$$

where  $\mathbf{P}_{C_1} = \mathbf{V}_S \mathbf{V}_S^H$ ,  $\mathbf{P}_{C_2} = \mathbf{E}_s \mathbf{E}_s^H$ , and  $P\{\cdot\}$  denotes the eigenvector associated with the maximal eigenvalue of a matrix. This estimation method can be more efficient when the look direction error is large, and the method avoids the need of optimization software by using a closed-form formula.

**3.2. Spatial Power Spectrum Sampling Based IPN Covariance Matrix Reconstruction.** The main computational cost of the method in [11] is the integration approximation by summation, where  $S$  (the number of sampled values) times spectrum estimation and vector multiplication operations have to be performed. To reduce the cost, the complex spectrum estimation process should be eliminated.

Consider the inner product of two steering vector which is written as

$$f(\theta; \theta_0) = \frac{1}{M} \mathbf{a}^H(\theta_0) \mathbf{a}(\theta), \quad (12)$$

where  $\theta_0$  is a specified reference direction and  $\theta, \theta_0 \in [-\pi/2, \pi/2]$ . Substituting  $\mathbf{a}(\theta)$  into (12) gives

$$f(\theta; \theta_0) = \frac{1}{M} \sum_{k=0}^{M-1} e^{jk\pi[\sin(\theta) - \sin(\theta_0)]}. \quad (13)$$

Let  $x = M/2[\sin(\theta) - \sin(\theta_0)] \in [(-1 - \sin(\theta_0))M/2, (1 - \sin(\theta_0))M/2]$ ; (13) can be written as

$$\begin{aligned} f(x) &= \frac{1}{M} \sum_{k=0}^{M-1} e^{j(2\pi/M)kx} \\ &= \frac{1}{M} \cdot \frac{\sin(\pi x)}{\sin((\pi/M)x)} e^{j((M-1)/M)\pi x}. \end{aligned} \quad (14)$$

From the derivation above,  $f(x)$  can be regarded as an inverse discrete Fourier transform (IDFT) of an  $M$ -point rectangular function in the frequency domain. When  $M$  is large enough,  $f(x)$  can be approximated as a sinc function; that is,  $f(x) = \text{sinc}(\pi x) = \sin(\pi x)/\pi x$ ;  $f(\theta; \theta_0)$  will approximate a Kronecker delta function; that is,

$$f(\theta; \theta_0) \approx \delta_{\theta, \theta_0} = \begin{cases} 1, & \theta = \theta_0 \\ 0, & \text{else.} \end{cases} \quad (15)$$

The function  $f(\theta; \theta_0)$  is called the selecting property of the steering vector in [15].

Denote the zeros of  $f(\theta; \theta_0)$  by  $\theta_k$ , and consider (14);  $f(x) = 0$  is obtained when  $x \in Z = \{z \mid z \in [(-1 - \sin(\theta_0))M/2, (1 - \sin(\theta_0))M/2], z \in \mathbb{Z}, z \neq 0\}$ ; then there are  $M-1$  such values in the set  $Z$  denoted by  $x_k, k = 1, 2, \dots, M-1$ . Then  $\theta_k$  can be easily obtained by  $\theta_k = \arcsin(2x_k/M + \sin(\theta_0))$ .

Define a matrix using  $\{\theta_k\}_{k=0}^{M-1}$ :

$$\mathbf{D} = \frac{1}{M} \sum_{\theta_k \in \Omega} \mathbf{a}(\theta_k) \mathbf{a}^H(\theta_k), \quad (16)$$

where  $\Omega$  is a specified angular sector. Consider that  $\mathbf{R}$  can be formed by integrating the spatial spectrum  $\sigma^2(\theta)$  though the whole region as

$$\mathbf{R} = \int_{\theta \in [-\pi/2, \pi/2]} \sigma^2(\theta) \mathbf{a}(\theta) \mathbf{a}^H(\theta) d\theta. \quad (17)$$

Then, let  $\Omega = \bar{\Theta}$ ; (18) can be obtained as

$$\begin{aligned}
\mathbf{D} \cdot \mathbf{R} \cdot \mathbf{D} &= \frac{1}{M} \sum_{\theta_k \in \bar{\Theta}} \mathbf{a}(\theta_k) \mathbf{a}^H(\theta_k) \\
&\cdot \left( \int_{\theta \in [-\pi/2, \pi/2]} \sigma^2(\theta) \mathbf{a}(\theta) \mathbf{a}^H(\theta) d\theta \right) \cdot \frac{1}{M} \\
&\cdot \sum_{\theta_i \in \bar{\Theta}} \mathbf{a}(\theta_i) \mathbf{a}^H(\theta_i) = \sum_{\theta_k \in \bar{\Theta}} \sum_{\theta_i \in \bar{\Theta}} \mathbf{a}(\theta_i) \\
&\cdot \left\{ \int_{\theta \in [-\pi/2, \pi/2]} \sigma^2(\theta) \left[ \frac{1}{M} \mathbf{a}^H(\theta_i) \mathbf{a}(\theta) \right] \cdot \left[ \frac{1}{M} \right. \right. \\
&\cdot \left. \left. \mathbf{a}^H(\theta) \mathbf{a}(\theta_k) \right] d\theta \right\} \cdot \mathbf{a}^H(\theta_k) = \sum_{\theta_k \in \bar{\Theta}} \sum_{\theta_i \in \bar{\Theta}} \mathbf{a}(\theta_i) \\
&\cdot \left\{ \int_{\theta \in [-\pi/2, \pi/2]} \sigma^2(\theta) f(\theta; \theta_i) f(\theta_k; \theta) d\theta \right\} \mathbf{a}^H(\theta_k).
\end{aligned} \tag{18}$$

As discussed above, when  $M$  is large enough,  $\mathbf{D} \cdot \mathbf{R} \cdot \mathbf{D}$  is a Hermitian matrix and can be approximated as

$$\begin{aligned}
\mathbf{D} \cdot \mathbf{R} \cdot \mathbf{D} &\approx \sum_{\theta_k \in \bar{\Theta}} \sum_{\theta_i \in \bar{\Theta}} \mathbf{a}(\theta_i) \left\{ \int_{\theta \in [-\pi/2, \pi/2]} \delta_{\theta, \theta_i} \delta_{\theta_k, \theta} d\theta \right\} \mathbf{a}^H(\theta_k) \\
&= \sum_{\theta_k \in \bar{\Theta}} \sigma^2(\theta_k) \mathbf{a}(\theta_k) \mathbf{a}^H(\theta_k).
\end{aligned} \tag{19}$$

In this way, the IPN covariance matrix is estimated by the sample matrix  $\mathbf{D}$  without calculating the spatial power spectrum. In practice,  $\mathbf{R}$  can be replaced by  $\hat{\mathbf{R}}_x$ , which yields  $\hat{\mathbf{R}}_{i+n} \approx \mathbf{D} \cdot \hat{\mathbf{R}}_x \cdot \mathbf{D}$ .

However, when  $M \ll \infty$ , there will be a large estimation error, because the sampling spacing is not dense enough. For the purpose of improving the performance, the covariance matrix tapering technique introduced in [16] is employed. The tapered matrix is given by  $\mathbf{R}_T = \mathbf{R} \circ \mathbf{T}$ , where “ $\circ$ ” denotes the Hadamard product and  $\mathbf{T}$  is the taper matrix. Here, the Mailloux-Zatman (MZ) taper is used, which is defined as

$$\mathbf{T}_{MZ} = [a_{mm}]_{M \times M} = \left[ \text{sinc} \left( \frac{(m-n)\Delta}{\pi} \right) \right], \quad \Delta > 0, \tag{20}$$

where  $\Delta$  corresponds to the width of the dithering area. Hence,  $\mathbf{T}_{MZ}$  should be adopted to taper the sample covariance matrix  $\hat{\mathbf{R}}_x$  and estimated IPN covariance matrix, respectively; that is, the reconstruction of IPN covariance matrix can be obtained by

$$\hat{\mathbf{R}}_{i+n} = \left( \mathbf{D} \cdot \left( \hat{\mathbf{R}}_x \circ \mathbf{T}_{MZ} \right) \cdot \mathbf{D} \right) \circ \mathbf{T}_{MZ}. \tag{21}$$

**3.3. The Proposed Beamforming Algorithm.** Based on the discussions above, the proposed beamforming algorithm can be summarized by the following steps.

*Step 1.* Construct the two subspaces  $\mathbf{V}_s$  and  $\mathbf{E}_s$  by eigendecomposing  $\mathbf{C}_{asv}$  and  $\hat{\mathbf{R}}_x$ , respectively. Then estimate the ASV of DS  $\mathbf{a}_{es}$  using (11).

*Step 2.* Specify the MZ taper  $\mathbf{T}_{MZ}$  using (20), and construct  $\mathbf{D}$  by (16). Hence, the reconstruction of IPN covariance matrix can be obtained by using (21).

*Step 3.* Substituting the reconstructed IPN covariance matrix  $\hat{\mathbf{R}}_{i+n}$  and estimated ASV of DS  $\mathbf{a}_{es}$  into the Capon beamformer, the weight vector of the proposed approach is computed as

$$\mathbf{w} = \frac{\hat{\mathbf{R}}_{i+n}^{-1} \mathbf{a}_{es}(\theta_s)}{\mathbf{a}_{es}^H(\theta_s) \hat{\mathbf{R}}_{i+n}^{-1} \mathbf{a}_{es}(\theta_s)}. \tag{22}$$

In the proposed algorithm, the main computational complexity lies in the eigendecomposition operation and the matrix inversion operation, both of which have complexity of  $O(M^3)$ . That means the overall computational complexity is  $O(M^3)$ . Considering that the number of sampling points required in (7) and (16) is reasonably much less than that required in the beamformer in [11], the proposed beamformer has a lower cost than that of [11]. Additionally, compared to the existing RAB methods in [12, 13], which have complexity equal or higher than  $O(M^{3.5})$ , the proposed algorithm also avoids the need of optimization software and, thus, is easier to apply in practice.

## 4. Simulations

In the simulations, without loss of generality, a ULA with  $M = 30$  omnidirectional sensors is considered. It is assumed that there is one DS from the presumed direction  $\theta_s = 5^\circ$ . Two uncorrelated interferences with random waveforms arrive from DOA angles of  $-53^\circ$  and  $32^\circ$ , respectively. The noise is modeled as zero-mean and unity variance spatially and temporally white Gaussian noise. The interference-to-noise ratio (INR) at each sensor is set to be fixed at 30 dB. For each scenario, 500 Monte Carlo trials are performed.

The proposed beamformer is compared to the diagonal loading sample matrix inversion (LSMI) beamformer [20], the ESB beamformer [8], the worst-case-based beamformer [9], the sequential quadratic programming (SQP) based beamformer [18], the reconstruction-based beamformer [11], and the beamformer in [13]. The diagonal loading factor of the LSMI beamformer is chosen as twice the noise power. The dimension of the signal-plus-interference subspace is assumed to be always estimated correctly for the eigenspace-based beamformer. The value  $\varepsilon = 0.3M$  is selected for the worst-case-based beamformer as it has been recommended in [9], while the value  $\delta = 0.1$  and 20 dominant eigenvectors of the matrix  $\mathbf{C}$  are used in the SQP based beamformer. For the proposed beamformer, the reconstruction-based beamformer, and the beamformer in [13], the angular sector of the DS is presumed to be  $\Theta = [\theta_p - 5^\circ, \theta_p + 5^\circ]$ . In this paper,  $\xi = 0.95$ ,  $\theta_0 = 0^\circ$ , and  $\Delta = 2 \arcsin(2/M)$  are chosen in (11), (12), and (20), respectively.

*Example 1* (mismatch due to signal direction error). The look direction mismatch of the DS is assumed to be random and uniformly distributed in  $[-4^\circ, 4^\circ]$  for each simulation run,

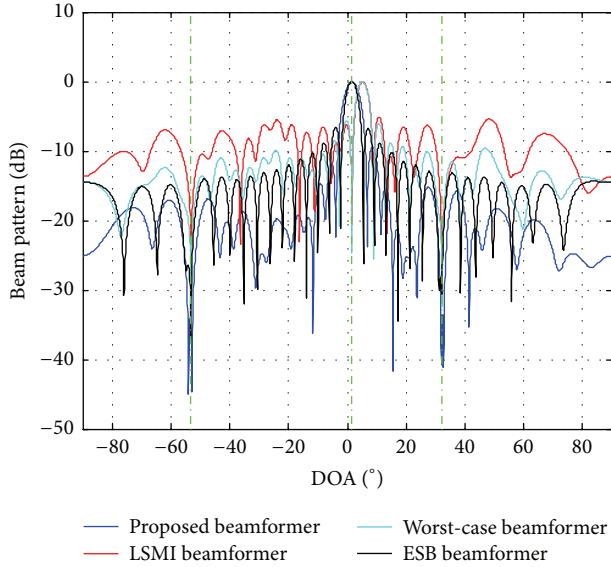


FIGURE 1: Comparison of the normalized beam patterns in Example 1 with SNR = 0 dB and  $K = 60$ .

which means the mismatch changes from run to run but keeps fixed from snapshot to snapshot. The array normalized beam patterns for the beamformers in a single simulation run where SNR = 0 dB and  $K = 60$  are displayed in Figure 1. It can be seen that, in the presence of pointing error, the proposed beamformer and ESB beamformer are able to point the main lobe to the actual direction, while the LSMI beamformer and worst-case-based beamformer cannot. Furthermore, the proposed beamformer has lower side lobes and deeper nulls at the directions of interferences, which make the proposed beamformer suppress the noise and interferences effectively.

Considering the influence of random look direction error on array output SINR, the performance curves versus the input SNR and the number of snapshots are drawn in Figures 2(a) and 2(b), respectively. The number of snapshots is fixed to be  $K = 60$  and the INR is kept at 30 dB in Figure 2(a), while a fixed SNR for the DS at 10 dB and a fixed INR at 30 dB are considered in Figure 2(b). From the results shown in Figure 2, it can be found that the output SINR of the proposed algorithm is closer to the optimal SINR in a large range of SNR from  $-10$  to 50 dB and for all values of number of snapshots from 10 to 100, which illustrates its high dynamic range. That means the proposed algorithm outperforms the other tested beamformers in the scenario where only signal direction error exists.

The SINR performance versus the pointing error is also investigated, and the results are shown in Figure 3 with fixed SNR and INR at 10 dB and 30 dB, respectively. It can be seen that the proposed beamformer effectively deals with a wide range of pointing errors and achieves the best performance among the tested beamformers even when the pointing error is as large as  $\pm 4^\circ$ .

TABLE 1: Deviations from the optimal SINR for training data size of  $K = 60$  and INR = 30 dB.

Beamformers	Deviations (dB) at SNR = 0 dB	Deviations (dB) at SNR = 30 dB
Proposed	1.330	1.347
LSMI	12.277	57.511
Worst-case-based	3.139	21.768
ESB	2.949	45.948
SQP	3.755	43.308
Reconstruction-based	1.081	1.083
Beamformer in [13]	3.122	39.040

*Example 2* (mismatch due to ASV random error). In this simulation example, the ASV of DS is assumed to be randomly distributed in an uncertainty set, which can be modeled as

$$\mathbf{a}(\theta_s) = \bar{\mathbf{a}}(\theta_s) + \mathbf{e}, \quad (23)$$

where  $\bar{\mathbf{a}}(\theta_s)$  represents the nominal SV corresponding to the direction  $\theta_s$  and  $\mathbf{e}$  is the random error vector, which is drawn in each simulation run independently from an uncertainty set as follows [12]:

$$\mathbf{e} = \frac{\varepsilon}{\sqrt{M}} [e^{j\phi_0}, e^{j\phi_1}, \dots, e^{j\phi_{M-1}}], \quad (24)$$

where  $\varepsilon$  and  $\phi_m$  are uniformly distributed in the intervals  $[0, \sqrt{3}]$  and  $[0, 2\pi]$ , respectively. Figures 4(a) and 4(b) correspond to the performance of the investigated methods versus the input SNR and the number of snapshots. It can be seen from the figures that the proposed beamformer and the reconstruction-based beamformer outperform the other tested beamformers. Table 1 shows the deviations from the optimal SINR for the beamformers at SNR = 0 dB and SNR = 30 dB, respectively. The performance improvement is a direct result of the ASV estimation and DS elimination, especially at high SNR values.

Furthermore, the proposed algorithm performs almost as well as the reconstruction-based beamformer for the output SINR but enjoys a faster convergence rate because of the lower computational cost without complex integral computation. Since the ASV mismatch is comprehensive and arbitrary-type, the proposed beamformer is proved to be effective against the random error of ASV.

*Example 3* (mismatch due to incoherent local scattering). In this example, it is assumed that the desired signal has a time-varying ASV which can be modeled as [11]

$$\mathbf{a}(\theta_s; k) = u_0(k) \bar{\mathbf{a}}(\theta_s) + \sum_{p=1}^4 u_p'(k) \mathbf{a}'(\theta_p'), \quad (25)$$

where  $\mathbf{a}'(\theta_p')$ , without loss of generality,  $p = 1, 2, 3, 4$ , denotes the incoherently scattered signal paths. Assume that the

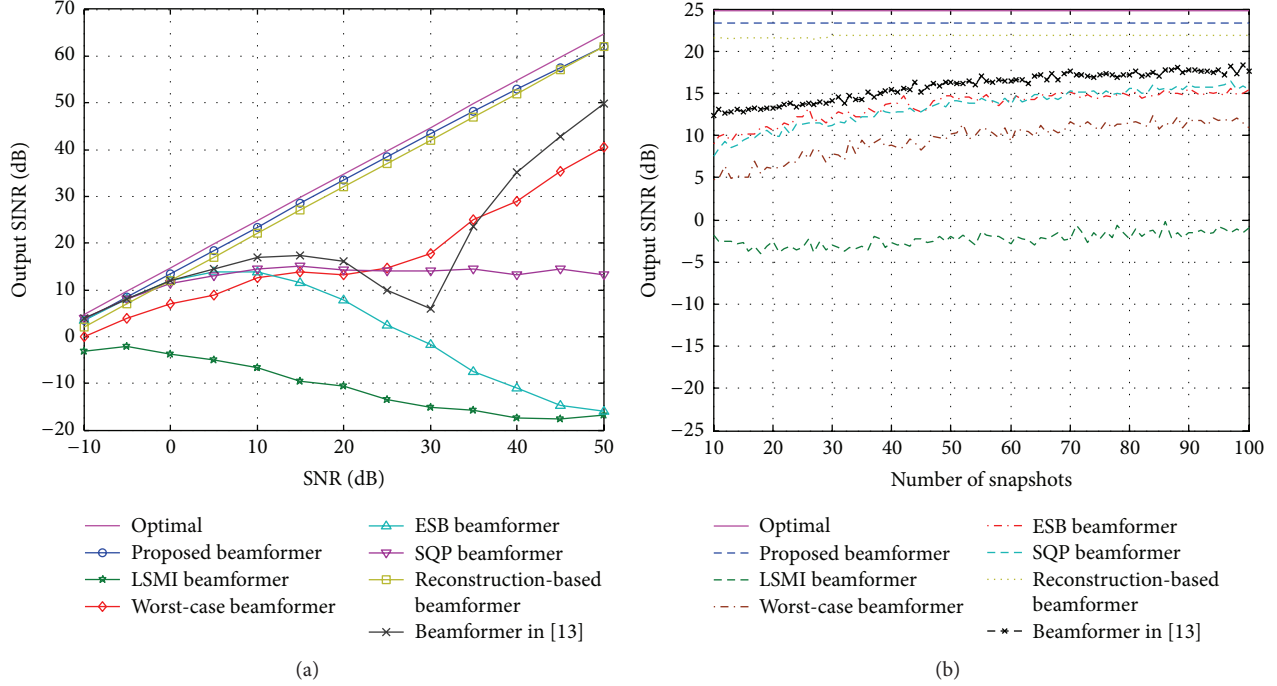


FIGURE 2: Performance of the beamformers for the case of mismatch due to signal direction error. (a) Output SINR versus SNR for training data size of  $K = 60$  and  $\text{INR} = 30$  dB. (b) Output SINR versus number of snapshots for fixed SNR = 10 dB and  $\text{INR} = 30$  dB.

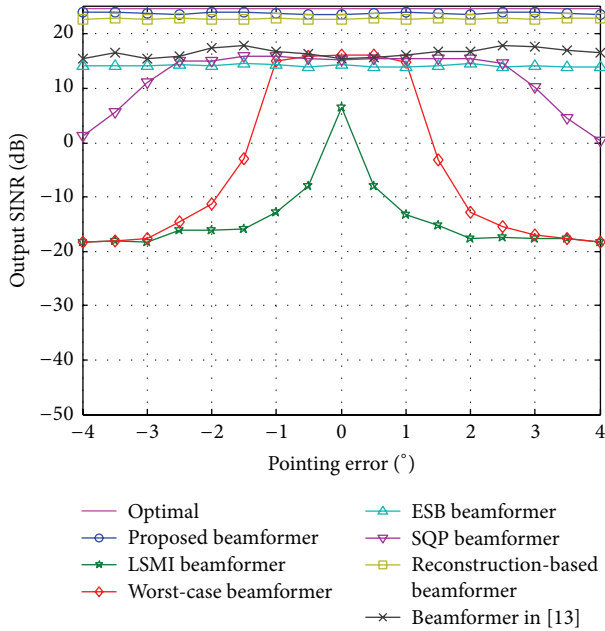


FIGURE 3: Output SINR versus pointing error for training data size of  $K = 60$  and SNR = 10 dB and  $\text{INR} = 30$  dB.

directions  $\theta'_p$  are randomly distributed in a Gaussian distribution with mean  $\theta_s$  and standard deviation  $2^\circ$ ;  $u_0(k)$  and  $u'_p(k)$  are independently and identically distributed complex Gaussian random variables drawn from  $N(0, 1)$  which change from snapshot to snapshot.

In this scenario, the signal covariance matrix  $\mathbf{R}_s$  is no longer a rank-one matrix; thus the output SINR should be rewritten in a more general form [9]:

$$\text{SINR}_{\text{opt}} = \frac{\mathbf{w}^H \mathbf{R}_s \mathbf{w}}{\mathbf{w}^H \mathbf{R}_{i+n} \mathbf{w}}, \quad (26)$$

which is maximized by [9]

$$\mathbf{w}_{\text{opt}} = P \left\{ \mathbf{R}_{i+n}^{-1} \mathbf{R}_s \right\}, \quad (27)$$

where  $P\{\cdot\}$  denotes the same operation as in (11). Figures 5(a) and 5(b) show the performance curves versus the input SNR and the number of snapshots. It can be seen from the figures that the proposed beamformer presents an effective performance when handling incoherent local scattering. Similar to Example 2, in detail, there is about 0.8 dB performance loss for the proposed algorithm comparing to the reconstruction-based beamformer. The main reason is that the DS may leak into the complement sector  $\bar{\Theta}$  due to the incoherent local scattering, which affects the accuracy of the ASV estimation.

*Example 4* (impacts of some factors on performance). The main purpose of this example is to study the impacts of some factors on performance.  $\xi$  and  $\Delta$  are two main factors in the proposed algorithm. The former affects the accuracy of the construction of subspace in which the actual ASV  $\mathbf{a}(\theta_s)$  lies, and the latter decides the choice of taper matrix which plays a key role in the reconstruction of IPN covariance matrix.

For the purpose of studying the impacts of the two factors, the model of the mismatch is set to be the same as the first example. The number of snapshots is fixed to be  $K = 50$ ;

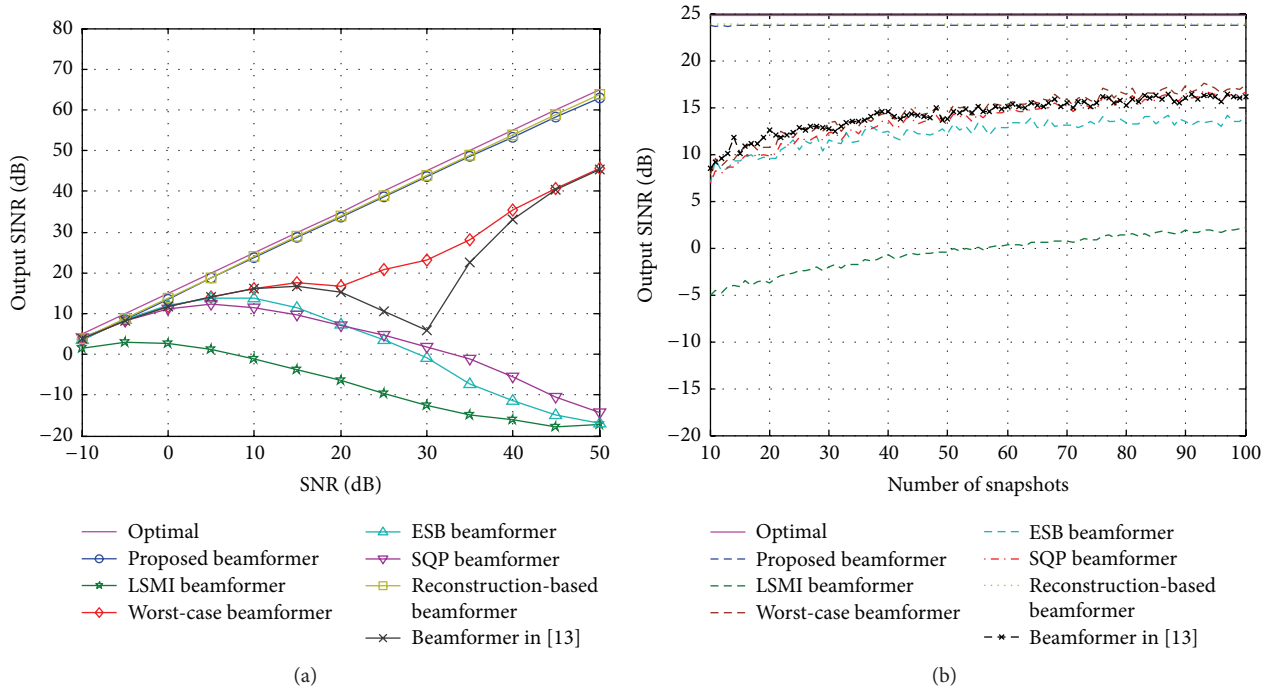


FIGURE 4: Performance of the beamformers for the case of ASV random error. (a) Output SINR versus SNR for training data size of  $K = 60$  and  $\text{INR} = 30$  dB. (b) Output SINR versus number of snapshots for fixed  $\text{SNR} = 10$  dB and  $\text{INR} = 30$  dB.

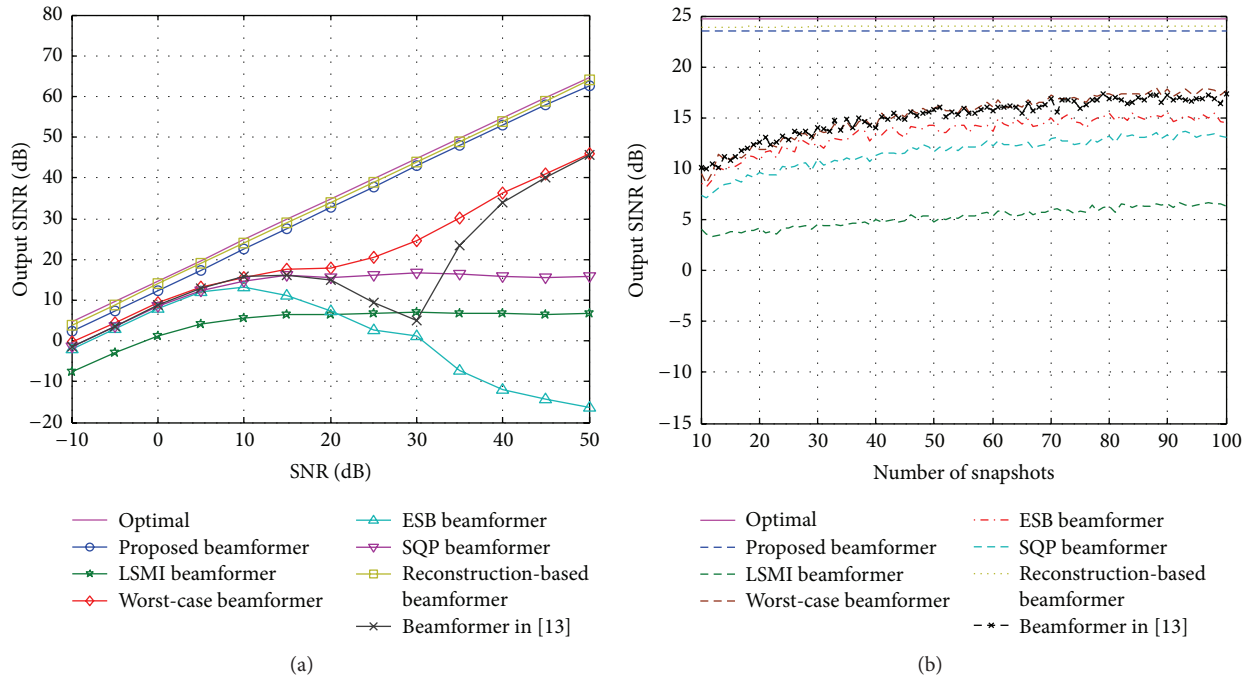


FIGURE 5: Performance of the beamformers for the case of incoherent local scattering. (a) Output SINR versus SNR for training data size of  $K = 60$  and  $\text{INR} = 30$  dB. (b) Output SINR versus number of snapshots for fixed  $\text{SNR} = 10$  dB and  $\text{INR} = 30$  dB.

the  $\text{INR}$  and  $\text{SNR}$  are kept at 20 dB and 10 dB, respectively. The performances of the proposed algorithm versus  $\xi$  and  $\Delta$  are displayed in Figures 6(a) and 6(b), respectively. From Figure 6(a), it can be seen that the output SINR increases as  $\xi$  gets larger, but the growth range is quite small. Considering

that the computational cost will not significantly increase as  $\xi$  gets larger, setting  $\xi = 0.95$  in the proposed algorithm is appropriate. Similarly, the result of the test of  $\Delta$  is shown in Figure 6(b), in which the choice of  $\Delta = 2 \arcsin(2/M)$  can be found near the peak of the performance curve. To ensure a

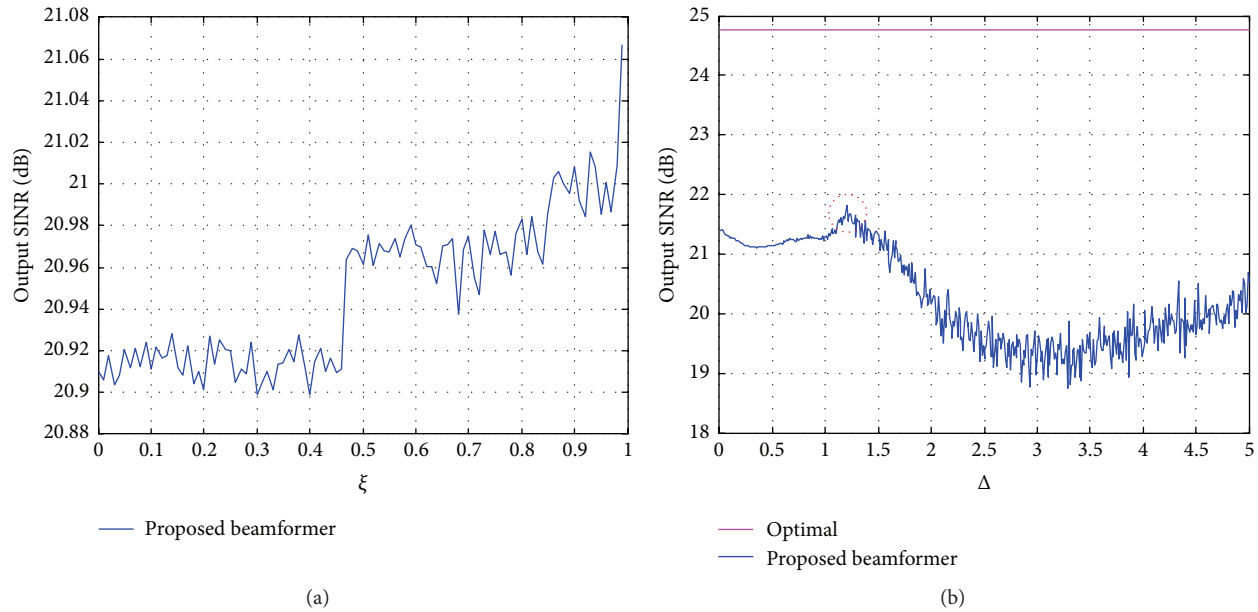


FIGURE 6: Performance of the beamformers for the case of mismatch due to signal direction error. (a) Output SINR versus  $\xi$ . (b) Output SINR versus  $\Delta$  for training data size of  $K = 50$  and  $\text{INR} = 20$  dB and  $\text{SNR} = 10$  dB.

satisfying output performance,  $\Delta$  can be decided by a test for a typical array before the algorithm operates. The procedure is offline and will not dramatically increase the system cost.

## 5. Conclusion

In this paper, a novel low-complexity RAB method is proposed which is easier to realize in practical situations and more robust to the look direction mismatch than other existing algorithms. The ASV is estimated by a closed-form formula so as to avoid utilizing the optimization software, and the IPN covariance matrix is reconstructed by a sampling progress. The proposed beamformer only requires prior knowledge of the antenna geometry and the angular sector in which the ASV is located. Simulation results have demonstrated that the proposed beamformer can achieve superior performance over the existing state of the art RAB methods. To simplify the illustration, the influence of the element pattern, the polarization, and the mutual coupling is not considered in this paper. However, these elements will be investigated in the future study.

## Competing Interests

The authors declare that they have no competing interests.

## References

- [1] H. L. Van Trees, *Optimum Array Processing*, John Wiley & Sons, Hoboken, NJ, USA, 2002.
- [2] W. Liu and S. Weiss, *Wideband Beamforming: Concepts and Techniques*, John Wiley & Sons, Chichester, UK, 2010.
- [3] H. Singh and R. M. Jha, "Trends in adaptive array processing," *International Journal of Antennas and Propagation*, vol. 2012, Article ID 361768, 20 pages, 2012.
- [4] U. Nickel, "Array processing for radar: achievements and challenges," *International Journal of Antennas and Propagation*, vol. 2013, Article ID 261230, 21 pages, 2013.
- [5] J. Capon, "High-resolution frequency-wavenumber spectrum analysis," *Proceedings of the IEEE*, vol. 57, no. 8, pp. 1408–1418, 1969.
- [6] S. A. Vorobyov, "Principles of minimum variance robust adaptive beamforming design," *Signal Processing*, vol. 93, no. 12, pp. 3264–3277, 2013.
- [7] L. Du, J. Li, and P. Stoica, "Fully automatic computation of diagonal loading levels for robust adaptive beamforming," *IEEE Transactions on Aerospace and Electronic Systems*, vol. 46, no. 1, pp. 449–458, 2010.
- [8] L. Chang and C.-C. Yeh, "Performance of DMI and eigenspace-based beamformers," *IEEE Transactions on Antennas and Propagation*, vol. 40, no. 11, pp. 1336–1348, 1992.
- [9] S. A. Vorobyov, A. B. Gershman, and Z.-Q. Luo, "Robust adaptive beamforming using worst-case performance optimization: a solution to the signal mismatch problem," *IEEE Transactions on Signal Processing*, vol. 51, no. 2, pp. 313–324, 2003.
- [10] H. Li, K. Wang, C. Wang, Y. He, and X. Zhu, "Robust adaptive beamforming based on worst-case and norm constraint," *International Journal of Antennas & Propagation*, vol. 2015, Article ID 765385, 7 pages, 2015.
- [11] Y. Gu and A. Leshem, "Robust adaptive beamforming based on interference covariance matrix reconstruction and steering vector estimation," *IEEE Transactions on Signal Processing*, vol. 60, no. 7, pp. 3881–3885, 2012.
- [12] L. Huang, J. Zhang, X. Xu, and Z. Ye, "Robust adaptive beamforming with a novel interference-plus-noise covariance matrix reconstruction method," *IEEE Transactions on Signal Processing*, vol. 63, no. 7, pp. 1643–1650, 2015.

- [13] H. Ruan and R. C. De Lamare, "Robust adaptive beamforming using a low-complexity shrinkage-based mismatch estimation algorithm," *IEEE Signal Processing Letters*, vol. 21, no. 1, pp. 60–64, 2014.
- [14] Z. Zhang, W. Liu, W. Leng, A. Wang, and H. Shi, "Interference-plus-noise covariance matrix reconstruction via spatial power spectrum sampling for robust adaptive beamforming," *IEEE Signal Processing Letters*, vol. 23, no. 1, pp. 121–125, 2016.
- [15] J. R. Guerci, "Theory and application of covariance matrix tapers for robust adaptive beamforming," *IEEE Transactions on Signal Processing*, vol. 47, no. 4, pp. 977–985, 1999.
- [16] A. Khabbazibasmenj, S. A. Vorobyov, and A. Hassanien, "Robust adaptive beamforming based on steering vector estimation with as little as possible prior information," *IEEE Transactions on Signal Processing*, vol. 60, no. 6, pp. 2974–2987, 2012.
- [17] F. Shen, F. Chen, and J. Song, "Robust adaptive beamforming based on steering vector estimation and covariance matrix reconstruction," *IEEE Communications Letters*, vol. 19, no. 9, pp. 1636–1639, 2015.
- [18] A. Hassanien, S. A. Vorobyov, and K. M. Wong, "Robust adaptive beamforming using sequential quadratic programming: an iterative solution to the mismatch problem," *IEEE Signal Processing Letters*, vol. 15, pp. 733–736, 2008.
- [19] J. Zhuang and A. Manikas, "Interference cancellation beamforming robust to pointing errors," *IET Signal Processing*, vol. 7, no. 2, pp. 120–127, 2013.
- [20] A. Elnashar, S. M. Elnoubi, and H. A. El-Mikati, "Further study on robust adaptive beamforming with optimum diagonal loading," *IEEE Transactions on Antennas and Propagation*, vol. 54, no. 12, pp. 3647–3658, 2006.

## Research Article

# A FPC-ROOT Algorithm for 2D-DOA Estimation in Sparse Array

Wenhao Zeng,<sup>1</sup> Hongtao Li,<sup>1</sup> Xiaohua Zhu,<sup>1</sup> and Chaoyu Wang<sup>2</sup>

<sup>1</sup>Nanjing University of Science and Technology, Nanjing, Jiangsu 210094, China

<sup>2</sup>China Shipbuilding 724 Research Institutions, Nanjing, Jiangsu 210003, China

Correspondence should be addressed to Hongtao Li; [liht@njust.edu.cn](mailto:liht@njust.edu.cn)

Received 24 December 2015; Revised 11 March 2016; Accepted 22 March 2016

Academic Editor: Jeich Mar

Copyright © 2016 Wenhao Zeng et al. This is an open access article distributed under the Creative Commons Attribution License, which permits unrestricted use, distribution, and reproduction in any medium, provided the original work is properly cited.

To improve the performance of two-dimensional direction-of-arrival (2D DOA) estimation in sparse array, this paper presents a Fixed Point Continuation Polynomial Roots (FPC-ROOT) algorithm. Firstly, a signal model for DOA estimation is established based on matrix completion and it can be proved that the proposed model meets Null Space Property (NSP). Secondly, left and right singular vectors of received signals matrix are achieved using the matrix completion algorithm. Finally, 2D DOA estimation can be acquired through solving the polynomial roots. The proposed algorithm can achieve high accuracy of 2D DOA estimation in sparse array, without solving autocorrelation matrix of received signals and scanning of two-dimensional spectral peak. Besides, it decreases the number of antennas and lowers computational complexity and meanwhile avoids the angle ambiguity problem. Computer simulations demonstrate that the proposed FPC-ROOT algorithm can obtain the 2D DOA estimation precisely in sparse array.

## 1. Introduction

Two-dimensional direction-of-arrival (2D DOA) [1–4] estimation plays an important role in array signal processing, and it usually utilizes L-shaped arrays, planar arrays, vector sensors, and so forth, to estimate the two-dimensional target angle. Compared with 2D DOA estimation of other arrays [5, 6], 2D DOA estimation of planar array is asymptotically unbiased where the target position can be determined precisely without the problem of angle ambiguity. Moreover, the phased-array radar in the planar array can utilize waveform diversity which makes it suitable for multiple targets and complex environments with enhanced performance of target recognition and target tracking. However, the planar array requires a large amount of array elements which results in tremendous demands of hardware equipment and increases the complexity and cost of design. Comparatively, the sparse array needs only a quite smaller number of elements, so it is a feasible remedy for the abovementioned problems, whereas, in this case, the problem of substantially rising average side lobes occurs, which accounts for its uncommon applications so far. Paper [5] lowers computational complexity of DOA estimation by introducing a preprocessing transformation

matrix but has poor performance in sparse array. Paper [7] achieves high-resolution DOA estimation in sparse array; however, it only works in uniform linear array (ULA).

Matrix completion [8–10] is an extension of compressive sensing (CS) [11, 12] and has been widely applied to image processing, remote sensing, and many other engineering fields [13, 14]. On the basis of low-rank matrix, matrix completion can recover the full matrix from an incomplete set of matrix entries with high probability by solving nuclear-norm optimization. Paper [15] proposed a fixed point and Bregman iterative methods for matrix rank minimization, which is a very fast, robust, and powerful algorithm. Paper [16] introduces a particularly simple yet highly efficient alternating projection algorithm and this algorithm is able to recover matrix from the minimum number of measurements necessary. Paper [17] provides a necessary and sufficient condition that quantifies when this heuristic successfully finds the minimum rank solution of a linear constraint set. The sparse received signal can be recovered to the full received signal by matrix completion, so that matrix completion has been applied to DOA estimation [14, 18].

This study proposes a Fixed Point Continuation Polynomial Roots (FPC-ROOT) algorithm. The proposed algorithm

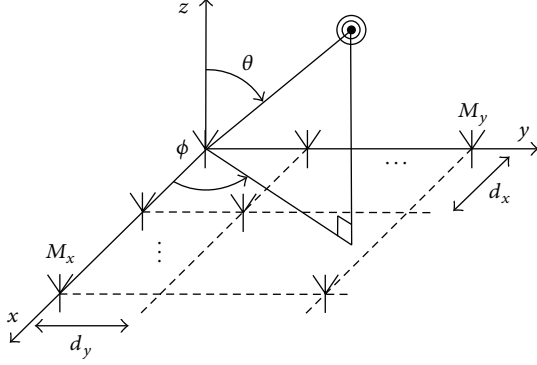


FIGURE 1: The uniform rectangular array.

establishes a signal model of matrix completion for 2D DOA estimation based on low-rank property of target in two-dimensional space domain, which turns out to meet the Null Space Property (NSP) and ensure the feasibility of 2D DOA estimation via matrix completion. By contrast to conventional algorithms, the proposed algorithm obtains left and right singular vectors of received signal matrix directly from the output of matrix completion algorithm instead of eigendecomposing autocorrelation matrix of received signal, for the benefit of lower dimensions. Besides, the proposed algorithm can avoid scanning of the 2D spectral peak by solving the polynomial roots, which reduces the computational complexity. In addition, it can estimate target angle accurately with less number of array units by adopting matrix completion.

## 2. Signal Model in Sparse Array

**2.1. The Signal Model of 2D DOA Estimation.** Suppose that the uniform rectangular array (URA) [3] is depicted in Figure 1.  $M_x$  and  $M_y$  are the number of elements in  $x$ -direction and  $y$ -direction, respectively. The corresponding element spacing is  $d_x$  and  $d_y$ .

Assume that there are multiple targets in the space. The number of snapshots is  $W$  and the number of targets is  $k$ , where the waveform of the  $i$ th ( $i = 1, 2, \dots, k$ ) target is  $s_i(t)$  and  $t = 1, 2, \dots, W$ . The target angles are  $(\phi_i, \theta_i)$ , where  $\phi_i$  and  $\theta_i$  express the elevation and azimuth angles of the  $i$ th target, respectively. Suppose the uncorrelated narrow-band signals are received in far field [19]; thus, the received signal of  $M_x$  elements in  $x$ -direction can be written as

$$L_x(t) = A_x S(t) + N_x(t), \quad (1)$$

where  $S(t) = \text{diag}(s_i(t))$  is a diagonal matrix of  $k \times k$  dimensions, the first  $k$  elements of  $s_i(t)$  are nonzero which correspond to  $k$  targets, and  $N_x(t)$  is the noise vector of the array.  $A_x$  is a  $M_x \times k$  dimensional steering vector, which can be given by

$$A_x = [a_x(\phi_1, \theta_1), a_x(\phi_2, \theta_2), \dots, a_x(\phi_k, \theta_k)]. \quad (2)$$

Assume the wavelength of received signal is  $\lambda$ ; then,  $a_x(\phi_i, \theta_i)$  is

$$[a_x(\phi_i, \theta_i)]_{m_x} = e^{j(2\pi/\lambda)d_x \sin(\theta_i) \cos(\phi_i)(m_x-1)}, \quad (3)$$

$$m_x = 1, 2, \dots, M_x.$$

Similarly, the received signal of  $M_y$  elements in  $y$ -direction can be represented as

$$L_y(t) = A_y S(t) + N_y(t), \quad (4)$$

where  $N_y(t)$  is the noise vector of the array.  $A_y$  is  $M_y \times k$  dimensional steering vector, which can be denoted as

$$A_y = [a_y(\phi_1, \theta_1), a_y(\phi_2, \theta_2), \dots, a_y(\phi_k, \theta_k)], \quad (5)$$

where  $a_y(\phi_i, \theta_i)$  is defined as

$$[a_y(\phi_i, \theta_i)]_{m_y} = e^{j(2\pi/\lambda)d_y \sin(\theta_i) \sin(\phi_i)(m_y-1)}, \quad (6)$$

$$m_y = 1, 2, \dots, M_y.$$

In conclusion, the received signal model of full array is demonstrated as

$$X(t) = A_x S(t) A_y^T + N_R(t), \quad t = 1, \dots, N. \quad (7)$$

When the power of noise matrix  $N_R(t)$  is much smaller than the signal power, we can get that  $\text{rank}(X(t)) \leq \text{rank}(S(t)) = k$ ; in other words, matrix  $X(t)$  is low-rank [10]. And matrix in (7) is consistent with strong incoherence property [15], so it can be recovered precisely with high probability via matrix completion.

**2.2. Matrix Completion.** With regard to the sparsity of signals, CS can sample signals at far lower sampling frequency than Nyquist sampling frequency and meanwhile reconstruct original signals precisely. In CS, the target to be recovered is a vector; however, on some practical occasions, it normally refers to a matrix and is sensitive to data missing, data corruption, and so on.

Matrix completion is an extension of CS. CS exploits the sparsity of signals; nevertheless, matrix completion utilizes the sparsity of matrix singular values, namely, the low-rank property, and reconstructs full matrix by solving nuclear-norm optimization.

Suppose  $M \in R^{n \times n}$  is an original low-rank matrix, where  $\text{rank}(M) = r$ ,  $r \ll n$ . Matrix completion refers to recovering the whole elements of matrix  $M$  from its partial elements. Let the available entries of matrix be  $\{M_{ij}, (i, j) \in \Omega\}$ , where  $\Omega$  is a random sampled subset of the whole elements; then, the matrix completion can be denoted as [10]

$$\begin{aligned} \min \quad & \|X\|_* , \\ \text{s.t.} \quad & X_{ij} = M_{ij}, \quad (i, j) \in \Omega, \end{aligned} \quad (8)$$

where matrix  $X$  is the estimated value of matrix  $M$ ;  $\|X\|_*$  represents the nuclear norm of the matrix  $X$ .

**2.3. The Sparse Array Model.** We sample elements from URA at random. Let the number of sampled elements be  $m$  with the corresponding element positions unchanged and the unsampled units removed; thus, a new sparse array is set up. To recover matrix precisely via matrix completion, the required number of samples is  $m \geq r(n_1 + n_2 - r)$  [10], while  $n_1, n_2$  are the numbers of rows and columns of the matrix, and  $r$  is the rank of the matrix. Suppose the received signal matrix in sparse array is  $X_s(t)$ ; then,  $X_s(t)$  is related to  $X(t)$  by

$$\begin{aligned} X_s(t)_{ij} &= X(t)_{ij}, & (i, j) \in \Omega, \\ X_s(t)_{ij} &= 0, & (i, j) \notin \Omega, \end{aligned} \quad (9)$$

where  $\Omega$  is the set of element positions in sparse array.

### 3. The Proposed Algorithm

**3.1. The Signal Model for 2D-DOA Estimation Based on Matrix Completion.** According to (7), the received signal matrix  $X(t)$  in URA is low-rank. Regard  $X_R(t)$  as the recovered matrix by matrix completion, so it can be deduced that

$$\begin{aligned} \min \quad & \|X_R(t)\|_* \\ \text{s.t.} \quad & X_R(t)_{ij} = X_s(t)_{ij}, \quad (i, j) \in \Omega. \end{aligned} \quad (10)$$

If a signal model meets NSP, the rank minimization of this model is equivalent to its nuclear-norm minimization [13]. So we introduce the projection  $P_\Omega$  as follows:

$$P_\Omega(M) = \begin{cases} M_{ij}, & (i, j) \in \Omega \\ 0, & (i, j) \notin \Omega. \end{cases} \quad (11)$$

From (11), we can see that (10) can be expressed as

$$\begin{aligned} \min \quad & \|X_R(t)\|_*, \\ \text{s.t.} \quad & P_\Omega(X_R(t)) = P_\Omega(X_s(t)), \end{aligned} \quad (12)$$

where  $X_R(t)$  is the estimated matrix. The null space of projection  $P_\Omega$  is

$$\text{Null}(P_\Omega) = \{M \in R^{n_1 \times n_2} : P_\Omega(M) = 0\}. \quad (13)$$

According to NSP, we are unable to recover a matrix if it belongs to the null space of projection  $P_\Omega$ . From (4), we can get that

$$\begin{aligned} [a_x(\phi_i, \theta_i)]_{m_x} &= e^{j(2\pi/\lambda)d_x \sin(\theta_i) \cos(\phi_i)(m_x-1)} \neq 0, \\ m_x &= 1, 2, \dots, M_x. \end{aligned} \quad (14)$$

In (7), the arbitrary elements of  $A_x$  and  $A_y$  are both nonzero and the first  $k$  elements in  $s_i(t)$  are nonzero, so the diagonal elements of  $k \times k$  dimensional diagonal matrix are nonzero. Arbitrary elements of  $X(t)$  are nonzero based on matrix multiplication property. Therefore, it can be concluded that whichever sampling operator is selected, there is always  $P_\Omega(X(t)) \neq 0$ ; in other words,  $P_\Omega(X(t)) \notin \text{Null}(P_\Omega)$ , which meets the Null Space Property.

**3.2. The FPC-ROOT Algorithm.** Suppose  $\text{svd}(X_R(t)) = U\Sigma V$  and matrices  $U$  and  $V$  are the left and right singular value matrix of  $X_R(t)$ . FPC-ROOT algorithm can obtain  $U$  and  $V$  directly by matrix completion based on the low-rank property of  $X(t)$  and realizes 2D DOA estimation by computing the polynomial roots.

Firstly, to solve problem (12), we achieve the left and right singular value matrices  $U$  and  $V$  of estimated value  $X_R(t)$  in full array by FPC algorithm. And then, we solve the autocorrelation matrix of received signal  $X(t)$  in full array, so the eigendecomposition of the autocorrelation matrix is

$$\begin{aligned} R_X &= X(t)X(t)^H = A_x S(t)A_y^T A_y^* S(t)^* A_x^H + N_{m1} \\ &= A_x R_{m1} A_x^H + N_{m1} = U_S \Sigma_S U_S^H + U_N \Sigma_N U_N^H, \end{aligned} \quad (15)$$

where  $t = 1, \dots, W$ ,  $X(t)^H$  is the conjugate transpose matrix of  $X(t)$ ,  $U_S$  is the signal subspace,  $U_N$  is the noise subspace, and  $R_{m1}$  is

$$R_{m1} = S(t)A_y^T A_y^* S(t)^*. \quad (16)$$

And  $N_{m1}$  in (15) can be expressed as

$$\begin{aligned} N_{m1} &= A_x S(t)A_y^T N_R(t)^H + N_R(t)A_y^* S(t)^* A_x^H \\ &\quad + N_R(t)N_R(t)^H. \end{aligned} \quad (17)$$

It is obvious that the spanned subspaces of  $A_x$  and  $U_S$  are identical. We solve the conjugate transpose of autocorrelation matrix  $R_X$  and then it can be concluded that

$$\begin{aligned} R_X^H &= X(t)^H X(t) = A_y^* S(t)^* A_x^H A_x S(t)A_y^T + N_{m2} \\ &= A_y^* R_{m2} A_y^T + N_{m2} = V_S \Sigma_S V_S^H + V_N \Sigma_N V_N^H, \end{aligned} \quad (18)$$

where  $t = 1, \dots, N$ , and similarly  $R_{m2}$  is

$$R_{m2} = S(t)^* A_x^H A_x S(t) \quad (19)$$

$N_{m2}$  can be expressed as

$$\begin{aligned} N_{m2} &= A_y^* S(t)^* A_x^H N_R(t) + N_R(t)^H A_x S(t)A_y^T \\ &\quad + N_R(t)^H N_R(t). \end{aligned} \quad (20)$$

So the space spanned by  $A_y^*$  is the same as the space spanned by  $V_S$ .

Based on singular value decomposition, it is easy to know that left and right singular value matrices  $U$  and  $V$  are related to the eigendecomposition of autocorrelation matrix  $R_X$  by

$$U = U_S + U_N, \quad (21)$$

$$V = V_S + V_N.$$

So the left and right singular vectors of received signal matrix can be obtained directly from the output of matrix completion algorithm instead of eigendecomposing autocorrelation matrix of received signal and the computational complexity of the proposed algorithm obtained a corresponding reduction.

Consider a polynomial as

$$f(z) = u_l^H p(z) \quad (l = k + 1, k + 2, \dots, N), \quad (22)$$

where  $u_l$  is the  $l$ th eigenvector of matrix  $R_X$  and  $p(z) = [1, z, \dots, z^{N-1}]^T$ . It can be deduced that the corresponding ROOT-MUSIC polynomial is

$$f_x(z) = z^{N-1} p^T(z^{-1}) U_N U_N^H p(z). \quad (23)$$

By solving the polynomial roots, the proposed algorithm can avoid scanning of the 2D spectral peak. Taking use of the orthogonality of signal subspace, the above equation can be converted to

$$P_x(z) = z^{N-1} p^T(z^{-1}) (I - U_S U_S^H) p(z). \quad (24)$$

The dimensionality of  $U_S$  is smaller than  $U_N$ ; hence, the proposed algorithm effectively reduced the computational complexity by reducing the dimension of the subspace matrix. Then, the vector corresponding to the roots of polynomial is

$$z_x = \left[ \exp\left(\frac{j2\pi d_x \cos \phi_1 \sin \theta_1}{\lambda}\right), \dots, \exp\left(\frac{j2\pi d_x \cos \phi_k \sin \theta_k}{\lambda}\right) \right]. \quad (25)$$

Thus,

$$r_x = [\cos \phi_1 \sin \theta_1, \dots, \cos \phi_k \sin \theta_k]. \quad (26)$$

Similarly, it can be obtained that

$$r_y = [\sin \phi_1 \sin \theta_1, \dots, \sin \phi_k \sin \theta_k]. \quad (27)$$

Hence, the estimated angles of targets are

$$\begin{aligned} [\theta_1, \theta_2, \dots, \theta_k] &= \arcsin \sqrt{r_x^2 + r_y^2} \\ [\phi_1, \phi_2, \dots, \phi_k] &= \arctan\left(\frac{r_x}{r_y}\right). \end{aligned} \quad (28)$$

In summary, the proposed FPC-ROOT algorithm in this paper can be programmed as follows.

#### Fixed Point Continuation Polynomial Roots (FPC-ROOT) Algorithm

*Initialize.* Given  $X_s(t)$ , the projection  $P_\Omega$  is corresponding to element positions in the sparse array:

- (1) Solve (12) to get left and right singular value matrices  $U_S$  and  $V_S$ .
- (2) Construct the polynomial roots (24).
- (3) Solve (24) to get

$$\begin{aligned} r_x &= [\cos \phi_1 \sin \theta_1, \dots, \cos \phi_k \sin \theta_k], \\ r_y &= [\sin \phi_1 \sin \theta_1, \dots, \sin \phi_k \sin \theta_k]. \end{aligned} \quad (29)$$

- (4) Determine the targets angles

$$\begin{aligned} [\theta_1, \theta_2, \dots, \theta_k] &= \arcsin \sqrt{r_x^2 + r_y^2}, \\ [\phi_1, \phi_2, \dots, \phi_k] &= \arctan\left(\frac{r_x}{r_y}\right). \end{aligned} \quad (30)$$

End.

**3.3. Dimensionality Reduction.** In normal 2D-DOA estimation, DOA estimation is achieved through autocorrelation matrix of a vector which is transformed from the signal matrix. Suppose the signal matrix is  $M_x \times M_y$ , so the dimension of the transformed vector is  $M_x M_y \times 1$ ; then, the dimension of the autocorrelation matrix is  $M_x M_y \times M_x M_y$ . In the proposed method, we obtain left and right singular vector directly from the signal matrix, avoiding solving the autocorrelation matrix, greatly reducing the dimension of the target matrix.

## 4. Simulations

In this section, several simulations for 2D DOA estimation are conducted to demonstrate the feasibility and effectiveness of the proposed algorithm in sparse array. In these experiments, we sample 1200 elements from full array at random to formulate a sparse array. The full array is an URA of  $64 \times 64$  elements, where the total number of elements is  $m = 4096$  and the corresponding element spacing in  $x$ -direction and  $y$ -direction is  $d_x = d_y = \lambda/2$ .

In the first examples, 2D DOA estimation of sparse array is shown. Let three targets be in the space domain, whose elevation and azimuth angles of 2D-DOA are  $(10^\circ, 15^\circ)$ ,  $(20^\circ, 25^\circ)$ , and  $(30^\circ, 35^\circ)$ , respectively, and input signal-to-noise ratio (SNR) is 20 dB. Let the number of snapshots be 50. Suppose the received signals are narrow-band in far field and the signal sources are uncorrelated; then, 100 experiment results of 2D-DOA estimation by FPC-ROOT algorithm are depicted in Figure 2. The proposed algorithm samples 1200 elements to construct a sparse array; in other words, 70% units are removed from full array. From Figure 2, it can be seen that the targets' angles can be achieved precisely by the proposed algorithm in sparse array.

In the second experiment, recovery errors by matrix completion in sparse array with different SNR are examined. We recover a full matrix from a sparse matrix using FPC algorithm. Suppose the full matrix is  $M$  and the recovered matrix is  $X$ ; then, the measurement criterion of recovery errors by matrix completion is  $\|M - X\|_2 / \|M\|_2$ . Figure 3 illustrates the variation of recovery errors by matrix completion with different SNR when the numbers of sparse array elements are 900, 1200, and 1500, respectively. It can be deduced easily from this experiment that recovery errors by FPC algorithm are inversely proportional to SNR. The larger the SNR is, the more similar the matrix  $M$  is to low-rank matrix. Simultaneously, the more elements the sparse array has, the closer the recovered signals are to the full array and the smaller the corresponding recovery errors are.

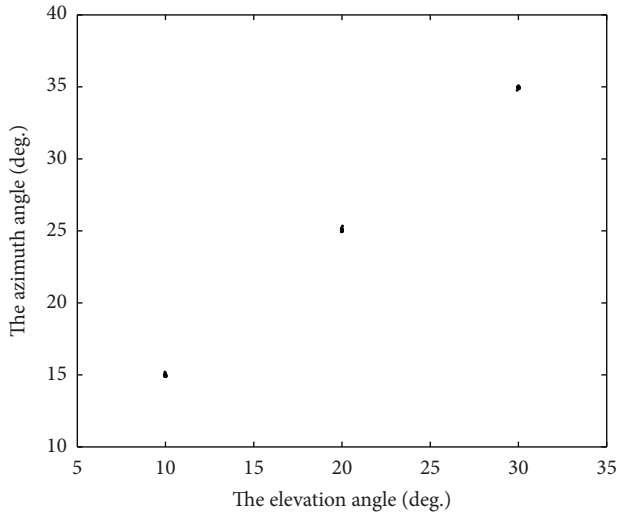


FIGURE 2: 2D DOA estimation via FPC-ROOT algorithm.

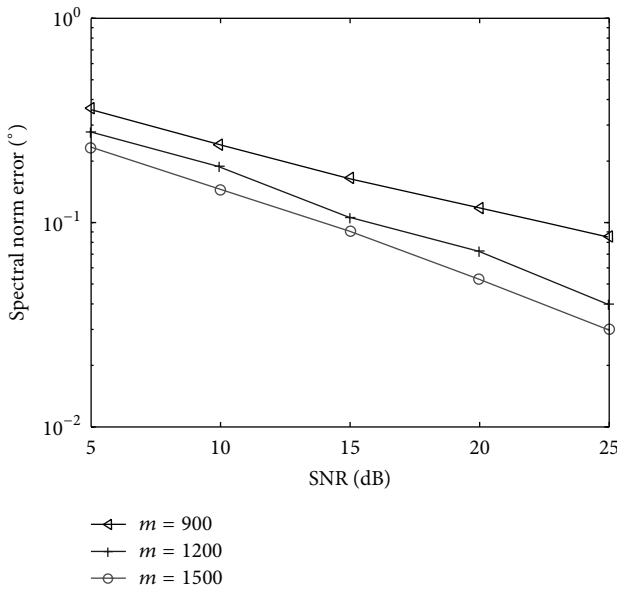


FIGURE 3: Recovery errors by matrix completion with different elements and SNR.

In the third experiment, root mean square error (RMSE) of 2D DOA estimation based on matrix completion is discussed. When 500 Monte Carlo simulations are performed, Figure 4 exhibits RMSE with different SNR via various algorithms. When the SNR is high, the recovery of matrix completion has a high precision, so the RMSE of DOA estimation is decreased. And it is evident that the proposed algorithm has higher accuracy for both elevation and azimuth angles estimation than 2D-MUSIC algorithms.

In the last experiment, RMSE by FPC-ROOT algorithm with different SNR and elements is demonstrated. Let the number of snapshots be 50 and let 500 Monte Carlo experiments be implemented. Figure 5 shows RMSE by FPC-ROOT

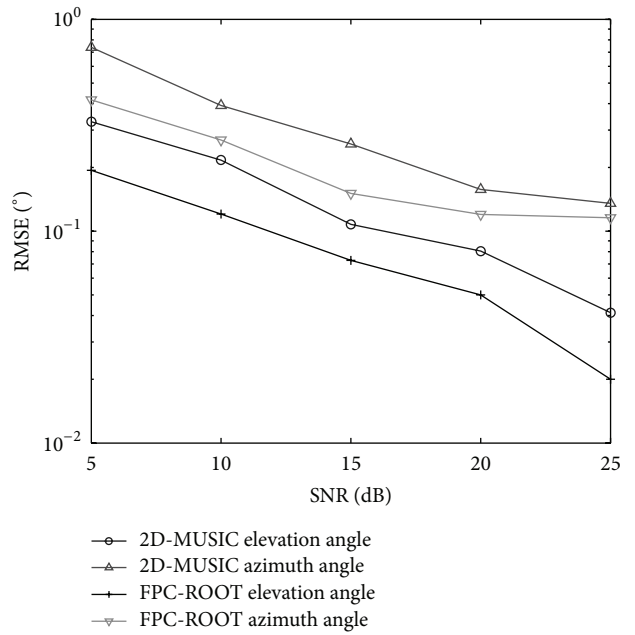


FIGURE 4: RMSE of 2D DOA estimation based on matrix completion.

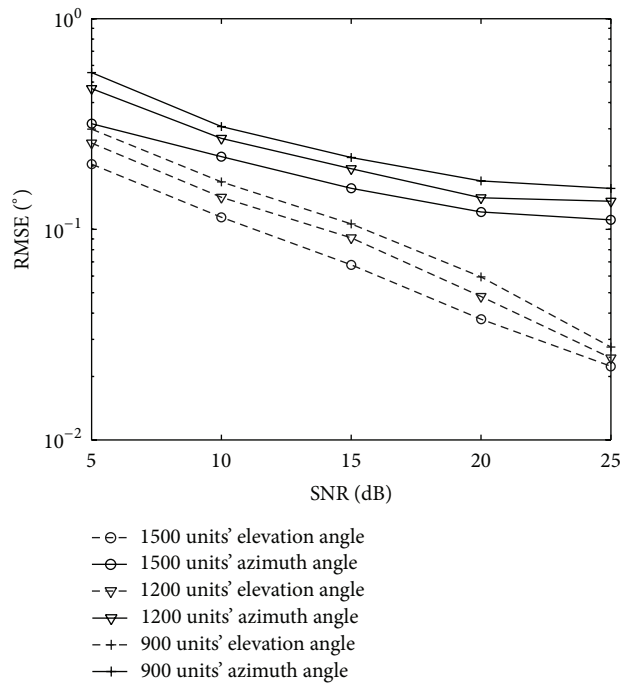


FIGURE 5: RMSE versus SNR with different elements by FPC-ROOT algorithm.

algorithm when SNR and the number of elements vary. As the recovery errors by FPC algorithm are inversely proportional to SNR, the RMSE of DOA estimation is decreased at high SNR. From this simulation, it can be concluded that the estimation accuracy by FPC-ROOT algorithm is proportional to the number of elements.

## 5. Conclusion

In this paper, a FPC-ROOT algorithm is proposed based on matrix completion, which can achieve high accuracy of 2D DOA estimation with reduced antenna units. The proposed algorithm obtains left and right singular vectors of received signal by the output of matrix completion algorithm directly instead of eigendecomposing the autocorrelation matrix of received signal, for the benefit of lower dimensions. Besides, by computing polynomial roots, the proposed algorithm can avoid the scanning of two-dimensional spectral peak, which cuts down the computational complexity.

## Competing Interests

The authors declare that there is no conflict of interests regarding the publication of this paper.

## Acknowledgments

This work was supported by the National Natural Science Foundation of China (Grant no. 61401204), Postdoctoral Science Foundation of Jiangsu Province (Grant no. 1501104C), Technology Research and Development Program of Jiangsu Province (Grant no. BY2015004-03), and the Fundamental Research Funds for the Central Universities (Grant no. 30916011319).

## References

- [1] J. Li and X. Zhang, "Closed-form blind 2D-DOD and 2D-DOA estimation for MIMO radar with arbitrary arrays," *Wireless Personal Communications*, vol. 69, no. 1, pp. 175–186, 2013.
- [2] Z. Zheng, G. Li, and Y. Teng, "Simplified estimation of 2D DOA for coherently distributed sources," *Wireless Personal Communications*, vol. 62, no. 4, pp. 907–922, 2012.
- [3] P. Heidenreich, A. M. Zoubir, and M. Rubsamen, "Joint 2-D DOA estimation and phase calibration for uniform rectangular arrays," *IEEE Transactions on Signal Processing*, vol. 60, no. 9, pp. 4683–4693, 2012.
- [4] M. Agatonović, Z. Stanković, N. Dončov, L. Sit, B. Milovanović, and T. Zwick, "Application of artificial neural networks for efficient high-resolution 2D DOA estimation," *Radioengineering*, vol. 21, no. 4, pp. 1178–1186, 2012.
- [5] W. Zhang, W. Liu, J. Wang, and S. Wu, "Computationally efficient 2-D DOA estimation for uniform rectangular arrays," *Multidimensional Systems and Signal Processing*, vol. 25, no. 4, pp. 847–857, 2014.
- [6] L. Yuan, R. Jiang, and Y. Chen, "Gain and phase autocalibration of large uniform rectangular arrays for underwater 3-D sonar imaging systems," *IEEE Journal of Oceanic Engineering*, vol. 39, no. 3, pp. 458–471, 2014.
- [7] N. Hu, Z. Ye, X. Xu, and M. Bao, "DOA estimation for sparse array via sparse signal reconstruction," *IEEE Transactions on Aerospace & Electronic Systems*, vol. 49, no. 2, pp. 760–773, 2013.
- [8] O. Klopp, "Noisy low-rank matrix completion with general sampling distribution," *Bernoulli*, vol. 20, no. 1, pp. 282–303, 2014.
- [9] H. Ji, C. Liu, Z. Shen, and Y. Xu, "Robust video denoising using low rank matrix completion," in *Proceedings of the IEEE Conference on Computer Vision and Pattern Recognition (CVPR '10)*, pp. 1791–1798, San Francisco, Calif, USA, June 2010.
- [10] E. J. Candès and B. Recht, "Exact matrix completion via convex optimization," *Foundations of Computational Mathematics*, vol. 9, no. 6, pp. 717–772, 2009.
- [11] D. L. Donoho, "Compressed sensing," *IEEE Transactions on Information Theory*, vol. 52, no. 4, pp. 1289–1306, 2006.
- [12] J. Cheng, Q. Ye, H. Jiang, D. Wang, and C. Wang, "STCDG: an efficient data gathering algorithm based on matrix completion for wireless sensor networks," *IEEE Transactions on Wireless Communications*, vol. 12, no. 2, pp. 850–861, 2013.
- [13] W. Chen, Q. Tian, J. Liu, and Q. Wang, "Nonlocal low-rank matrix completion for image interpolation using edge detection and neural network," *Signal, Image and Video Processing*, vol. 8, no. 4, pp. 657–663, 2014.
- [14] D. S. Kalogerias and A. P. Petropulu, "Matrix completion in colocated mimo radar: recoverability, bounds & theoretical guarantees," *IEEE Transactions on Signal Processing*, vol. 62, no. 2, pp. 309–321, 2014.
- [15] S. Ma, D. Goldfarb, and L. Chen, "Fixed point and Bregman iterative methods for matrix rank minimization," *Mathematical Programming*, vol. 128, no. 1-2, pp. 321–353, 2011.
- [16] J. Tanner and K. Wei, "Normalized iterative hard thresholding for matrix completion," *SIAM Journal on Scientific Computing*, vol. 35, no. 5, pp. S104–S125, 2013.
- [17] B. Recht, W. Xu, and B. Hassibi, "Necessary and sufficient conditions for success of the nuclear norm heuristic for rank minimization," in *Proceedings of the 47th IEEE Conference on Decision and Control (CDC '08)*, pp. 3065–3070, Cancún, Mexico, December 2008.
- [18] P. Pal and P. P. Vaidyanathan, "A grid-less approach to under-determined direction of arrival estimation via low rank matrix denoising," *IEEE Signal Processing Letters*, vol. 21, no. 6, pp. 737–741, 2014.
- [19] H. Krim and M. Viberg, "Two decades of array signal processing research: the parametric approach," *IEEE Signal Processing Magazine*, vol. 13, no. 4, pp. 67–94, 1996.

## Research Article

# Efficient Design of the Microstrip Reflectarray Antenna by Optimizing the Reflection Phase Curve

**Xing Chen, Qiang Chen, Pan Feng, and Kama Huang**

*College of Electronic and Information Engineering, Sichuan University, Chengdu 610064, China*

Correspondence should be addressed to Xing Chen; [xingc@live.cn](mailto:xingc@live.cn)

Received 5 January 2016; Accepted 27 March 2016

Academic Editor: Giuseppe Mazzarella

Copyright © 2016 Xing Chen et al. This is an open access article distributed under the Creative Commons Attribution License, which permits unrestricted use, distribution, and reproduction in any medium, provided the original work is properly cited.

The microstrip reflectarray antenna is an attractive directional antenna combining advantages of both the reflector and the microstrip array antenna. For the design of this kind of antenna, the conventional method, which is based on the reflection phase curve, may not be effective because of the approximations made in the design procedure. The common optimization method that employs an optimization algorithm in conjunction with the full-wave simulation to optimize the antennas' structural parameters is able to achieve better performances in comparison with the conventional method; but it is impractical for large-scale microstrip reflectarray antennas due to too many structural parameters from variable reflection elements. To tackle the design problem of the microstrip reflectarray antenna, a new method is proposed for the first time. It optimizes the reflection phase curve rather than the structural parameters and then utilizes the optimized reflection phase curve to design the antenna. A microstrip reflectarray antenna working at 5.8 GHz and with a fixed size of 300 mm × 300 mm is designed for high gain as a sample design. The results show that the proposed method has greatly improved the antenna's gain over 2.2 dB (from 19.7 dBi to 21.9 dBi) in comparison with the conventional design method, and it only needs to optimize 6 structural parameters, in contrast to 22 for the common optimization method.

## 1. Introduction

The microstrip reflectarray antenna proposed by Malagisi [1] has raised significant interest in the high-gain antenna field, due to its salient features combining some of the best features of reflector and array antennas [2]. It provides an attractive alternative to conventional directive antennas and has been widely applied in many fields recently, for example, direct broadcast satellite (DBS), space telemetry, and radar applications [3–5].

A microstrip reflectarray antenna usually consists of a feed source and a reflector. The feed source is an antenna placed at a certain distance from the reflector, and the reflector is an array of microstrip patches and/or slots etched on a grounded dielectric substrate. Microwave energy is emitted from the feed source and scattered by the reflector. Elements in the reflector are designed to generate proper phase compensations associated with the path lengths from the feed source so that a planar phase surface is formed in

front of the aperture of the antenna, and in this way the directional radiation property with high gain can be achieved.

The conventional design method for the microstrip reflectarray antenna contains the following major steps: analyzing the phase characteristics of the reflection elements using numerical simulations to obtain a reflection phase curve, which describes the one-to-one correspondence between the phase compensation and a structural parameter that controls the elements' reflection phase; calculating the required phase compensation for each reflection element according to the distance and the relative location between the reflection element and the feeding source; and finally determining the structural parameters of the reflection elements based on the reflection phase curve and the required phase compensation [2, 6–8].

This conventional design method is simple and has been adopted for most microstrip reflectarray antennas. However, its design may not be an optimum one because of the approximations made in the design procedure as described

as follows. The reflection phase curve is obtained under the assumption of a normal incidence [9], but actually the incident angle may vary and the reflection phase curves are different with different incident angles [10]. The feed source and the reflection elements are considered as sizeless points in the calculation of the path length for determining the phase compensation [2]. The coupling effect between the reflection elements is ignored in the design procedure but it actually may not be negligible when the distance between patch edges is small (e.g., less than a quarter wavelength) [2, 11]. The field diffracted by the reflector's edges, the shielding effect of the feed source, and the support frame are not taken into account in the design procedure [2, 12]. Those approximations may bring forth errors in the design and subsequently deteriorate the performances of the antennas designed.

A widely used method for antenna design employs an optimization algorithm such as the genetic algorithm (GA) in conjunction with the full-wave simulation to optimize the antenna's structural parameters [13–16]. The optimization algorithm enables design of antennas with optimum performance, and the full-wave simulation allows taking all the involved effects into account without the above-mentioned approximations. This method was employed in the authors' previous work [17] to design a microstrip reflectarray antenna consisting of  $7 \times 7$  reflection elements, and encouraging results were achieved; for example, the antenna's gain has been considerably improved over 1.4 dBi (from 18.1 dBi to 19.5 dBi) in comparison with the conventional design method.

However, the aforementioned common optimization method is impractical for a large-scale microstrip reflectarray because its large number of structural parameters deriving from its variable reflection elements would result in too many unknown parameters needed in the optimization. Taking the microstrip reflectarray studied in [17] as an example, the number of the unknown structural parameters is 10 for the antenna containing  $7 \times 7$  reflection elements, but it will become 27 if the quantity of the reflection elements rises to  $13 \times 13$ . In practical applications, microstrip reflectarray antennas are usually of much more reflection elements, which would result in not only a huge computation burden but also a difficulty of achieving good results using an optimization algorithm. That is why very little work published in literature has employed the optimization method to design a microstrip reflectarray antenna.

To solve the design problem of microstrip reflectarray antennas, this paper proposes a novel method, which employs an optimization algorithm in conjunction with the full-wave simulation to optimize the reflection phase curve rather than the structural parameters and then uses the optimized reflection phase curve to design a microstrip reflectarray antenna. This method is able to make full use of the advantages of the optimization algorithm and the full-wave simulation so as to achieve better design in comparison with the conventional method. Meanwhile, it can reduce the number of unknown parameters needed in the optimization to a low level and thus possesses the capacity of effectively designing large-scale microstrip reflectarray antennas.

The other sections of this paper are organized as the follows. Section 2 introduces the configuration of the microstrip reflectarray antenna to be designed in this work. The conventional design method is described and its design results are given in Section 3. The principle and procedure of the proposed design method are presented in Section 4. Finally, in Section 5, conclusions are drawn.

## 2. Antenna Configuration

To validate the proposed design method, it is employed to design a sample  $300 \text{ mm} \times 300 \text{ mm}$  microstrip reflectarray antenna operating at 5.8 GHz with high gain and end-fire property (i.e., the main beam of the antenna is set to be perpendicular to the reflector). As illustrated in Figure 1(a), the feed source of the antenna is a rectangular patch antenna, whose configuration and parameters are shown in Figure 1(b). It is propped by three metal sticks and placed at a distance of  $h_1$  from the reflector. The reflector consists of a metal ground fabricated by an aluminum board with thickness of 4.0 mm and a printed circuit board (PCB) with relative dielectric constant  $\epsilon_r = 2.65$  and thickness  $h_2 = 1 \text{ mm}$ . The PCB and the metal ground are separated by an air layer with thickness  $h_3$ .

As illustrated in Figure 1(c), various reflection elements are etched on the PCB. Because of the geometrical symmetry and the antenna's end-fire property, the reflection elements whose distances to the center of the reflector are equal should be of the same reflection phase and thus the same structural parameters. Hence, the reflection elements can be indexed from 1 to  $n$  according to their distance to the center where  $n$  is the quantity of groups of the elements with different dimensions, as illustrated in Figure 1(c).

As shown in Figure 1(d), each element contains a square patch with a side length  $L_1$  as well as a square ring with an outer side length  $L_2$  and thickness  $W$ , and it occupies a square area  $L * L$ . To simplify the structure of the reflection element, in this work,  $L_1$  and  $W$  are taken as  $L_1(i) = k_1 * L_2(i)$  and  $W(i) = k_2 * L_2(i)$ , where  $k_1$  and  $k_2$  are two constant coefficients and  $i$  is the index number of the element. Thus, for a reflection element, among its structural parameters  $L_1$ ,  $L_2$ , and  $W$ , only one of them is independent from the others. In this work,  $L_2$  is selected to represent the element dimension.

## 3. Design Using the Conventional Design Method

To provide a benchmark for comparison with and an initial design for the proposed method, the conventional design method is employed to design the microstrip reflectarray antenna introduced in the last section.

The side length  $L$  of the square area occupied by a reflection element, which is also the distance between the adjacent element centers, is set to be  $0.6\lambda$ , where  $\lambda$  is the free-space wavelength at the working frequency 5.8 GHz. This setting can help to avoid the appearance of grating lobes to a certain extent [2]. For a reflectarray antenna, the distance  $h_1$  is required to be large enough so that the incident wave to

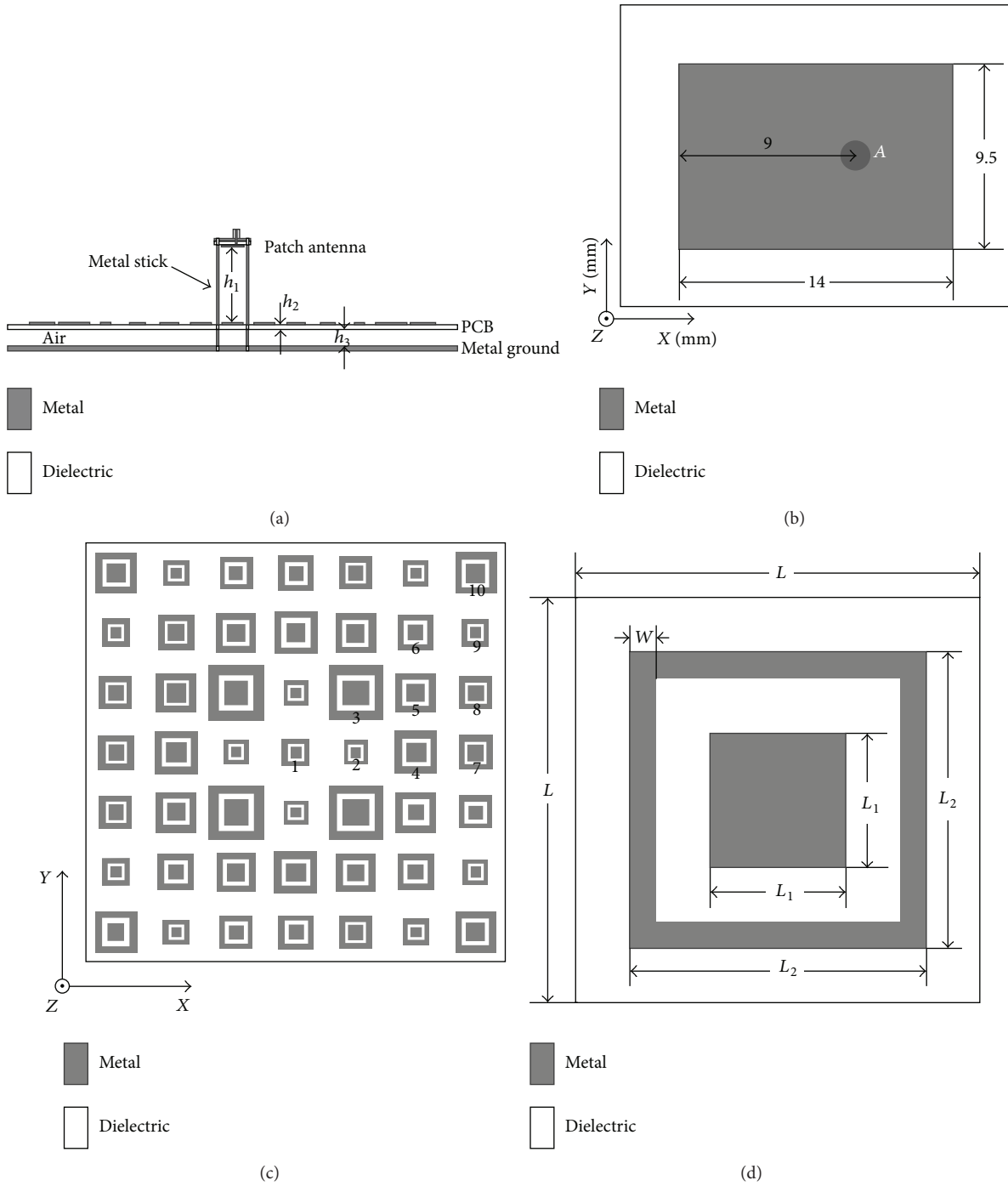


FIGURE 1: The configuration of the microstrip reflectarray antenna: (a) side view of the reflectarray antenna; (b) top view of the patch antenna; (c) top view of the reflector; (d) configuration of a reflection element.

the reflection elements can be approximated as a plane wave [10, 18], but  $h_1$  cannot be too large in order to ensure that the reflector covers at least the main lobe of the feed source. As a compromise,  $h_1$  is set to be 100 mm in this work.

The reflection phase curve plays a key role in the conventional method for designing a microstrip reflectarray antenna. To compensate various phases, the reflection phase curve should cover a phase range of 360 degrees,

and meanwhile the curve should be monotonically smooth in order to reduce the fabrication sensitivity [2]. After a serial of parameter sweeps using the full-wave simulation and employing the method presented in [9] for analyzing the reflection characteristics of the reflection elements, a monotonically smooth reflection phase curve is derived and presented in Figure 2 for  $k_1 = 0.5$ ,  $k_2 = 0.15$ , and  $h_3 = 12$  mm. In this work, the full-wave simulation is

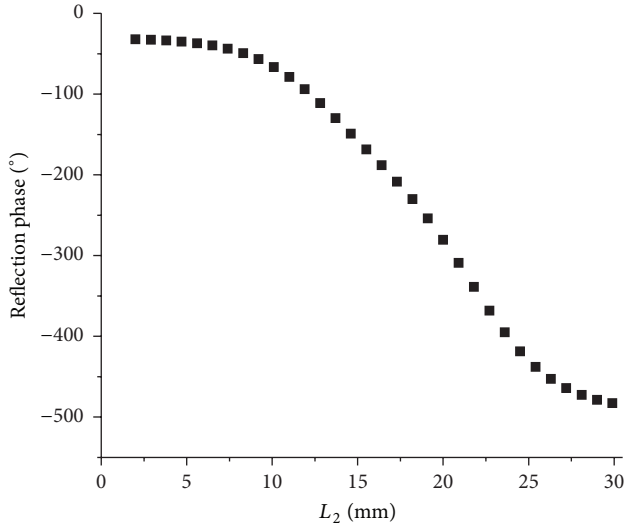


FIGURE 2: The reflection phase versus the square ring outer length  $L_2$ .

conducted by employing the popular commercial software CST MICROWAVE STUDIO (MWS) based on the finite integration technique (FIT).

Then, the required phase compensation for each reflection element is calculated using the equation [13]

$$\phi_i = k(R_i - \vec{r}_i \cdot \vec{r}_0), \quad (1)$$

where  $k$  is the propagation constant in vacuum, which is equal to  $2\pi/\lambda$ ;  $R_i$  is the distance from the phase center of the feed source to  $i$ th element;  $\vec{r}_i$  is the vector from the center of the reflectarray to the element; and  $\vec{r}_0$  is the unit vector in the main beam direction.

In this work, the main beam of the antenna is set to be perpendicular to the reflector so that the angle between  $\vec{r}_i$  and  $\vec{r}_0$  is 90 degrees making the dot product  $\vec{r}_i \cdot \vec{r}_0$  zero. Then, (1) is simplified to

$$\phi_i = kR_i. \quad (2)$$

Because the size of the reflector is fixed to be  $300 \text{ mm} \times 300 \text{ mm}$  and the element spacing  $L$  is  $0.6\lambda \approx 31 \text{ mm}$ , the reflector can only contain a maximum of  $9 \times 9$  reflection elements. The reflection elements have 15 different sizes. According to (2), the required reflection phase for those elements are (in degree)  $-24, -351.3, -319.9, -260.8, -232.8, -153.9, -129, -104.8, -35.5, -289.3, -330.5, -309.7, -249.4, -155.2,$  and  $-33.8$ , respectively. By referring to the reflection phase curve in Figure 2, the square ring outer length  $L_2(i)$  can be determined as follows (in mm):  $L_2(1) = 23.22, L_2(2) = 22.17, L_2(3) = 21.24, L_2(4) = 19.35, L_2(5) = 18.3, L_2(6) = 14.82, L_2(7) = 13.68, L_2(8) = 12.48, L_2(9) = 23.61, L_2(10) = 20.28, L_2(11) = 21.54, L_2(12) = 20.91, L_2(13) = 18.93, L_2(14) = 14.88,$  and  $L_2(15) = 23.55$ .

For this microstrip reflectarray designed using the conventional method, its characteristics are simulated by CST and shown in Figures 3 and 4. One observes from Figure 3

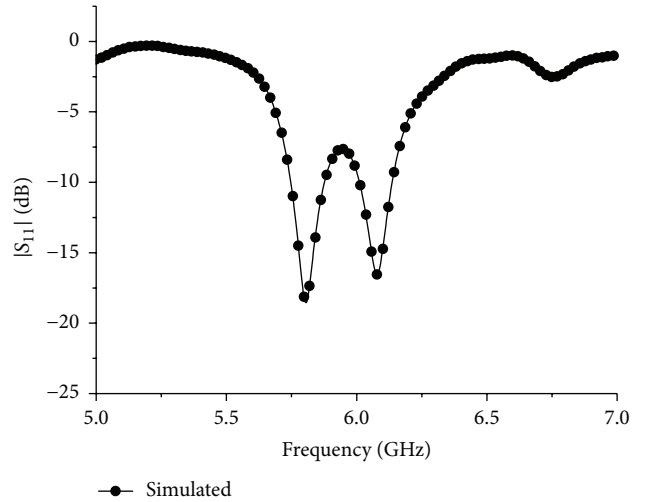


FIGURE 3: Simulated  $|S_{11}|$  for the microstrip reflectarray designed by the conventional method.

that the simulated  $|S_{11}|$  is  $-18.4 \text{ dB}$  at the working frequency of  $5.8 \text{ GHz}$  and  $|S_{11}| < -10 \text{ dB}$  impedance bandwidth is about  $2.2\%$  (from  $5.75 \text{ GHz}$  to  $5.88 \text{ GHz}$ ) and Figure 4 illustrates that the antenna has good end-fire property at  $5.8 \text{ GHz}$ , its gain is  $19.7 \text{ dBi}$ , and side-lobes are about  $12.3 \text{ dB}$  below the main lobe.

It is worth noting from the simulation results that the three metal sticks have very strong effect on the antenna's radiation properties. But the conventional design method cannot take into consideration the shielding effect of the metal sticks and just simply ignored it. According to the CST simulation, the gain of this antenna should go up to  $21.5 \text{ dBi}$ ,  $1.8 \text{ dB}$  over the gain of  $19.7 \text{ dB}$ , if the three metal sticks are taken away. This is a good example demonstrating the defect of the conventional design method.

## 4. The Proposed Design Method by Optimizing the Reflection Phase Curve

**4.1. Principle of the Proposed Design Method.** As discussed above, for the microstrip reflectarray antenna, the conventional design method may not be effective due to the approximations made in the design procedure. But the common optimization method, which employs an optimization algorithm in conjunction with the full-wave simulation to optimize antennas' structural parameters, is impractical for large-scale microstrip reflectarray antennas because of too many unknown parameters from various elements in the reflector. In this section, a new design method, which is effective and with acceptable computation burden, is proposed for the first time for the microstrip reflectarray antenna.

The reflection phase curve plays a key role in the microstrip reflectarray antenna design. Using a reflection phase curve, the structural parameters of the reflection elements can be determined according to the required phase compensation of those elements. Hence, one would expect that optimizing a reflection phase curve may result in the same effect on the antenna designed as optimizing

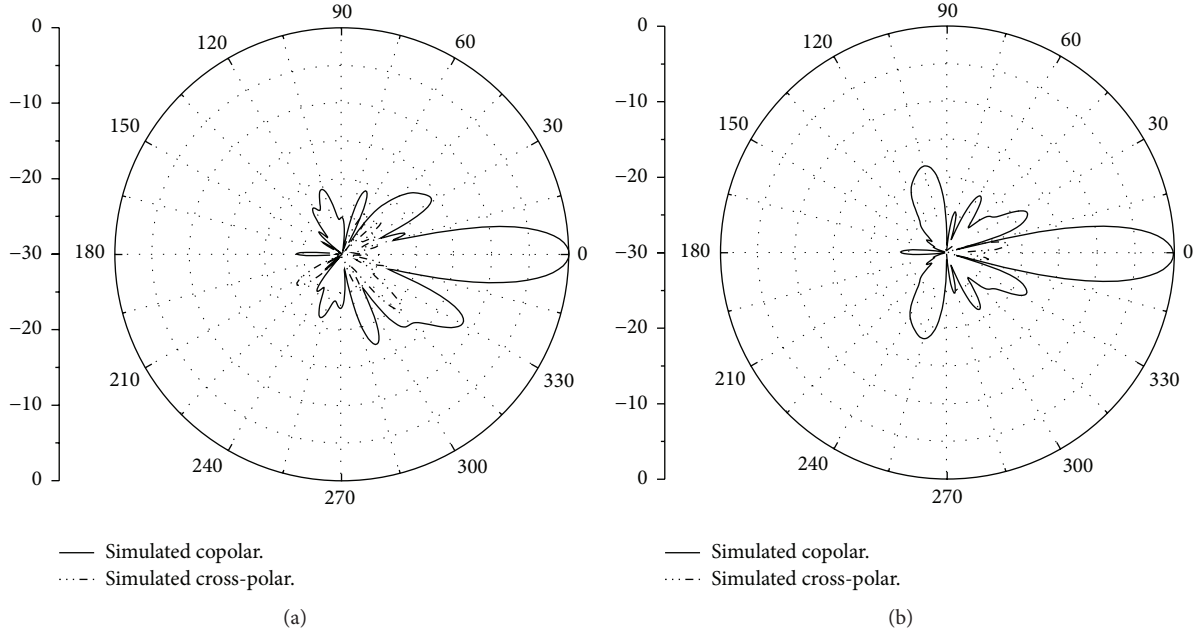


FIGURE 4: Simulated radiation patterns on the XZ plane and YZ plane: (a) XZ plane; (b) YZ plane.

the structural parameters. Moreover, the reflection phase curve is a continuous curve. Its continuity allows using only a few parameters to describe it, and thus the unknown parameters needed in the optimization can be controlled to a very low level even for a large-scale microstrip reflectarray antenna.

To validate the proposed design method, the microstrip reflectarray antenna introduced in Section II is designed as an example. In the design procedure, an optimization algorithm, that is, the genetic algorithm (GA), in conjunction with the full-wave simulation is employed for optimizing the reflection phase curve; and then the optimized curve is used to design the microstrip reflectarray antenna for high performances.

**4.2. Design Procedure.** The GA is a powerful and efficient optimization technique, which makes use of a natural evolution process: the improvement of a population of parameters along with successive generations by applying the genetic operators, for example, mutation, selection, and crossover. The GA is adopted in this paper to optimize the reflection phase curve of the microwave reflectarray antenna.

A reflection phase curve is typically “S” shaped. In this work we use the DoseResp Function defined in the following to fit the reflection phase curve:

$$f(x) = A_1 + \frac{A_2 - A_1}{1 + 10^{(\text{Mid}-x)*p}}, \quad (3)$$

where  $f$  is the phase compensation value,  $x$  represents the structural parameters that control the elements’ reflection phase, and  $A_1$ ,  $A_2$ , Mid, and  $p$  are 4 unknown parameters.

By using a curve fitting tool available in Matlab, the reflection phase curve shown in Figure 2 can be expressed

by the DoseResp Function given in (3) for  $A_1 = -536.34$ ,  $A_2 = -19.61$ , Mid = 19.63, and  $p = -0.101$ .

Besides  $A_1$ ,  $A_2$ , Mid, and  $p$ , the parameters  $L$  and  $h_1$  are also taken into the optimization for better results. Then, there are 6 unknown parameters that need to be optimized. For those unknown parameters, the determination of their possible value range is very important to the GA optimization because it has a big impact on the optimization efficiency and results. These parameters’ initial values can be obtained from the design using the conventional method; and then after giving a considerable margin for the GA-based optimization, the parameters  $L$ ,  $h_1$ ,  $A_1$ ,  $A_2$ , Mid, and  $p$  are confined to be  $0.35\lambda \sim 0.85\lambda$ , 70 mm~130 mm,  $-650 \sim -400$ ,  $-100 \sim 100$ , 0.02~30,  $-0.3 \sim -0.001$ , respectively.

The goal of the GA optimization is to achieve a high gain and good impedance match at the working frequency of 5.8 GHz. Hence, the fitness function, which represents the desired performance requirements and guides the direction of the GA optimization, is defined as

$$\text{Fitness} = C_1 \times \text{MaxGain} + C_2 \times \text{MaxS11}, \quad (4)$$

where Fitness represents the value of the fitness function; MaxGain refers to the radiation gain at the working frequency of 5.8 GHz; and MaxS11 denotes the maximum  $|S_{11}|$  over a preset frequency band ranging from 5.7 to 5.9 GHz. The values of the gain and  $|S_{11}|$  are in dB.  $C_1$  and  $C_2$  are weight coefficients, whose values should emphasize the relative importance of each term in the design requirements, but no specific rule exists for determining their values. In this work they are selected by experience and are set to be 0.03 and  $-0.02$ , respectively.

A GA-based optimization is executed. In the optimization, the GA employs tournament selection with elitism, single-point crossover with probability  $P_c = 0.5$ , and jump

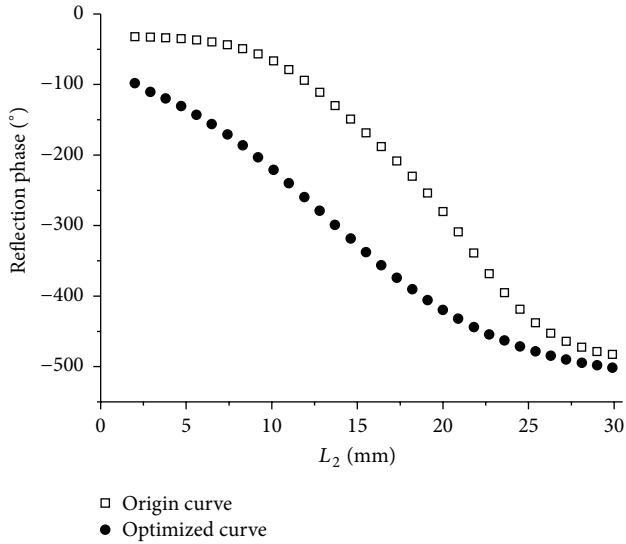


FIGURE 5: A comparison of the origin and the optimized reflection phase curve.

mutation with probability  $P_m = 0.2$ , and it uses 50 generations and 100 individuals in a population.

In the design procedure, the performance of the antenna is simulated by full-wave simulations employing CST MWS. To reduce the heavy computational burden, the design procedure is parallelized in a master-slave model and implemented on a Beowulf cluster system [13]. The Beowulf cluster system consists of 32 processors interconnected by a fast 1000 Mb/s Ethernet. One processor, named the master processor, carries out the GA optimization while all the others, called slave processors, execute the full-wave simulations.

**4.3. Results and Analysis.** The parameters determined by the GA-based optimization are as follows:  $L = 0.409\lambda$ ,  $h_1 = 95.75$  mm,  $A_1 = -521.34$ ,  $A_2 = -48$ ,  $\text{Mid} = 13.05$ , and  $p = -0.08$ .

Because the optimized element spacing  $L$  is  $0.409\lambda$ , which is less than that in the conventional design described above, the reflector with fixed size of  $300 \times 300$  mm<sup>2</sup> is able to contain  $11 \times 11$  reflection elements. It can be seen that there are 20 reflection elements with different dimensions in the reflector of this antenna. Noticing that each different element has one unknown parameter, and adding the parameters  $c_0$  and  $h_1$ , there would be 22 unknown parameters in need for optimization if we utilize the common optimization method. Obviously, it is very difficult for an optimization algorithm, even for a powerful algorithm such as the GA, to achieve good results with so many parameters that need to be optimized.

In Figure 5, the optimized reflection phase curve is compared with the origin one. Based on the optimized reflection phase curve, the structural parameters of the reflection elements are determined; and then a prototype antenna is fabricated and depicted in Figure 6. To illustrate the dimension of the antenna, a ruler is placed in front of it in the figure.

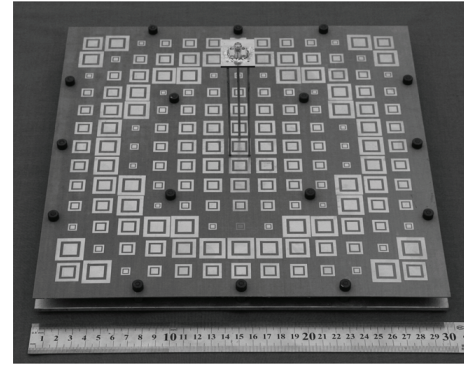


FIGURE 6: Prototype of the antenna.

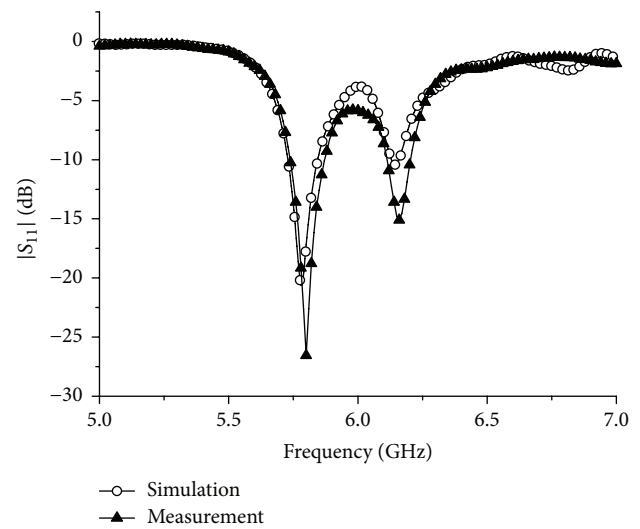


FIGURE 7: Measured and simulated  $|S_{11}|$ .

The reflection coefficient of the prototype antenna is measured with an Agilent E8362B vector network analyzer. In Figure 7, the measured and simulated  $|S_{11}|$  curves are compared with each other and a good agreement is observed. Also, the figure illustrates that  $|S_{11}| < -10$  dB impedance bandwidth is about 2% (from 5.77 GHz to 5.88 GHz), which is very close to that achieved by the conventional design method.

The radiation patterns of the proposed antenna are measured in an anechoic chamber, and the measurement results are compared with the simulated radiation patterns in the XZ plane and YZ plane at 5.8 GHz. The comparison is shown in Figure 8, where one observes that they also agree very well and this antenna possesses good end-fire property. The measured side-lobes are about 18 dB below the main lobe, and the measured cross-polarization levels are less than 20 dB in both XZ and YZ planes.

Figure 9 compares measured gains against frequencies of two antennas; one of them is designed by the conventional method and the other is designed by the proposed optimization method. The comparison shows that, in comparison with the conventional method, the proposed optimization

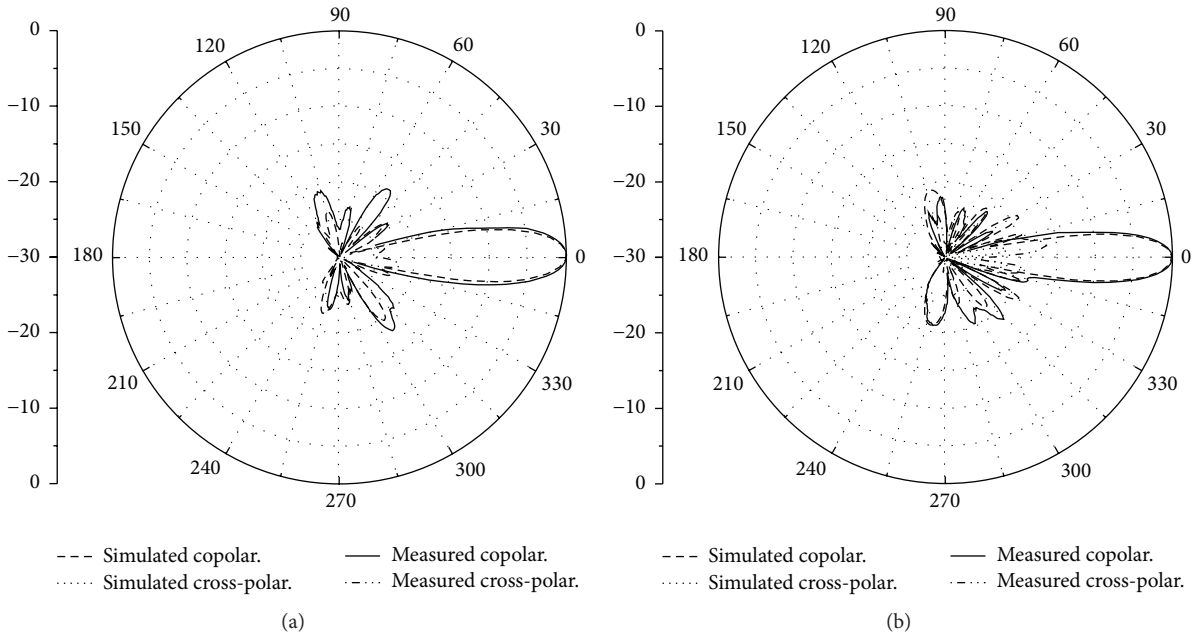


FIGURE 8: Measured and simulated radiation patterns on the XZ plane and YZ plane: (a) XZ plane; (b) YZ plane.

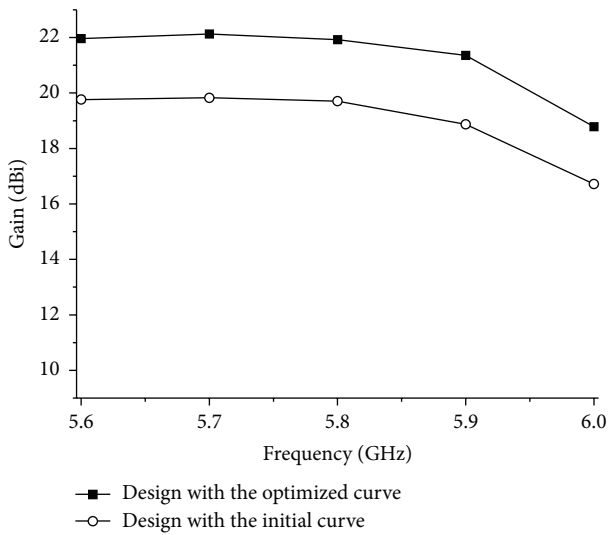


FIGURE 9: Gain comparison with frequency varying from 5.6 to 6.0 GHz.

method has considerably improved the gain of the microstrip reflectarray antenna over the frequency band from 5.6 GHz to 6.0 GHz; at the working frequency of 5.8 GHz, it achieves a gain of 21.9 dB, which is 2.2 dB over that of the conventional design (19.7 dBi) and even more than that of the conventional design without three metal sticks (21.5 dBi). This demonstrates that the proposed optimization method is able to remedy or offset the adverse effects caused by some factors such as the support frame’s shield.

### 5. Conclusions

Currently, the design of the microstrip reflectarray is under an embarrassing condition. The conventional design, which is adopted for most microstrip reflectarray antennas, may not be effective due to many approximations made in its design procedure, while the common optimization method that optimizes antennas’ structural parameters is impractical for large-scale antenna because of too many parameters in need for optimization. A novel design method is proposed in this paper. It employs an optimization algorithm such as the GA in conjunction with the full-wave simulation to optimize the reflection phase curve and utilizes the optimized curve to design a microstrip reflectarray antenna.

As an example, the design of a microstrip reflectarray antenna with fixed size of  $300 \times 300 \text{ mm}^2$  for high gain is presented. The results demonstrate that the proposed method is feasible and effective. Being able to avoid the approximations made in the conventional design, it can greatly improve the antenna’s gain over 2.2 dB (from 19.7 dBi to 21.9 dBi). By controlling the number of the unknown parameters in need for optimization to a low level, the proposed method only need to optimize 6 parameters, but the common optimization method has to optimize 22 parameters. Hence, the proposed method has the ability of designing large-scale antennas. These merits will make the proposed method to be a powerful tool for the design of microstrip reflectarray antennas.

### Competing Interests

There is no conflict of interests related to this paper.

## Acknowledgments

This work was supported by the China NSAF Fund under Grant U1230112.

## References

- [1] C. S. Malagisi, "Microstrip disc element reflectarray," in *Proceedings of the Electronics and Aerospace Systems Convention*, vol. 1, pp. 186–192, Arlington, Va, USA, September 1978.
- [2] J. Huang and J. A. Encinar, *Reflectarray Antennas*, Wiley Interscience, 2007.
- [3] J. A. Encinar, M. Arrebola, M. Dejus, and C. Jouve, "Design of a 1-metre reflectarray for DBS application with 15% bandwidth," in *Proceedings of the 1st European Conference on Antennas and Propagation (EuCAP '06)*, pp. 1–5, Nice, France, November 2006.
- [4] C. Cheymol, T. Dousset, P. Dumon, M. Labeyrie, and C. Renard, "A X-band electronically scanned reflectarray antenna for space telemetry," in *Proceedings of the European Conference on Antennas and Propagation (EuCAP '03)*, pp. 2766–2668, Berlin, Germany, November 2009.
- [5] J. Huang, "Microstrip reflectarray antenna for the SCANSCAT radar application," JPL Publication 90-45, 1990.
- [6] H. Li, B.-Z. Wang, G. Zheng, W. Shao, and L. Guo, "A reflectarray antenna backed on FSS for low RCS and high radiation performances," *Progress In Electromagnetics Research C*, vol. 15, pp. 145–155, 2010.
- [7] J. Ethier, M. R. Chaharmir, and J. Shaker, "Reflectarray design comprised of sub-wavelength coupled-resonant square loop elements," *Electronics Letters*, vol. 47, no. 22, pp. 1215–1217, 2011.
- [8] S. Costanzo, "Reflectarray antennas: analysis and synthesis techniques," *International Journal of Antennas and Propagation*, vol. 2012, Article ID 945682, 3 pages, 2012.
- [9] F.-C. E. Tsai and M. E. Bialkowski, "An equivalent waveguide approach to designing of reflect arrays with the use of variable-size microstrip patches," *Microwave and Optical Technology Letters*, vol. 34, no. 3, pp. 172–175, 2002.
- [10] S. D. Targonski and D. M. Pozar, "Analysis and design of a microstrip reflectarray using patches of variable size," in *Proceedings of the IEEE Antennas and Propagation International Symposium*, pp. 1820–1823, IEEE, June 1994.
- [11] R. D. Javor, X.-D. Wu, and K. Chang, "Design and performance of a microstrip reflectarray antenna," *IEEE Transactions on Antennas and Propagation*, vol. 43, no. 9, pp. 932–939, 1995.
- [12] R. E. Zich, M. Mussetta, M. Tovaglieri, P. Pirinoli, and M. Orefice, "Genetic optimization of microstrip reflectarrays," in *Proceedings of the Antennas and Propagation Society International Symposium*, pp. 128–131, San Antonio, Tex, USA, June 2002.
- [13] X. Chen, K. Huang, and X.-B. Xu, "Automated design of a three-dimensional fishbone antenna using parallel genetic algorithm and NEC," *IEEE Antennas and Wireless Propagation Letters*, vol. 4, no. 1, pp. 425–428, 2005.
- [14] J. M. Jayasinghe, J. Anguera, D. N. Uduwawala, and A. Andújar, "Nonuniform overlapping method in designing microstrip patch antennas using genetic algorithm optimization," *International Journal of Antennas and Propagation*, vol. 2015, Article ID 805820, 8 pages, 2015.
- [15] K. Michael and A. Kucharski, "Genetic algorithm optimization for multiband patch antenna design," in *Proceedings of the 1st European Conference on Antennas and Propagation (EuCAP '06)*, pp. 1–4, Nice, France, November 2006.
- [16] M. Rattan, M. S. Patterh, and B. S. Sohi, "Optimization of gain, impedance, and bandwidth of Yagi-Uda array using particle swarm optimization," *International Journal of Antennas and Propagation*, vol. 2008, Article ID 193242, 4 pages, 2008.
- [17] Y. Chen, X. Chen, and K. Huang, "Design of microstrip reflectarray antenna using a genetic algorithm based optimization method," *Electromagnetics*, vol. 32, no. 2, pp. 77–85, 2012.
- [18] D. M. Pozar and T. A. Metzler, "Analysis of a reflectarray antenna using microstrip patches of variable size," *Electronics Letters*, vol. 29, no. 8, pp. 657–658, 1993.